

https://dspace.org/

Full Run-2 boosted right-handed heavy neutrino and single leptoquark searchin ATLAS

Davou, Christopher Lawrence

2021
https://hdl.handle.net/10539/33087

Downloaded from a DSpace repository. https://dspace.org/

Full Run-2 boosted right-handed heavy neutrino and single leptoquark search in ATLAS



Christopher Lawrence Davou
lawrence.davou.christopher@cern.ch
School of Physics
University of the Witwatersrand

Supervisor: Prof Deepak Kar
deepak.kar@cern.ch

A Thesis Submitted in conformity with the requirements for the degree of Doctor of Philosophy, School of Physics, Institute for Collider Particle Physics, University of the Witwatersrand

Johannesburg, 2021

Declaration

This thesis represents my original research work. Every effort has been made to indicate the contributions of others by duly referencing in the literature and acknowledging collaborative research and discussion. The study was done under the supervision of Prof Deepak Kar, at the school of Physics, Institute for collider particle physics, University of the Witwatersrand, Johannesburg South Africa.



Name of Candidate: **Christopher Lawrence Davou**
Date: 11/11/2021

Dedication

This work is dedicated to my mother late Ngo Christiana Christopher Davou who died on the 14/06/2021 and my late father Da Christopher Davou Gatong who died on the 21/10/2021. It was like my whole world came crumbling down, I have always wished I will return and see you both again but all I have now is just memories. It is very devastating to know that I will not be able to see you two again. Up till this very moment I have not been able to process that, I sincerely pray that God will grant you eternal rest and I will always miss you dear mum and dad.

Acknowledgement

The decision to enroll for a PhD in high energy physics is out of my fantasy and curiosity for particles of nature and radiation. I had to wait for a long time before this dream came to reality even though it came at a personal cost, but I am happy I was able to fulfill this dream. My Special thanks to God Almighty for making this possible and seeing me through this study even when I contracted Covid-19 in the course of my PhD. My sincere gratitude goes to my amazing supervisor Prof. Deepak Kar, thank you for believing in me by accepting to be my mentor, I really enjoyed working under your guidance and learning from you. Your dedication to my success will never go unnoticed, not every student is lucky to have a dynamic supervisor like you and if I am asked to choose again, I will still prefer to work under you again and again. Your book Experimental Particle Physics: Understanding the measurements and searches at the Large Hadron Collider published by IOP was very insightful for me in the course of my PhD. I will also like to thank the leader of our group Prof. Bruce Mellado and the entire SA-CERN group and the staff of the school of Physics, you made my time a memorable one at Wits. My appreciation goes to other colleagues that I met in the school of Physics, Wits university that assisted me in one way or the other while doing my research, they include: Dr. Stefan von Buddenbrock, Dr. Shell-May Liao, Dr. Kahinde Tomiwa, Abdualzeem Fadol, Dimbiniaina Rafanoharana, Sukanya Sinha, Esra Shrif, Dr. Sunday Olorunfemi, Harshna Jivan and I will not forget Thokozile Manaka who helped me settle down when I first arrived South Africa. I will also like to appreciate the assistance I received from Dr. Debarati Roy, Dr. Salah-Eddine Dahbi and Dr. Marvin Flores in the course of my PhD.

I will not forget the invaluable contributions of Dr. Philip Sommer, Kamal Saoucha, my Egamma technical supervisors and all the members of the Egamma team for their inputs during my qualification task in ATLAS. Special appreciation goes to the single leptoquark analysis team especially Yoav and Marcus and the Heavy neutrino analysis team. I cannot forget to express my sincere appreciation to Prof. Jon Butterworth of UCL for the wonderful gift of the book "Most Wanted Particle", anytime I travel, it is always my travel companion because it always gives me fresh ideas in particle physics.

To my dad Da Christopher Davou and mum Ngo Christiana Christopher Davou, I want to say thank you for believing in me, To my wife Nasiba Lawrence and all my sisters and my friend Zumnan Daze, I want to thank you all for the moral support and encouragement. I will not forget the invaluable support of Prof Y.Y. Jabil, the current Head, department of Physics, Unijos, Dr. Emmanuel Taddy and Dr. Robert Dawam. I will always be indebted to you and I will ever remain grateful for the assistance, prayers and encouragement. Thank you to Fr. Otu Elijah for making me feel at home far away from home and to my wonderful colleague Fr. Ekefre Edidiong, thank you for the friendship.

This work is based on the research supported by the National Research Foundation of South Africa (NRF) in conjunction with The World Academy of Science (TWAS) Grant number 1106886 and Ref No: SFH170530235137, without which this study will not

have been possible. Thank you for making my dream come true.

I got to this stage not because of anything but grace and because I stood on the shoulders of giants. A lot of people have played various roles in my life and the list is endless, all I can say is thank you.

Abstract

Two searches for physics beyond the Standard Model scenario are presented in this thesis, the first is a search for right-handed gauge boson W_R, decaying into a boosted right-handed heavy neutrino N_R, and a lepton while the second search is the single leptoquark search decaying to a lepton and a quark using 139 fb^{-1} of proton- proton data from the ATLAS detector at $\sqrt{s}$ =13 TeV. Only the electron final state is considered in this thesis for the right-handed gauge boson search which uses a large-radius jet containing an electron as a proxy for the N_R. A detailed study to improve the identification of electrons close to jets in the context of this search is also presented. The result for the search shows no significant deviation from the Standard Model implying no new physics was observed.

The single leptoquark search presented in this thesis considers leptoquarks decaying into an electron or muon in association with a strange or bottom quark in the final state. The leptoquark mass range is between 500 GeV - 2500 GeV. For each of the signal regions, the expected upper limits at 95% CL on the single leptoquark production cross section as a function of the leptoquark mass were set for leptoquarks coupling to electron, muon, strange and bottom quarks. In the electron b-veto channel, the model exclude leptoquarks coupling to strange quarks at masses below 1.1 TeV while for leptoquarks coupling to b-quarks and electrons, the model excludes the masses below 1.0 TeV. Similarly, for the muon channel, the exclusion is at masses below 1.1 TeV for the leptoquarks coupling to strange quark and 1.0 TeV for the leptoquarks coupling to the bottom quark. No new physics has been observed in this analysis.

Contents

Declaration i

Dedication ii

Acknowledgement iii

Abstract v

1 The Standard Model of Particle Physics 1
- 1.1 The Symmetries and Lagrangian of the Standard Model . . . 2
- 1.2 Global symmetry breaking and the goldstone bosons . . . 3
- 1.3 Local symmetry breaking and the Higgs boson . . . 4
- 1.4 SU(2) symmetry and symmetry breaking . . . 5
- 1.5 New physics scenarios probed in this thesis . . . 8

2 The Large Hadron Collider and the ATLAS experiment 10
- 2.1 Physics at the LHC . . . 10
- 2.2 The Large Hadron Collider . . . 10
- 2.3 Overview of the ATLAS Detector . . . 13
- 2.4 Coordinate system in ATLAS . . . 14
- 2.5 The ATLAS Inner Detector (ID) . . . 15
- 2.6 The Calorimeter System . . . 15
- 2.7 The Muon Spectrometer System . . . 17
- 2.8 Event simulation in hadron collisions . . . 17

3 Event Reconstruction in ATLAS 21
- 3.1 ATLAS trigger system . . . 21
- 3.2 Electron reconstruction . . . 22
- 3.3 Jet reconstruction . . . 25

4 Boosted right-handed heavy neutrino search 28
- 4.1 Introduction . . . 28
- 4.2 Analysis strategy . . . 29
- 4.3 Overview of the analysis . . . 30
- 4.4 Signal and background MC samples . . . 30
- 4.5 Object and event selection . . . 31
- 4.6 Event selection . . . 33
- 4.7 The electron-in-jet identification study . . . 34
- 4.8 Variables used in electron identification . . . 37
- 4.9 Isolated electron and electron-in-jet comparison . . . 39
- 4.10 Profile plots of electron in jet ID as a function of angular distance . . . 42
- 4.11 Electron in jet identification variables inside a jet . . . 44
- 4.12 Control region . . . 48

4.13 Control region summary . . . 52
4.14 Systematic uncertainty . . . 53
4.15 Background estimation in the SR . . . 57
4.16 Conclusion . . . 61

5 Search for single leptoquarks in final states with electrons and muons 62
5.1 Introduction . . . 62
5.2 Data . . . 63
5.3 Signal and background samples . . . 63
5.4 Object reconstruction and selection . . . 65
5.5 Event selection . . . 66
5.6 Background estimation . . . 67
5.7 Systematic uncertainty . . . 80
5.8 Statistical analysis and results . . . 81
5.9 Conclusion . . . 99

6 Summary 100

Bibliography 101

List of Figures

1.1 The Standard Model of particles . . . 2
1.2 Plot of potential as a function of the classical field . . . 4

2.1 The CERN accelerator complex . . . 11
2.2 Cumulative luminosity delivered by LHC . . . 12
2.3 ATLAS integrated luminosity for Run 1, and Run 2 . . . 12
2.4 A cut-away section through the ATLAS detector . . . 13
2.5 Illustration of the ATLAS coordinate system . . . 14
2.6 A barrel view of the ATLAS inner detector . . . 15
2.7 A cut-away view of the ATLAS calorimeter system . . . 16
2.8 Sketch of the section through the LAr EM barrel . . . 16
2.9 A cut-away view of the ATLAS muon system . . . 17
2.10 A schematic diagram of a complete event generation by a Z + jets process 20

3.1 The ATLAS trigger system . . . 22
3.2 An electron moving through the ATLAS detector . . . 23
3.3 A flow chart of the particle flow algorithm . . . 26
3.4 Jet clustering algorithms . . . 27

4.1 Feynman diagram of the production of W_R in a proton-proton collision and decay . . . 29
4.2 Signal selection efficiency for a number of mass points . . . 35
4.3 Feynman diagram for the production and decay of W_R . . . 35
4.4 Overlap of boosted decay products of the heavy neutrino system . . . 36
4.5 Efficiency vs E_T and η . . . 36
4.6 Efficiency vs ΔR . . . 37
4.7 Plot of energy width variables . . . 39
4.8 Plot of energy ratio variables . . . 40
4.9 Track-cluster match variables . . . 41
4.10 Profile of energy ratio and some track variables . . . 42
4.11 Profile of cluster match variables . . . 43
4.12 Plot of f_1, and f_3 vs angular distance . . . 44
4.13 Distribution of track and the track-cluster match variables vs angular distance . . . 45
4.14 Distribution of energy ratio and width variables vs angular distance . . . 46
4.15 Electron efficiency as a function of E_T and η from electron in jet ID . . . 47
4.16 Leading electron kinematics in the CR from data and MC . . . 48
4.17 Kinematics of sub-leading electron, large-radius jet and di-electron in the CR . . . 49
4.18 W_R kinematics and angular distributions in the CR . . . 50
4.19 W_R, N_R and electron kinematic distributions in the CR . . . 51
4.20 Di-electron invariant mass distribution in the CR . . . 52
4.21 Uncertainties due to large-radius-jet JES and JER . . . 54

4.22 Electron uncertainties due to energy resolution, energy scale, Identification, and pileup . . . 55
4.23 Uncertainties due to electron reconstruction, trigger, and isolation . . . 56
4.24 Background and nominal fit functions . . . 58
4.25 Toys and background fit functions . . . 59
4.26 Toys and background fit functions . . . 60

5.1 Feynman diagrams for single LQ production . . . 63
5.2 A schematic representation of the event selection of the analysis. . . . 67
5.3 Pre-fit and post-fit plots for the electron channel . . . 69
5.4 Pre-fit and post-fit plots for the muon channel . . . 70
5.5 Extrapolation of the high mass LQ top background for the electron b-veto channel . . . 71
5.6 Extrapolation of the high mass LQ top background for the electron b-tag channel . . . 72
5.7 Plots for the electron channel showing the pre-fit and post-fit in TCR . . 74
5.8 Plots for the muon channel showing the pre-fit and post-fit in the TCR . 75
5.9 Extrapolation of the high mass LQ top background for the electron channel in the top-Control region . . . 76
5.10 Extrapolation of the high mass LQ top background for the electron channel in the VR region . . . 77
5.11 Plots for the electron channel showing the pre-fit and post-fit in the VR . 78
5.12 Plots for the muon channel showing the pre-fit and post-fit in the VR . . 79
5.13 Pre-fit and post-fit event yields in the signal, control and validation regions 83
5.14 The reduced correlation matrix for electron channel, b-veto . . . 85
5.15 Ranking plot of the nuisance parameters electron channel b-veto . . . 86
5.16 Expected upper limit at 95 % confidence level (CL) electron channel b-veto 87
5.17 Pre-fit and post-fit event yields in the signal, control and validation regions 88
5.18 The reduced correlation matrix for electron channel, b-tag . . . 89
5.19 Ranking plot of the nuisance parameters electron channel, b-tag . . . 90
5.20 Expected upper limit at 95 % confidence level (CL) electron channel, b-tag 91
5.21 Pre-fit and post-fit event yields in the signal, control and validation regions 92
5.22 The reduced correlation matrix for muon channel, b-veto . . . 93
5.23 Ranking plot of the nuisance parameters for muon channel, b-veto . . . 94
5.24 Expected upper limit at 95 % confidence level (CL) for muon channel, b-veto . . . 95
5.25 Pre-fit and post-fit event yields in muon channel b-veto . . . 96
5.26 The reduced correlation matrix of the nuisance parameters for muon channel b-tag . . . 97
5.27 Ranking plot of the nuisance parameters for muon channel b-tag . . . 98
5.28 Expected upper limit at 95 % confidence level (CL) for muon channel b-tag 99

List of Tables

4.1 Overview of the simulated background samples. 31
4.2 Criteria for selection of object for the analysis. 33
4.3 SR and CR region definition. 34
4.4 Variables used in electron identification 38
4.5 Table showing variables chosen for our electron in jet ID 47
4.6 Yields in CR from background and data with statistical uncertainties. . 52
4.7 Summary of systematic uncertainties for the background estimate and signal. 54
4.8 Event yield in the signal region. 61

5.1 Event generators and other software packages 65
5.2 A summary of event selection for the four signal regions. 66
5.3 Post-fit event yield in all channels in the ZCR 68
5.4 Post-fit event yield in all channels in the TCR 73
5.5 A summary of the fit ranges and the Q-cut values 73
5.6 Post-fit event yield for all channels in the validation region 77
5.7 A summary of the theory uncertainty nuisance parameters for single top and $t\bar{t}$ MC samples. 81
5.8 A summary of the theory uncertainty nuisance parameters for $t\bar{t}V$ MC samples. 81
5.9 A summary of the cut value of the LQ mass with the best upper limit on the signal strength 84
5.10 A summary of the cut value of the LQ mass for electron channel b-tag . 88
5.11 A summary of the cut value of the LQ mass for muon channel b-veto . . 92
5.12 A summary of the cut value of the LQ mass for muon channel b-tag . . . 96

1. The Standard Model of Particle Physics

All matter in the universe is composed of a few primary building blocks termed fundamental particles governed by four fundamental forces. Our best understanding of the relationship between these particles and three of the forces is formulated in the standard model (SM). The SM is composed of elementary particles: twelve fermions with spin-$\frac{1}{2}$, one spin-0 boson, and four spin-1 bosons as seen in Figure 1.1, and it explains the interactions among these particles. The spin-0 boson is the Higgs boson, which comes from the excitation of the Higgs field that is found everywhere. The Higgs field is responsible for the masses of quarks and charged leptons through Yukawa coupling and the masses of the W and Z gauge bosons through the Higgs mechanism [1].

The four spin-1 bosons are the gluon, photon, W and Z bosons. The twelve fermions are made up of six quarks flavours and six leptons. Leptons maybe charged or uncharged while all quarks carry the electric charge of either $\frac{2}{3}$ or -$\frac{1}{3}$ in units of electron charge. Charged leptons interact through the electromagnetic interaction, and together with uncharged leptons also undergo weak interactions. Quarks interact through the electromagnetic, weak and strong interactions. Quarks and leptons are grouped into three generations with the first generation, the lightest fermion family made up of up quark, down quark, electron, and electron neutrino. The second generation which is heavier than the first generation is made up of charm quark, strange quark, muon, and the muon neutrino while the third generation, the heaviest of all the three generations is composed of the top quark, bottom quark, τ and the τ neutrino. Each of the fermions has a corresponding anti-fermion having the same mass and spin but opposite charge and opposite magnetic moment relative to the spin direction correctly predicted by Dirac's equation for a massive charged fermion. The gluon and the photon are massless, the gluon is the mediator (quanta) of the strong force felt by quarks. Unlike the electromagnetic field, the gluon fields are confining because gluons carry colour charge likewise quarks and as a result can not be isolated. This is why quarks and gluons must bound together to form hadrons. Two major types of hadrons exist i.e the meson which is a bound state of a quark and an antiquark, and baryon which is a bound state of three quarks.

Quantum chromodynamics (QCD) [2] explains this interaction between coloured particles through the exchange of gluons. The photon is the mediator of the electromagnetic force between charged particles described by quantum electrodynamics (QED) [3]. The W and Z bosons are massive and are the carriers of the weak force, however, at high energies, electromagnetic and the weak forces become indistinguishable. This is explained by QED. The weak interaction makes it possible for quarks and leptons to switch flavor. Quark flavor changing is made possible by the Cabibbo−Kobayashi−Maskawa (CKM) mixing matrix which enable CP violation and rare decays [4]. The Standard Model has been successful in explaining almost all experimental result and also predicting various phenomena precisely making it a well tested and established physics theory. This model consists of the strong, electromagnetic and weak forces as well as their carrier particles, explaining the nature of these forces interacting with all building blocks of matter. Even with the successes of the Standard Model, it is unable

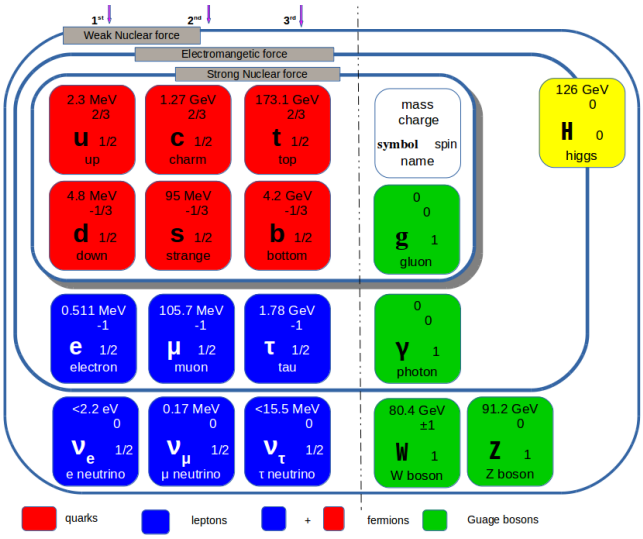


Figure 1.1: *The Standard Model of particles*

to explain why gravity is so much weaker than the electromagnetic and the nuclear forces, the hierarchy problem relating to the strength of the fundamental forces and also the Higgs boson mass and also dark matter necessitating the studies at the LHC. The SM theory is summarized by a *lagrangian* that describes all the interactions between the particles (fields).

1.1 The Symmetries and Lagrangian of the Standard Model

The SM, a theory of interacting fields guided by the principles of symmetry is an $SU(3)_C \otimes SU(2)_L \otimes U(1)_Y$ locally gauge invariant theory that is imposed on the quark and lepton field operators. Each group's generators are the corresponding spin-1 particles that mediate the force associated with the group. QCD which describes strong interactions is invariant under the local $SU(3)_C$ colour symmetry group with the colour being the charge of the strong force. $SU(3)_C$ is made up of eight (N^2 - 1) generators that correspond to eight colour-charge gluons. Weak and EM interactions combined together to have local invariance under the $SU(2)_L \otimes U(1)_Y$ transformation with "L" indicating that only left-handed fermion interactions are allowed and "Y" is the weak hypercharge. The electroweak group has four generators which are related to the four electroweak theory gauge bosons, γ, $W^{\pm}$ and Z from the linear combination of the fields which transform under this group. The combination of the U(1) weak hypercharge and the third component of the weak isospin can be used to determining the charge: $Q = T_3 + Y/2$. The photon remains massless while the weak bosons acquire mass from spontaneous symmetry breaking through the Higgs mechanism [1]. This is because Brout, Englert, Higgs [5, 6] and others pointed out that when you have a gauge symmetry and also a spontaneously broken symmetry, the masseless scalar particle from the broken symmetry will get incorporated into the gauge bosons from the local symmetry. This will allow the gauge bosons to have mass and eliminate the massless scalar particle

detailed further in section 1.4. The SM Lagrangian can be written compactly fully as:

$$\begin{aligned}\mathscr{L} = -\frac{1}{4}F_{\mu\nu}\,F^{\mu\nu} + i\bar{\psi}D\psi + h.c.\,(Interactions)\\ +|D_\mu\phi|^2 + V(\phi)\,(Higgs)\\ +\psi_i y_{ij}\psi_j\phi + h.c.\,(Yukawa)\end{aligned} \tag{1.1.1}$$

The first line represents the massless vector-gauge fields and their interactions with the matter spinor-fields (ψ) through the covariant derivative, h.c means hermitian conjugate.The second line is the Higgs potential while the last line is the Yukawa couplings of the Higgs which can generate mass terms that are forbidden by gauge invariance. Section 1.2, 1.3, and 1.4 will discuss symmetry breaking in models and theories and their implications. A brief introduction of physics beyond the Standard Model will be given in section 1.5. Since we are dealing with hadron collision which is a complex process, section 2.8 will discuss how events are simulated in hadron collision

1.2 Global symmetry breaking and the goldstone bosons

For a complex scalar field $\Phi = (\phi_1 + i\phi_2)/\sqrt{2}$ a possible lagrangian density is

$$\mathscr{L} = \partial_\mu\,\Phi^\dagger\,\partial^\mu\,\Phi\, - m^2\,\Phi^\dagger\,\Phi\,. \tag{1.2.1}$$

From the above lagrangian, we can regard the kinetic energy density as $(\partial\Phi^\dagger/\partial t)(\partial\Phi/\partial t)$ with $\nabla\Phi^\dagger\,\nabla\Phi + m^2\Phi^\dagger\Phi$ as the potential energy density. If Φ is independent of space and time, the only contribution to the energy will be $m^2\Phi^\dagger\Phi$. This will be a minimum when $\phi_1 = \phi_2 = 0$ since m^2 is positive, $\Phi = 0$ corresponds to the vacuum state. If we now change the sign in front of m^2 and look at the lagrangian density, it becomes unstable: the potential energy density is then unbounded with the term $(m^2/2\phi_0^2)(\Phi^\dagger\Phi)^2$ where ϕ_0^2 is another real parameter where for convenience, a constant term $m^2\phi_0^2/2$ is added such that

$$\mathscr{L} = \partial_\mu\,\Phi^\dagger\,\partial^\mu\,\Phi\, - V(\Phi^\dagger\,\Phi). \tag{1.2.2}$$

Where

$$V = \frac{m^2}{2\phi_0^2}[\Phi^\dagger\Phi - \phi_0^2]^2\,. \tag{1.2.3}$$

The form of V is shown in Figure 1.2. The minimum energy of the field is then obtained with the field independent of space and time (constant) but such that $\Phi^\dagger\Phi = |\Phi|^2 = \phi_0^2$. This field is non-unique is defined by a circle $|\Phi| = \phi_0$ in the state space (ϕ_1, ϕ_2) which makes the number of vacuum states possible to be infinite. The lagrangian density Eq. 1.2.2 has a global U(1) symmetry: $\Phi \rightarrow \acute{\Phi} = e^{-i\beta}\Phi$, $\mathscr{L} \rightarrow \acute{\mathscr{L}} = \mathscr{L}$ for any real β. Also,

$$\begin{aligned}\acute{\phi_1} &= \phi_1\cos\beta + \phi_2\sin\beta,\\ \acute{\phi_2} &= -\phi_1\sin\beta + \phi_2\cos\beta.\end{aligned}$$

If we select a direction in the state space for which Φ is real, and we take $(\phi_0, 0)$ to be our vacuum, we break the U(1) symmetry. Expanding about this vacuum state, if Φ =

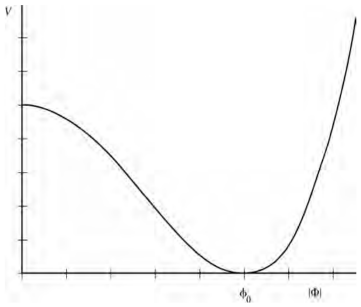


Figure 1.2: *Plot of* $V = \frac{m^2}{2\phi_0^2}[\Phi^*\Phi\text{-}\phi_0^2]^2$ *as a function of* $|\Phi|$ *where the* Φ *is a classical field [7]*

$\phi_0 + (1/\sqrt{2})(\chi + i\psi)$. We have a lagrangian density of the form,

$$\mathscr{L} = \frac{1}{2}\,\partial_\mu \chi\,\partial^\mu \chi + \frac{1}{2}\,\partial_\mu \psi\,\partial^\mu \psi - \frac{m^2}{2\phi_0^2}\,[\sqrt{2}\,\phi_0\,\chi + \frac{\chi^2}{2} + \frac{\psi^2}{2}]^2\,. \tag{1.2.4}$$

We can see that in place of the complex field Φ, we end up with two coupled scalar fields ψ and χ that are real. We decompose the lagrangian density into $\mathscr{L} = \mathscr{L}_{\text{free}} + \mathscr{L}_{\text{int}}$, where

$$\mathscr{L}_{\text{free}} = \frac{1}{2}\,\partial_\mu \chi\,\partial^\mu \chi - m^2\,\chi^2 + \frac{1}{2}\,\partial_\mu \psi\,\partial^\mu \psi\,. \tag{1.2.5}$$

The free component of the lagrangian density contains all the quadratic field terms in $\mathscr{L}$ and represents free fields while the $\mathscr{L}_{\text{int}}$ are interactions between the free particles and higher order corrections in their motion. The χ fields are scalar spin-zero particles of mass $\sqrt{2}$m due to the quadratic term while for the ψ field the corresponding scalar spin-zero particle is massless due to the absence of the quadratic term. Such massless particles that always result from the breaking of global symmetry are known as Goldstone bosons.

1.3 Local symmetry breaking and the Higgs boson

Constructing a Lorentz invariant lagrangian density invariant under local U(1) gauge transformation $\Phi \rightarrow \acute{\Phi} = e^{-iq\beta}\Phi$, where $\beta = \beta(x)$ might be space and time dependent, requires the introduction of a massless gauge field B_μ giving us:

$$\mathscr{L} = [(\partial_\mu - i\,q\,B_\mu)\Phi^\dagger\,][(\partial^\mu + i\,q\,B^\mu)\Phi\,] - \frac{1}{4}\,F_{\mu\nu}\,F^{\mu\nu} - V(\Phi^\dagger\,\Phi). \tag{1.3.1}$$

where $F_{\mu\nu} = \partial_\mu B_\nu - \partial_\nu B_\mu$ and $V(\Phi^\dagger\Phi)$ is of the form in Eq. 1.2.3. The above lagrangian is invariant under local gauge transformation. The symmetry can be broken if for a given $\Phi(x)$ $\beta(x)$ can always be chosen such that the field $\acute{\Phi}(x) = e^{iq\beta}\Phi(x)$ is real. This is because we have lost the freedom of making further gauge transformations. To show

this, let us take $\acute{\Phi}(x) = \phi_0 + b(x)/\sqrt{2}$, with b(x) real, we will have

$$\mathscr{L} = [(\partial_\mu - i\,q\,\acute{B}_\mu)(\phi_0 + b/\sqrt{2})][(\partial^\mu + i\,q\,B^\mu)(\phi_0 + b/\sqrt{2})] - \frac{1}{4}F_{\mu\nu}F^{\mu\nu} - \frac{m^2}{2\phi_0^2}[\sqrt{2}\,\phi_0\,b + \frac{1}{2}b^2]^2\,. \tag{1.3.2}$$

Before the breaking of symmetry, we had a masseless vector field with 2 polarization states and a complex scalar field $\Phi = (\phi_1 + i\phi_2)/\sqrt{2}$, after symmetry breaking, we have a single scalar field b(x) which corresponds to a spinless boson of mass $\sqrt{2}$m and a vector field B_μ corresponding to a vector boson of mass $\sqrt{2}\phi_0$ with three independent components. Higgs (1964) and others [5] pointed out this mechanism of introducing mass into the theory. The particle corresponding to the scalar field b(x) is known as the Higgs boson. The breaking of local symmetry enables the gauge field to acquire mass seen in section 1.4 which replaces the massless spin-zero Goldstone boson that appeared in global symmetry breaking in section 1.2.

1.4 SU(2) symmetry and symmetry breaking and fermion mass generation

Yang and Mills (1954) [8] were the first to explore the idea of constructing a lagrangian density that is invariant under local SU(2) transformation as well as a local U(1) transformation. If two component fields are introduced,

$$\Phi = \begin{pmatrix}\Phi_a \\ \Phi_b\end{pmatrix} \tag{1.4.1}$$

with Φ_a and Φ_b, complex scalar fields of the form $\Phi_a = \phi_1 + i\phi_2$ and $\Phi_b = \phi_3 + i\phi_4$ giving four real fields in total. The lagrangian density Eq. 1.2.2 has global U(1) × SU(2) symmetry with respect to the new fields,

$$\Phi^\dagger\Phi = \Phi_a^*\Phi_a + \Phi_b^*\Phi_b = \phi_1^2 + \phi_2^2 + \phi_3^2 + \phi_4^2$$
$$\partial_\mu\Phi^\dagger\partial^\mu\Phi = \partial_\mu\phi_1\partial^\mu\phi_1 + \partial_\mu\phi_2\partial^\mu\phi_2 + \partial_\mu\phi_3\partial^\mu\phi_3 + \partial_\mu\phi_4\partial^\mu\phi_4$$

The U(1) and SU(2) global symmetries are transformed into local symmetries in the Standard Model. U(1) transformation can be written as $\Phi \rightarrow \acute{\Phi} = e^{(-i\beta\tau^0)}\Phi$, where τ^0 is a unit matrix. In order to make it a local symmetry, we need to introduce a gauge field $A_\mu(x)\tau^0$ such that $A_\mu(x) \rightarrow \acute{A}_\mu(x) = A_\mu(x) + (2/g1)\partial_\mu\beta$. Any SU(2) element can be written in the form $U = e^{-i\alpha^k\tau^k}$, with τ^k being the three group generators identical to the Pauli spin matrices and α^k three real numbers. A gauge vector field $W_\mu{}^k(x)$ for each generator τ^k is needed to be introduced in order for the global SU(2) symmetry to become a local symmetry that will follow the appropriate transformation laws. Then we also need to define:

$$D_\mu\,\Phi = [\partial_\mu + (\frac{ig1}{2})A_\mu + (\frac{ig2}{2})W_\mu]\Phi\,. \tag{1.4.2}$$

The locally gauge invariant lagrangian density corresponding to Eq. 1.2.2 becomes

$$\mathscr{L}_{\phi} = (D_{\mu}\,\Phi\,)^{\dagger}\,D^{\mu}\,\Phi\,-V(\Phi^{\dagger}\,\Phi). \tag{1.4.3}$$

The above lagrangian density will be invariant under Lorentz transformation if W_{μ} and A_{μ} transforms as covariant four-vectors. Defining a field strength tensor $B_{\mu\nu}$ for the case of a gauge field B_{μ} we have

$$B_{\mu\,\nu}\,=\partial_{\mu}\,B_{\nu}\,-\partial_{\nu}\,B_{\mu}\,, \tag{1.4.4}$$

and let the dynamical contribution of the lagrangian density be -$\frac{1}{4}B_{\mu\nu}\,B^{\mu\nu}$. The introduction of the field strength tensors adds some complications to the W_{μ} gauge fields due to the non-Abelian nature of the SU(2) group. The field strength tensor will then take the form

$$W_{\mu\nu}\,=[\partial_{\mu}\,+(ig_2\,/2)W_{\mu}\,]W_{\nu}\,-[\partial_{\nu}\,+(ig_2\,/2)W_{\nu}\,]W_{\mu}\,. \tag{1.4.5}$$

Under an SU(2) transformation, $W_{\mu}\rightarrow W'_{\mu}$ and

$$W_{\mu\nu}\,\rightarrow W'_{\mu\nu}\,=UW_{\mu\nu}\,U^{\dagger}\,. \tag{1.4.6}$$

The total dynamical contribution to the lagrangian density associated with the gauge fields is

$$\mathscr{L}_{dyn} = -\frac{1}{4}\,B_{\mu\nu}\,B^{\mu\nu}\,-\frac{1}{8}\,Tr(W_{\mu\nu\,W^{\mu\nu}}). \tag{1.4.7}$$

which translates to

$$\mathscr{L}_{dyn} = -\frac{1}{4}\,B_{\mu\nu}\,B^{\mu\nu}\,-\frac{1}{4}\,W^{3}_{\mu\nu}\,W^{3\mu\nu}\,-\frac{1}{2}\,W^{-}_{\mu\nu}\,W^{+\mu\nu}\,. \tag{1.4.8}$$

Eq. 1.4.6 makes the total dynamical contribution to the lagrangian density associated with the gauge fields in Eq. 1.4.7 invariant under a local SU(2) transformation. To break the SU(2) symmetry, the potential in Eq. 1.2.3 $V(\Phi^{\dagger}\Phi)$ becomes:

$$V(\Phi^{\dagger}\Phi) = \frac{m^2}{2\phi_0^2}\,[\phi_1^2\,+\phi_2^2\,+\phi_3^2\,+\phi_4^2-\phi_0^2\,]^2\,. \tag{1.4.9}$$

With ϕ_0 being a real parameter as in Eq. 1.2.3. Eq. 1.4.8 is the vacuum state of our system which shows that it is degenerate in the four-dimensional space of the scalar fields. To break the SU(2) symmetry, the α^k(x) can be used. They are the three real parameters specifying the element of SU(2), adopting a gauge for any field configuration Φ_A = 0 (two conditions) and Φ_B is real (one condition), the ground state becomes:

$$\Phi_{ground} = \begin{pmatrix} 0 \\ \Phi_0 \end{pmatrix} \tag{1.4.10}$$

and the excited states takes the form

$$\Phi_{excited} = \begin{pmatrix} 0 \\ \Phi_0 + h(x)/\sqrt{2} \end{pmatrix} \tag{1.4.11}$$

with h(x) being a real field. Under U(1) × SU(2) transformation, the fields in Eq. 1.4.11 are unchanged and still retain a local U(1) symmetry which is the symmetry of electromagnetism. Expressing the locally gauge invariant lagrangian density for the excited states Eq. 1.4.9 in terms of the field h(x), the potential in Eq. 1.4.3 becomes:

$$V(\Phi^\dagger \Phi) = m^2 h^2 + \frac{m^2 h^3}{\sqrt{2}\,\phi_0} + \frac{m^2 h^4}{8\phi_0^2} \equiv V(h); \tag{1.4.12}$$

and (1.4.3) takes the form

$$\begin{aligned} \mathscr{L}_\Phi = \frac{1}{2}\,\partial_\mu h\,\partial^\mu h + \frac{g_2^2}{2}\,W_\mu^-\,W^{+\mu}\,(\phi_0 + h/\sqrt{2})^2 \\ +[\frac{g_2^2}{4}\,W_\mu^3\,W^{3\mu} - \frac{g_1 g_2}{2}\,W_\mu^3\,B^\mu + \frac{g_1^2}{4}\,B_\mu\,B^\mu\,](\phi_0 + h/\sqrt{2}\,)^2 - V(h) \end{aligned} \tag{1.4.13}$$

simplifying further gives

$$\begin{aligned} \mathscr{L}_\Phi = \frac{1}{2}\,\partial_\mu h\,\partial^\mu h + \frac{g_2^2}{2}\,W_\mu^-\,W^{+\mu}\,(\phi_0 + h/\sqrt{2})^2 \\ +\frac{1}{4}\,(g_1^2 + g_2^2) Z_\mu\,Z^\mu\,(\phi_0 + h/\sqrt{2})^2 + V(h)\,. \end{aligned} \tag{1.4.14}$$

The full lagrangian density takes the form $\mathscr{L} = \mathscr{L}_\Phi + \mathscr{L}_{\rm dyn}$ which is expressed as $\mathscr{L} = \mathscr{L}_1 + \mathscr{L}_2$ where $\mathscr{L}_1$ in Eq. 1.4.15 is the lagrangian density of the free massive neutral vector boson field $Z_\mu(x)$, the free massive neutral scalar boson field h(x), and a pair of massive charge vector boson fields $W_\mu^-(x)$ and $W_\mu^+(x)$ that are all interacting with the electromagnetic field $A_\mu(x)$.

$$\begin{aligned} \mathscr{L}_1 = \frac{1}{2}\,\partial_\mu h\partial^\mu h - m^2 h^2 - \frac{1}{4}\,Z_{\mu\nu}\,Z^{\mu\nu} \\ +\frac{1}{4}\phi_0^2\,(g_1^2 + g_2^2)\,Z_\mu\,Z^\mu - \frac{1}{4}A_{\mu\nu}A_{\mu\nu} \\ -\frac{1}{2}[(D_\mu\,W_\nu^+)^* - (D_\nu\,W_\mu^+)^*][D^\mu\,W^{+\nu} - D^\nu\,W^{+\mu}] + \frac{1}{2}g_2^2\,\phi_0^2\,W_\mu^-\,W^{+\mu} \end{aligned} \tag{1.4.15}$$

$\mathscr{L}_2$ in Eq. 1.4.16 is the sum of the remaining interaction terms

$$\begin{aligned}\mathscr{L}_2 = (\frac{1}{4}h^2 + \frac{1}{\sqrt{2}}h\phi_0)(g_2^2\, W_\mu^-\, W^{+\mu} + \frac{1}{2}(g_1^2 + g_2^2)Z_\mu\, Z^\mu) \\ -\frac{m^2h^3}{\sqrt{2}\phi_0} - \frac{m^2h^4}{8\phi_0^2} + \frac{g_2^2}{4}(W_\mu^-\, W_\nu^+ - W_\nu^-\, W_\mu^+)(W^{-\mu}\, W^{+\nu} - W^{-\nu}\, W^{+\mu}) \\ +\frac{ig_2}{2}(A_{\mu\nu}\, sin\theta_w + Z_{\mu\nu}\, cos\,\theta_w)(W^{-\mu}\, W^{+\nu} - W^{-\nu}\, W^{+\mu}) \\ -g_2^2\, cos^2\,\theta_w\,(Z_\mu\, Z^\mu\, W_\nu^-\, W^{+\nu} - Z_\mu\, Z^\nu\, W_\nu^-\, W^{+\mu}) \\ +\frac{ig_2}{2}\, cos\,\theta_w\,[(Z_\mu\, W_\nu^- - Z_\nu\, W_\mu^-)(D^\mu\, W^{+\nu} - D^\nu\, W^{+\mu}) \\ -(Z_\mu\, W_\nu^+ - Z_\nu\, W_\mu^+)\,(D^\mu\, W^{+\nu})^* - (D^\nu\, W^{+\mu})^*]\,. \end{aligned} \tag{1.4.16}$$

Upon symmetry breaking, most of the U(1) $\times$ SU(2) symmetry that existed is lost, $\mathscr{L}_2$ has no trace of the original SU(2) symmetry. The W_μ^+, W_μ^-, and Z_μ are three vector fields with corresponding particles W^+, W^-, and Z, the physical bosons of the broken symmetry which have acquired mass and are the mediators of the weak interaction, the photon remain massless because the U(1) symmetry is still unbroken. The spontaneous symmetry breaking of the other groups does not affect the SU(3) symmetry of the strong force yielding gluons that are massless just like the photons.

In the case of fermions, an invariant $SU(2)_L \otimes U(1)_Y$ invariant Yukawa lagrangian is introduced [9] of the form:

$$\mathscr{L}_f = -|\lambda_f|\,\bar{\psi}_L\,\Phi\,\psi_R + h.c \tag{1.4.17}$$

and repeating the same procedure as above. The masses of the femions are subsequently identified as the constant coefficients,

$$M_f = \frac{|\lambda_f|v}{\sqrt{2}} \tag{1.4.18}$$

with λ_f being the Yukawa coupling of the higgs, which is proportional to M_f, which is the mass of the fermion.

1.5 New physics scenarios probed in this thesis

The Standard Model offers an effective low energy description of all confirmed collider data. Even with the successes of the Standard Model, there are still some open questions such as the origin of particle mass, why there are so many different types of matter particles, why quark and neutrino flavours mix the way they do, origin of charge-parity (CP) violation, the dominance of matter over antimatter in our present universe, the nature of dark matter, unification of fundamental forces. These open questions are the reasons to expect some physics beyond the Standard Model.

In the Standard Model, the neutrino masses are zero, it does not include singlet field

implying no Dirac mass terms, it has no scalar triplets implying no Majorana mass terms, it is renormalizable and quantum corrections can not generate Majorana mass terms due to baryon-lepton (B-L) number symmetry. The discovery of neutrino masses and mixings became an important milestone in the history of particle physics and is the first evidence of the existence of new physics beyond the Standard Model. Neutrino masses can be generated by adding light or heavy fields to the Standard Model. When light fields are added, the neutrinos generated will be too heavy and will require some mechanism to suppress them, while adding heavy fields will give very light neutrinos consistent with the observed neutrino masses.

By adding a new heavy field per family which is the Standard Model at low energy while at high energy, this new field exist which introduces non-renormalizable terms to the action of the Standard Model and give light neutrinos. These terms are suppressed by the ratio of $\frac{\nu}{M_R}$, where ν is the Standard Model vacuum expectation value of the Higgs which characterizes the weak scale and M_R is the unknown scale of new physics $\equiv$ Grand Unification Theory (GUT). As a result, the Standard Model has two more terms $M_R\overline{N_R^C}N_R$ + $h_\nu\overline{L}HN_R$ + h.c. added to it. The neutrino masses are generated by dimension 5 operators. The second term generates the Dirac mass (M_D) of neutrinos with $M_D \approx h_\nu\nu$ and M_R which is the Majorana mass term is $>> M_D$. The neutrino mass matrix (left and right-handed neutrinos) can be represented in the form

$$M_\nu = \begin{pmatrix} 0 & M_D \\ M_D & M_R \end{pmatrix} \tag{1.5.1}$$

Where M_D and M_R are 3×3 matrices. After diagonalizing the above mass matrix, we arrive at a light neutrino mass matrix of the form

$$M_\nu = -\frac{M_D^2}{M_R} \tag{1.5.2}$$

Since we have already noted that M_R can be much larger than M_D. This is known as the seesaw mechanism and it provides natural explanation why neutrino masses are small. More detail of this search is in section 4.1.

The fundamental fermions of the Standard Model (quarks and leptons) exist in three generations, comprising of two members. Flavour is a property that distinguishes the fundamental fermions with each other. One of the most interesting consequence of the Standard Model is the universality of lepton flavour (LFU). LFU is an accidental symmetry that is broken only by Yukawa interactions and states that the electroweak bosons couple with the same strength to the three families of leptons. Any violation of LFU is a clear indication of new particles being involved in quark flavour changing processes, affecting their dynamics. Experimental data shows several anomalies in the flavour sector (B-decays) and these anomalies hint at lepton non universality. The single leptoquark search is aimed at addressing these anomalies in the flavour sector and also offer an explanation to the recent muon g-2 result. A detail introduction is given in section 5.1.

2. The Large Hadron Collider and the ATLAS experiment

This chapter will describe briefly the CERN accelerator complex with focus on the Large Hadron Collider (LHC) together with its four main experiments. It will be followed by a more detailed overview of the ATLAS detector and the section will be concluded with detector simulation. The goal of the ATLAS [10] detector at the Large Hadron Collider (LHC) is to observe particles coming from the high energy proton-proton and heavy ion collisions to find signatures for new physics and also study standard model processes at very high energy scale.

2.1 Physics at the LHC

At the LHC, we are interested in studying Standard Model processes at unprecedented high energy scales and also to search for signs for new physics not explained by the Standard Model i.e, physics beyond the Standard Model (BSM). By exploring with this high energy scale, we hope to understand why the generation of fermions with such corresponding masses, the mechanism for electroweak symmetry breaking, nature of forces, existence of dark matter, absence of antimatter in the observed universe leading to the observed matter-antimatter asymmetry unaccounted for by the Standard Model, charge-parity (CP) violation, Cabibbo - Kobayashi - Maskawa (CKM) mixing matrix with such range of values [4, 11, 12]. Most of the LHC physics studies rely on excellent particle identification capability. This is needed because some of the decay modes are characterized by small-cross sections and large backgrounds.

Proton-proton collision at the LHC result in the production of charged and neutral particles. The charged particles leave their characteristic tracks in the inner detector (ID). Both the charged and neutral particles deposit their energies in the calorimeter. A jet is a collection of these energy deposits in calorimeter cells which is reconstructed to correspond to the original quark or gluon. Jet algorithms defines how these energy deposits are grouped. These are clustering algorithms which groups high transverse momentum (p_T) objects into pairs first before combining the whole objects in the cluster. The Standard Model measurements, new physics beyond the Standard Model searches and the Higgs discovery have all shown how important a good electron reconstruction and identification is to the success of these ATLAS searches [13–15].

2.2 The Large Hadron Collider

The LHC is a 27 km synchroton used for accelerating and colliding protons at a designed center-of-mass energy of 14 TeV, making it possible to study fundamental particles and interactions. The LHC also accelerates and collides heavy ions for the studies of quark-gluon plasma. It has four main detectors: ATLAS (A Toroidal LHC Apparatus), CMS (Compact Muon Solenoid), LHCb (LHC beauty) and ALICE (A Large Ion

Collider Experiment) [10, 16–18]. These experiments are designed differently with different physics applications. ATLAS and CMS are general purpose detectors for various physics programs including the studies of Standard Model processes at high energies and also the search for beyond the Standard Model (BSM) physics. ALICE detector is dedicated for studying Quark Gluon Plasma from heavy ion (PbPb) collisions. LHCb focus mostly on the physics of beauty and charm quarks by investigating the differences between matter and antimatter.

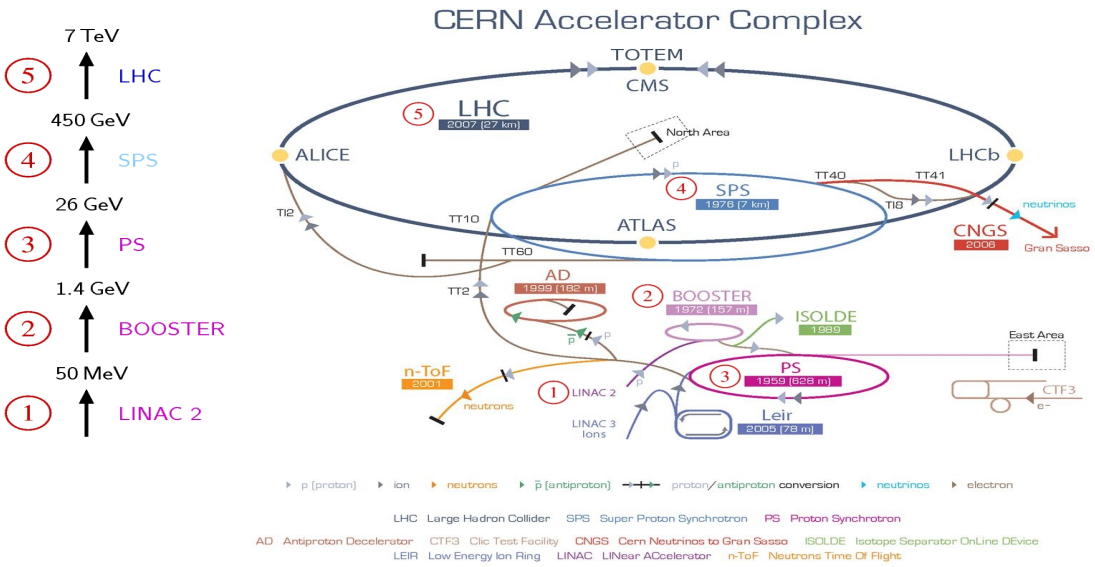


Figure 2.1: *The CERN accelerator complex [19].*

The LHC is currently housed in a tunnel that was previously used for the Large Electron-Positron (LEP) collider [20] consisting of 1232 dipoles and 392 quadruple magnets for focusing the beams and keeping them in a circular orbit. The temperature of 1.9 K is maintained around the superconducting magnets using liquid helium as the cooling system. An 8.3 T magnetic field is created by the magnets making it possible for protons to be accelerated up to 14 TeV center of mass energy. The protons go through several step acceleration chain seen in Figure 2.1 so as to reach this energy. The protons are produced in the Duoplasmatron by removing electrons from hydrogen gas and these protons are injected into the LINAC2, which is a linear accelerator that accelerates the protons to 50 MeV. The protons go into the Proton Synchroton Booster (PSB) with this energy, where they are accelerated to an energy of 1.4 GeV. They are then injected into the Proton Synchroton (PS) from the PSB and accelerated to 26 GeV. They are moved from the PS to the Super Proton Synchroton (SPS) where they are accelerated to 450 GeV before they are injected into the LHC ring. In the LHC, they are further accelerated to an energy of 7 TeV. The proton beams at this energy, are ready for collision at the collision points, which is the center of the detector depending on the physics being studied. The LHC beam is designed for a luminosity (a measure of the number of collisions produced in a detector per cm^2 per second) of 10^{34} $cm^{-2}s^{-1}$.

It has 2808 bunches containing approximately 1.1×10^{11} protons in each bunch. The bunch spacing is equivalent to approximately 25 ns between collisions and a the rate of bunch crossing is 40 MHz. This high luminosity and high energy of collisions makes the LHC the most powerful accelerator.

In Run 2 (2015 - 2018) The LHC has delivered a total integrated data luminosity of 156 fb^{-1}. Figure 2.2 shows a comparison to that recorded by ATLAS. A comparison of the integrated luminosity measured at the ATLAS collision point from Run 1 (2011-2012) to Run 2 is shown in Figure 2.3.

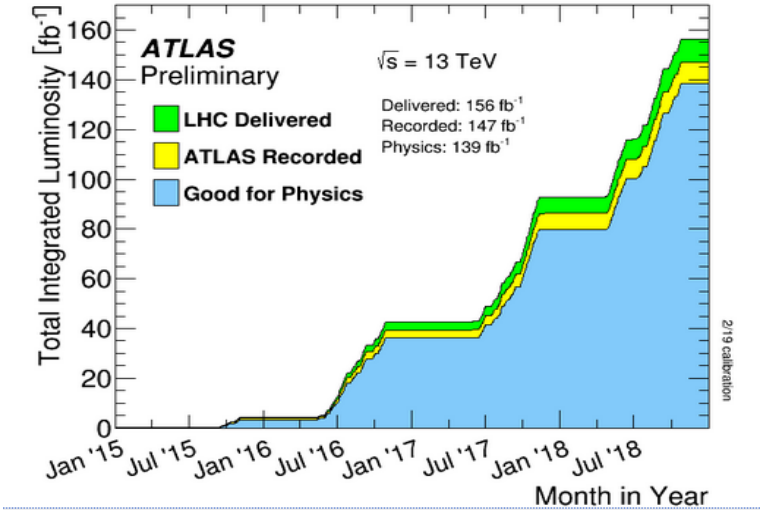


Figure 2.2: *Total cumulative luminosity delivered by the LHC shown in green with yellow depicting what was recorded by ATLAS while the blues is what is available for physics analysis [21].*

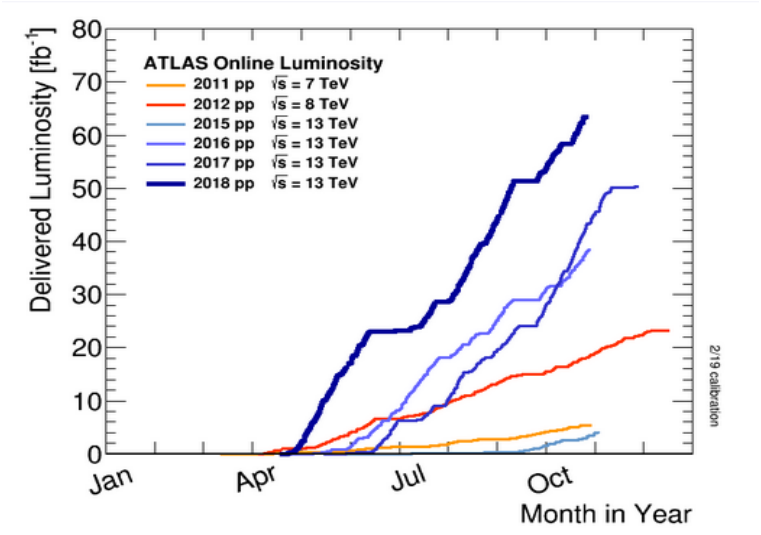


Figure 2.3: *Integrated luminosity versus day for Run 1 and Run 2 delivered to ATLAS [21].*

2.3 Overview of the ATLAS Detector

The ATLAS detector [10, 22, 23] has a forward-backward symmetric cylindrical geometry covering almost 4π in solid angle. From the inner to the outer along the transverse plane, this detector consists of the inner tracking detector (ID), superconducting solenoid, electromagnetic (EM) calorimeter, hadronic calorimeter and the muon spectrometer that is surrounded by the toroid magnet system. Along the longitudinal axis, the endcaps of this cylindrical detector are covered with Liquid-Argon (LAr) hadronic calorimeters, toroid magnets and the muon spectrometer. A cut-away section of the ATLAS detector is seen in Figure 2.4.

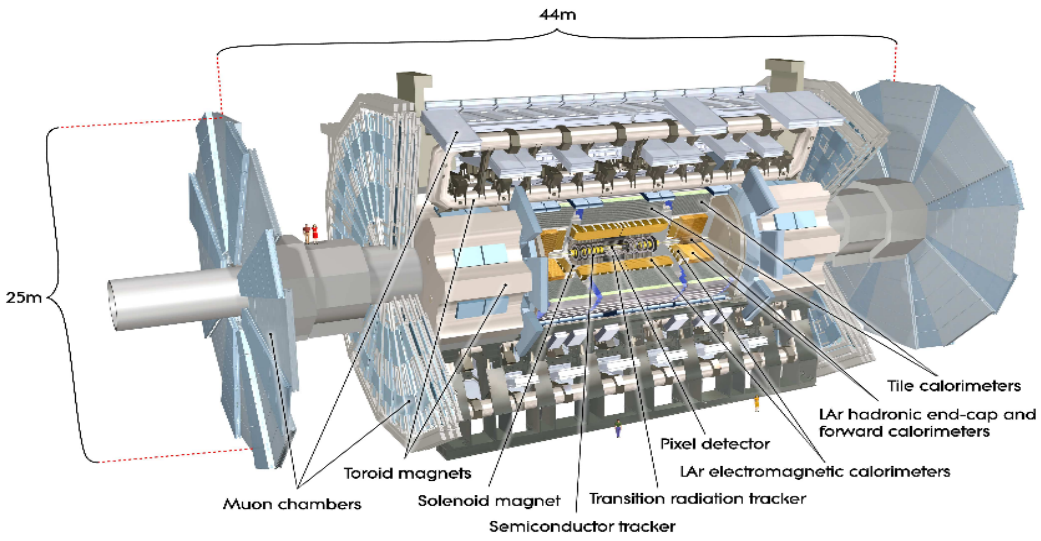


Figure 2.4: *A cut-away section through the ATLAS detector [10].*

2.4 Coordinate system in ATLAS

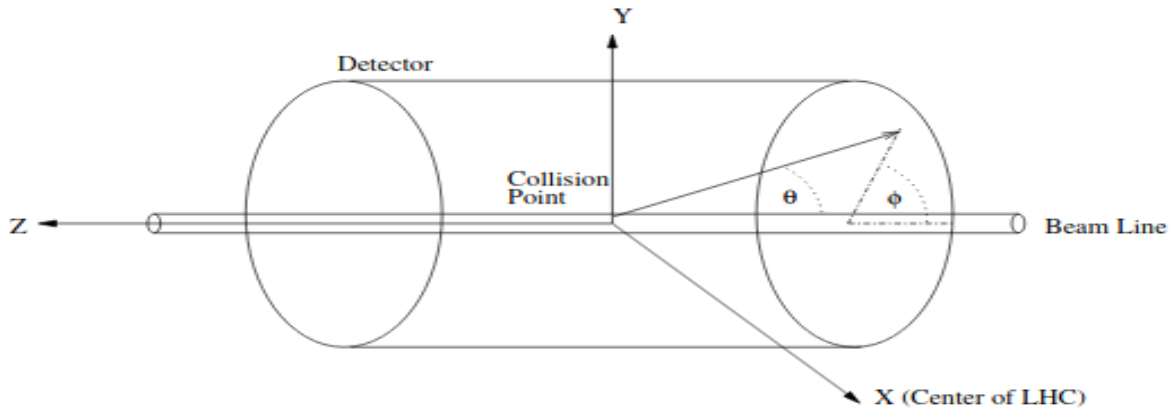


Figure 2.5: *Illustration of the ATLAS coordinate system [24].*

ATLAS uses a right- handed three-dimensional coordinate system with origin at the proton-proton or heavy ion interaction point at the center of the detector (IP) as seen in Figure 2.5.

- z-axis: along the beam pipe (beam direction).
- y-axis: points upwards perpendicular to the LHC ring plane.
- x-axis: direction from the IP to the center of the LHC ring.

The azimuthal angle ϕ and polar angle θ are our usual polar coordinates, (r, ϕ) are the two cylindrical coordinates used in the transverse plane. To describe the 4-momentum of any particle, E, p_T, η, ϕ are used. where E is the energy of the particle. The momentum in the transverse plane denoted by p_T is defined as

$$p_T = \sqrt{{p_x}^2 + {p_y}^2}.$$

η is the pseudo-rapidity which is defined in terms of the polar angle θ as

$$\eta = -\ln \tan(\theta/2)$$

The pseudo-rapidity is the rapidity of a massless particle. Rapidity is defined as

$$y = \frac{1}{2}\ln(\frac{E + p_z}{E - p_z})$$

The reason why pseudo-rapidity is used is because it is Lorentz boost invariant. The angular separation between two objects in pseudo-rapidity and azimuthal space is defined as

$$\Delta R = \sqrt{\Delta\eta^2 + \Delta\phi^2}$$

2.5 The ATLAS Inner Detector (ID)

The ATLAS ID [10, 25] is the innermost section of the ATLAS detector and is used for locating charged particles. It is designed to ensure excellent momentum resolution and also excellent pattern recognition as well as a good measurement of primary and secondary vertex for charge particle tracks [26, 27] of a p_T threshold of 0.5 GeV even though it may be lower depending on the studies and covers a pseudorapidity range of $|\eta| < 2.5$ [10]. The ID seen in Figure 2.6 is composed of a pixel and silicon microstrips covering $|\eta| < 2.5$ surrounded by a transition radiation tracker enabling electron identification within $|\eta| < 2.0$ pseudorapidity range. The pixel detector was the nearest detector to the beam pipe designed to carryout precise measurement such as impact parameter and decay vertices and also to perform with high granularity. The pixel detector is made up of 4 barrel layers and 6 disk layers(3 for each endcap). Between Run 1 and Run 2, a new inner pixel was added [22] at an approximate sensor radius of 3.3 cm, this is the IBL [23]. The aim is to improve the impact parameter and primary vertex information by providing hit information that has very high resolution. The ID is immersed in a 2 T axial magnetic field produced by a superconducting solenoid enabling tracking upto $|\eta| < 2.5$.

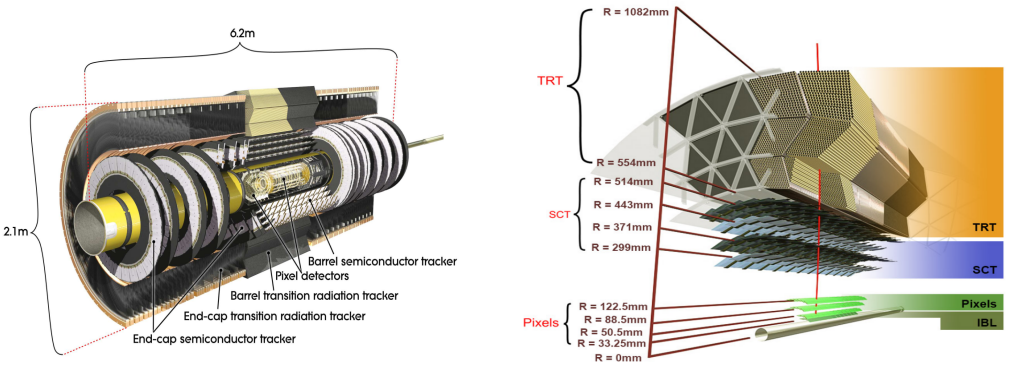


Figure 2.6: *Left:A barrel view of the ATLAS inner detector. Right: layout of the ATLAS inner detector with insertable B-Layer (IBL) [28].*

2.6 The Calorimeter System

Next to the ID is the Calorimeter system covering $|\eta| < 4.9$ in pseudorapidity aimed at measuring the energy of photons, electrons and hadrons. An overview of this system is seen in figure 2.7. The electromagnetic (EM) calorimeter both in the barrel and end-cap regions is made of fine-granularity lead/liquid argon (LAr). The EM calorimeter is segmented radially into three different η - ϕ (granularity sections). The first is the strips which has fine segmentation in η. The strips are able to distinguish between the showers that are initiated by a photon or electron from those initiated neutral pions. Most of the energy measurement is provided by the second sampling which has fine segmentation in ϕ and η. The last layer is the third sampling which increases the dept of the calorimeter has coarser segmentation. See Figure 2.8 for a cut-away section

showing the different layers of the EM barrel calorimeter. The EM calorimeter provides a pseudorapidity coverage of $|\eta| < 3.2$ and measures precisely the energies and positions of photons and electrons.

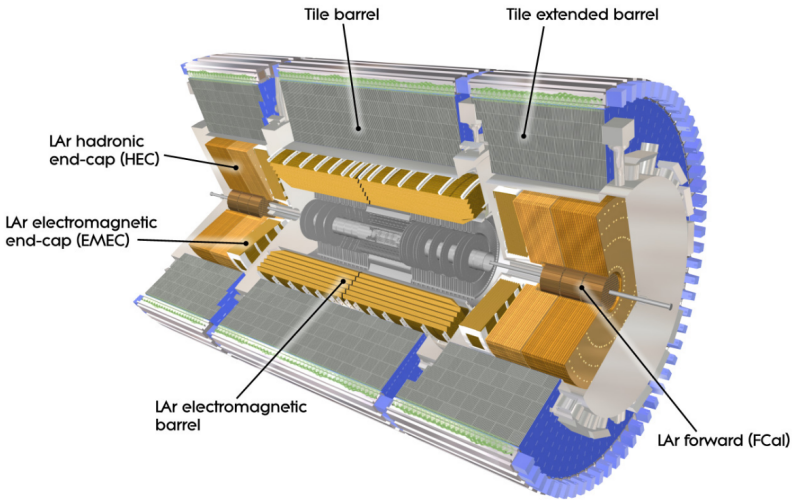


Figure 2.7: *A cut-away view of the ATLAS calorimeter system [10].*

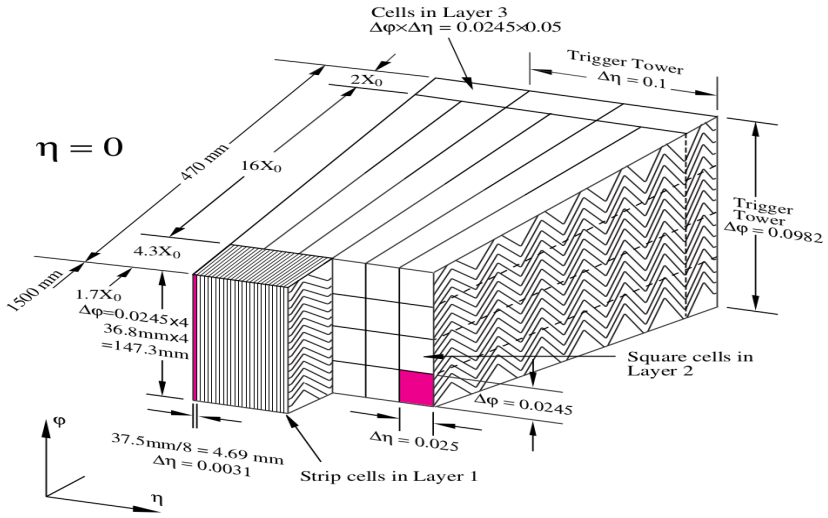


Figure 2.8: *Sketch of the section through the LAr EM barrel with showing the different layers and also showing the granularity in ϕ and η for the cells of the 3 layers [10].*

The energy of hadrons is measured by the tile and LAr hadronic end-cap. The tile calorimeter covers the range $|\eta| < 1.7$. The scintilator-tile calorimeter is composed of the barrel and 2 extended barrel regions. In the region $1.5 < |\eta| < 3.2$ which is the end-cap, the hadronic calorimeter use LAr. The LAr forward calorimeters measure both hadronic and electromagnetic energy deposites thereby extending the pseudorapidity

coverage of the calorimeter to $|\eta|$= 4.9.

2.7 The Muon Spectrometer System

Surrounding the calorimeter system [10] is the muon spectrometer for measuring the position of muons and infer their momenta as they move through the detector. The layout is shown on Figure 2.9. The muon spectrometer works in an air core toroid magnetic system which bend the tracks of muons. The large barrel toroid ensure magnetic bending within the range $|\eta| < 1.4$, while within $1.6 < |\eta| < 2.7$, two smaller end-cap magnets in both ends of the barrel toriod are responsible. The combination of barrel and end-cap fields ensure muon tracks bending in the region $1.4 < |\eta| < 1.6$. The muons position in the barrel region is measured in three chambers that are arranged in cylindrical layers around the axis of the beam. The muon positions are measured over most of the η range by Monitor Drift Tubes, MDTS [29]. Cathode Strip Chambers (CSCs) are used in the range $2 < |\eta| < 2.7$ [30]. Incorporated in the muon spectrometer system is the muon triger system for muon identification from the interactions of proton-proton (pp) or heavy-ion (HI) [31]. This muon trigger chamber covers the range $|\eta| < 2.4$ in pseudorapidity with resistive plate chambers [32] used for the barrel and thin gap chambers [33] for the end-cap regions. The system is designed to operate with high efficiency and low transverse momentum (p_T) thresholds for muons [31].

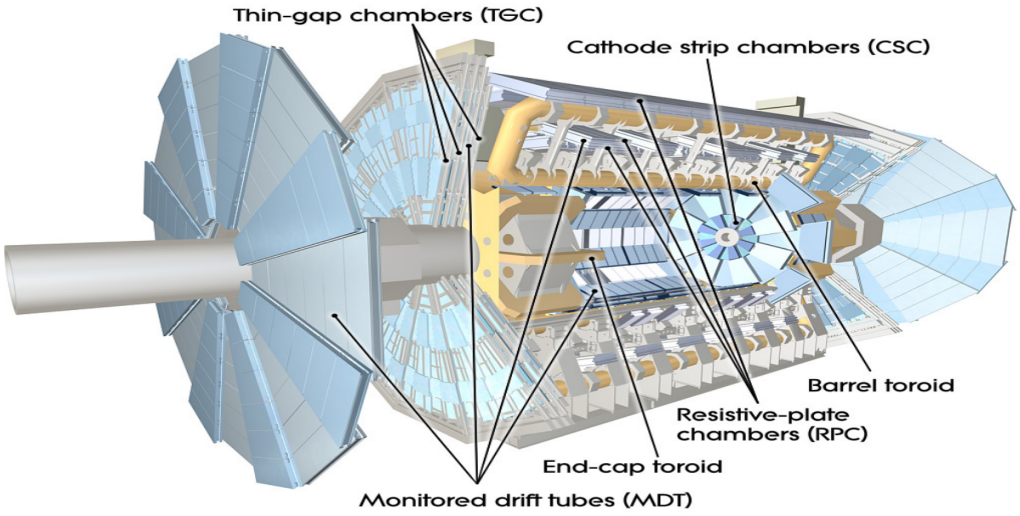


Figure 2.9: *A cut-away view of the ATLAS muon system [10].*

2.8 Event simulation in hadron collisions

Quarks and gluons are collectively referred to as partons. When two quarks interacts, the energy stored in the gluon field increases with increase in distance between the quarks, and it requires more energy to keep the pair separated (asymptotic freedom). This is responsible for the absence of free quarks or gluons in nature. The gluon field is

able to create a pair of quarks if it is sufficiently large. Colour charged quarks can emit gluons the same way charge particles can radiate photons. Similarly, a gluon can split into a pair of quark − antiquark similar to a photon creating electron − positron pair. A single parton as a result of this can usually lead to a shower of partons which eventually combine to form colour-neutral hadrons (hadronization). As the shower traverses the ATLAS detector, they deposite their energy before hadronising and the energy flow of the colour partons is approximated to the colour neutral hadrons formed and this collection of colour neutral hadrons is called a jet. This is why jets are proxies for quarks and gluons even though it is difficult to point the origin of the hadrons. This is because hadrons that originate from the initial/final state radiation (I/FSR), multiple parton interaction (MPI) and pileup would will inevitably become part of the jets regardless of how these jets are formed. When a parton emits other partons before and after a QCD interaction vertex, it results into initial and final state parton showers. I/FSR also includes photon radiation due to QED. MPI is when more than one parton pairs interact in a proton − proton collision due to the composite nature of the protons. Pileup is when there are multiple interactions in a bunch crossing of existence of effects from the preceding or subsequent bunch crossing.

Protons are made up of two up quarks and one down quark (valence quarks) bounded together by the strong force through gluon exchange. In addition to the valence quarks there is a sea of quarks and gluons (partons) due to the gluon's ability to split into a pair of quark-antiquark or more gluons. Due to the composite nature of protons, the event structure at hadron collider becomes significantly complex, and in order to describe the full final states, multi-particle calculations must be involved since most processes are effectively 2→ n processes. Where n is the number of final state particles and not all of them are directly created from the hard scatter process or calculable from the matrix element. Starting with a simple 2→ 2 process which defines approximately the directions and energy of the hardest partons, and subsequently adding simple parton branchings in order to build up the complete event structure (final state). This approach determines the structure of the energy flow in the even without modifying the total cross section and it is known as the parton shower (PS) approach [34, 35]. It is independent of the physics process generating the initial partons (quarks and gluons).

In the case where the complete event is generated with PS generator at leading order (LO), a k-factor is often calculated which is the ratio of the theoretical cross-section at next-to-leading order (NLO) or next-to-next-to leading order (NNLO) over the cross section at LO. This k-factor is used to reweight the event without any event regeneration with higher order accuracy. This does not account for difference in kinematics due to higher order effects. The DGLAP (Dokshizer Gribov Lipatov Altareli Parisi) equation governs the branching processes q→qg, g→gg, and g→$q\bar{q}$ and the Sudakov form factors [36] gives the probability that a branching will occur at a given time. Each branching must be at small angles and the emitted parton is required to have a small energy fraction of the original parton (collinear and soft safety) in order to ensure that these perturbative approaches are valid. The branching of partons can occur both before and after a QCD interaction vertex which will result into initial and final state parton showers respectively.

Parton shower begins at an energy scale close to Λ_{QCD}, evolving down from the hard scale. Then the energy scale further decreases with each branching, with subsequent new branches starting at lower energy scales. This evolution continues until the parton energy scale reaches Λ_{QCD}, which is the point when the showering process terminates upon entering the low-momentum regime where perturbative QCD can no longer hold because this is a long-distance regime where confinement starts taking effect, the partons then combine through hadronization forming color-neutral objects before interacting with the ATLAS detector. So in essence, not all the final state particles are directly created from most of the hard scatter processes at hadron colliders, because at the hardest interaction (HS) scale, only a few partons, and particles are present and only 1 parton each is involved in the HS processes, but as the hardness scale reduces, these hardest partons split, producing a cascade (shower) of more partons through fragmentation by perturbative QCD. Fragmentation and hadronization is a process that occurs after the termination of the shower and this process converts the partons to hadrons, which are detected by the detector. This is non-perturbative and occurs outside the radius of the proton. The hadrons may further decay depending on their lifetimes. Figure 2.10 shows a complete event generation for a Z +jets process in a simulated proton-proton collision.

The interaction of the resulting particles (hadrons, mesons, electrons, photons) with the calorimeters causes a further cascade of low momentum particles. Combining information from the different parts of the detector enables us to identify the particles present in that collision. In other to build the complete event structure, the energies and directions of the hardest parton are approximated and simple partons branchings are added in a successive manner. This is how a parton shower is constructed in theory using different Monte-Carlo event generators. Local parton-hadron duality hypothesis [37] is the general approach adopted for hadronization. It is based on the principle that the quantum numbers and four-momentum (E^2 - P^2) at the hadronic level must flow from the already established at partonic level.

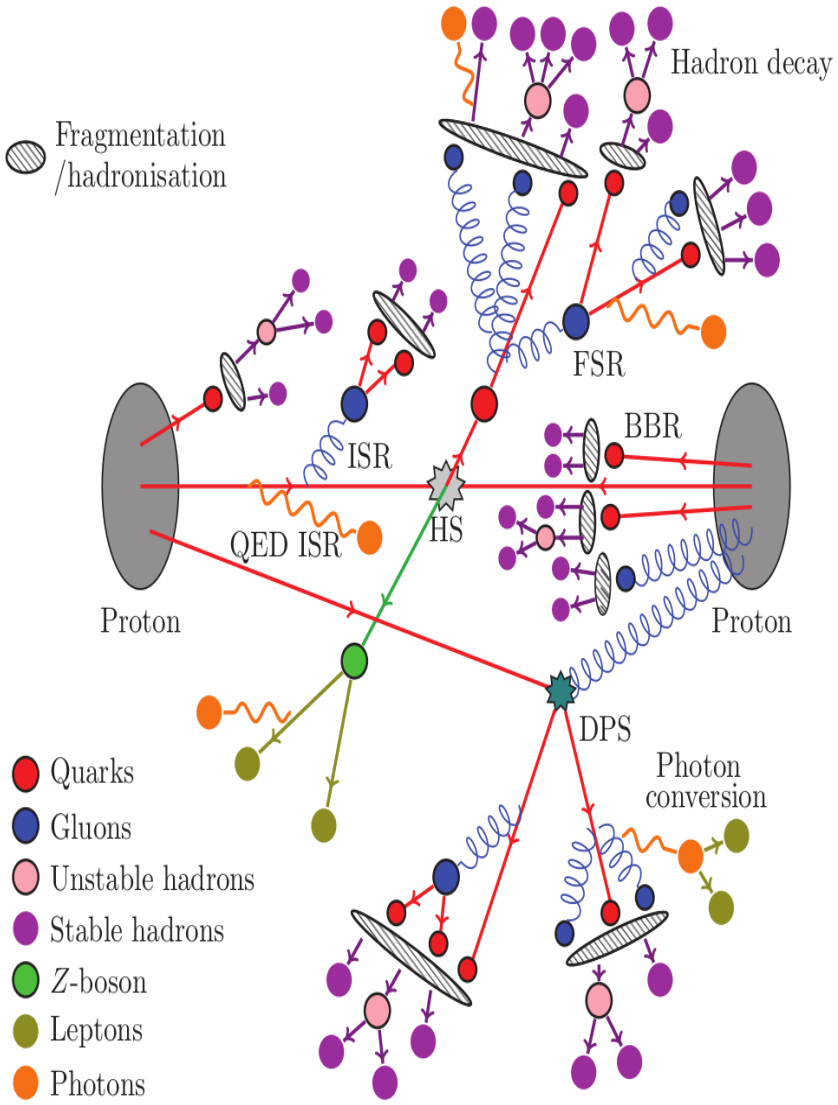


Figure 2.10: *A schematic diagram of a complete event generation by a Z + jets process. The hard scatter (HS)in grey star led to a Z boson and a quark being produced. The boson decays into oppositely charged leptons of the same flavour with one of the leptons emitting a photon. The quark creates a parton shower through final-state-radiation (FSR), forming stable and unstable hadrons. The QED initial-state-radiation (ISR) results into a photon, while the QCD initial state radiation results into hadrons. The beam-beam remnants (BBR) also results into hadrons. The secondary scatter (DPS) represented by the teal star, produces two quarks with each producing its own parton shower and in the end resulting into hadrons. The radiated photon from the gluon converts into electron-positron pair. [38].*

3. Event Reconstruction in ATLAS

3.1 ATLAS trigger system

The limitation in data storage and flow capacity from the proton-proton collisions necessitate the use of triggers in the acquisition of data. These triggers are designed so as to only record potentially interesting events while discarding less interesting ones which constitutes a major chunk of the events from these collisions. The ATLAS trigger system shown on Figure 3.1 is made up of triggers arranged in successive levels with events selected from the preceding level becoming input for the next level. The Level-1 trigger (L1) uses information from the calorimeter and the muon triggers (designed to identify jets with high momentum and electroweak objects). The decision time for this trigger is of the order of 2 μs making it operate under strictest time constraint reducing the data rate from 40 MHz to 100 KHz [39]. The Events from L1 are processed by the Level-2 trigger (L2) after receiving Regions of Interest (ROIs) information from the L1. A sliding window algorithm is used in identifying these ROIs by summing the total energy that is deposited within a η-ϕ square window and it is triggered once this sum exceeds some certain energy thresholds. Next to this is the Level-3 trigger (L3) known as the high level trigger (HLT). This trigger carries out detailed analysis of the complete event data by also using tracking information from the inner detector to selects events with one or two leptons or a jet that meets some p_T threshold value. The HLT is allowed longer computing time and receives full information from the various subsystems of the detector in order to reconstruct physics objects in addition to other event variables.The average size of the event file from the HLT is $\approx$ 1.5 MB, if recording is at the rate of 1 KHz, this will result into tens of Gb/s which is transported to CERN data center and stored on the Worldwide LHC computing grid. During Run 2, the grid was storing $\approx$ 50-70 PB of data which is expected to increase by an order of magnitude at least with high-luminosity LHC (HL-LHC) [40].

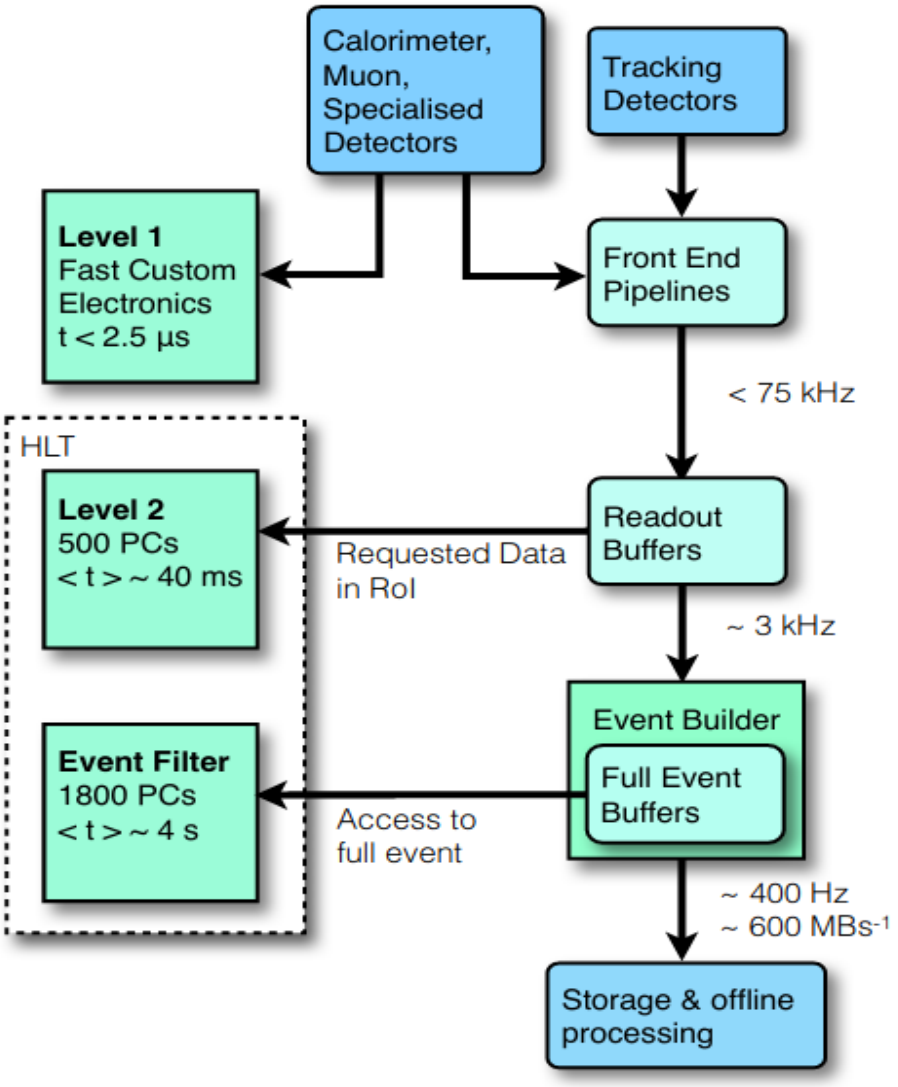


Figure 3.1: *The ATLAS trigger system [41] in Run 2.*

3.2 Electron reconstruction

The electrons in the ATLAS detector [10] are characterized by some unique signatures which enable them to be identified and reconstructed. Several steps are involved in electron reconstruction in the central region i.e $|\eta| < 2.47$ of the ATLAS detector because of the signatures that electron leave in several components of the detector as it traverse this detector as seen in Figure 3.2:

- Seed-Cluster Reconstruction: A sliding window with a fixed size of 3×5 in

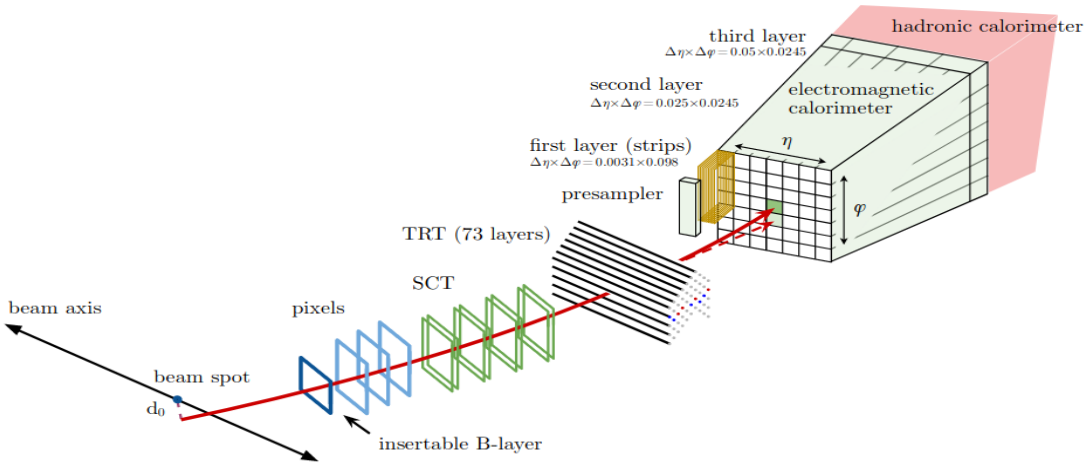


Figure 3.2: *A diagram showing the path of an electron moving through the ATLAS detector. The hypothetical path of the electron is the red trajectory which shows the electron first traversing through the tracking system (pixel detectors, followed by the silicons-trip and lastly through the TRT) afterwards it enters into the electromagnetic calorimeter where it deposits most of its energy. Due to the interaction of the electron with the TRT a photon is produced represented by the dash red trajectory [42].*

units of 0.025×0.025 (in $\eta \times \phi$ space) is used to search for EM topo cluster "seeds". This window corresponds to the granularity of the middle layer of the EM calorimeter, and searches are made for longitudinal towers that have total cluster transverse energy (E_T) greater than 2.5 GeV. The clustering algorithm is then used to form clusters around the seed and this algorithm enables duplicates to be removed [43]. An extended window that is dependent on the calorimeter cluster position which uses 3×7 cells in the barrel and 5×5 cells in the endcap is used to reconstruct the kinematics of the cluster. The sliding window moving with the dimension above gets centered on an adjacent tower, the process of seed cluster reconstruction is repeated for every tower. The efficiency range of this cluster search is from above 99% for E_T =15 GeV to 96% at E_T =7 GeV [44].

- Electron track reconstruction: This process is made up of two steps: Recognition of pattern and fitting of electron track. The standard ATLAS pattern recognition is based on the pion hypothesis (this is because most of the tracks are generated by charged pions [45]) when accounting for energy loss as a result of particle interactions with the material in the detector [46]. This has been modified into a pattern recognition algorithm that allows for about 30% energy loss due to bremsstrahlung for each intersection of the track of the particle with the detector material. Using the pion hypothesis, when a track seed of P_T greater than 1 GeV (made up of three hits in various layers of the silicon detector) fails to be extended successfully into a full track of at least seven hits, and it is found to be within one of the regions of interest of the EM clusters, an electron hypothesis

which allows for larger energy loss is carried out as a second pattern recognition attempt. These two hypothesis enables tracks with $P_T > 400$ MeV to be fitted to either of them depending on the hypothesis used with the help of the ATLAS Global χ^2 track fitter [47]. This is how the standard track reconstruction have been incorporated with the electron algorithm to improve the performance of the electron and also limit interference with the reconstruction of the main track.

- Specific electron track refit: The reconstructed tracks are extrapolated to loosely match the EM cluster in $\eta \times \phi$ space in the middle layer of the calorimeter and the barycenter of the cluster. The condition $|\eta_{cluster} - \eta_{track}| < 0.05$ and also $0.10 < |\phi_{cluster} - \phi_{track}| < 0.005$ must be satisfied. The design of the asymmetric matching condition in ϕ is designed to account for energy loss from bremsstrahlung. Tracks are refit with an optimized Gaussian sum filter (GSF) to account for non-linear bremsstrahlung effect after satisfying the loose track match to EM cluster and also having not less than four precision hits [48]. The GSF improves the parameters of the tracks such as the transverse impact parameter significance and the signed impact parameter significance.

- Electron candidate reconstruction: The electron reconstruction procedure is completed after a successful matching of the clustered seed to the tracked candidate. The refit procedure is carried out similarly but with more strict conditions. In a situation where more than one track satisfies this condition, then one of the tracks is chosen as the primary track depending on the algorithm, using information from cluster-track distance evaluated with different momentum hypotheses, the number of pixel hit and also the existence of a hit in the first layer of the silicon layer [49]. Any electron candidates without tracks associated with at least four-pixel hit or SCT layers are considered as photons and as a result, dropped from the group of electron candidates, also each member of this group is screened for tracks associated with a secondary vertex with no pixel hit, any candidate found to satisfy this condition, it is classified as a photon which is likely to have come from photon conversion and as a result, also dropped from the group. In instances whereby the electromagnetic cluster is already reconstructed, the above criteria become the only source of loss in the efficiency of the electron reconstruction. Additional classification is carried out using the electron's candidate information such as existence of a pixel hit, E/P, p_{T} and also information about the secondary vertex. This classification is carried out to ascertain if the object is being considered exclusively as an electron candidate or the object is a photon candidate as well as an electron candidate. In the case of the former, it must have:

- The absence of matched secondary vertex
- The value of $\mathrm{E/P} < 10$
- A track with $p_{\mathrm{T}} > 2$ GeV and at least 1 pixel hit
- The presence of a secondary vertex should fail one of the following criteria:
  - A conversion of more than 40 mm from the secondary vertex
  - Several or none of the tracks with hits in the innermost pixel layer

– It is a double silicon vertex

3.3 Jet reconstruction

A jet is a collection of collimated bunches of hadrons with each bunch coming ideally from a single parton. A jet algorithm maps a set of hadrons into a set of jets with four momenta. In order to form jets, the inputs must first be identified. These are clusters of energy deposits in the calorimeter or the currently used which is the object formed by combining the energy deposit and track information (particle flow or Pflow objects). Stable final state particles or partons can be used in simulation as inputs to form jets. The identified input objects are then collected based on some distance criteria which determines the size of the jet. The chosen jet algorithm determines which input object goes into which particular jet. The distance parameter R used is equivalent to the opening angle in the coordinates of the collider. The jet algorithm is required to satisfy several criteria such as: the physics interpretation of the event should be independent of the clustering algorithm, the clustering algorithm should be independent of the design and structure of the detector, although it is not always possible, the clustering algorithm should have minimal sensitivity to hadronization, underline events, pileup, they are also required to be easy to inplement and execute and in addition they are required to be infrared (IR) and collinear safe so as not to have divergent cross-sections in perturbative calculations. Infrared safety means that any soft gluon added shouldn't change the results of the jet clustering while collinear safety is the unchanging of the jet clustering from the splitting of a parton into two collinear partons.

Previously, topological clusters of the calorimeter cells are the primary inputs used in jet reconstruction in ATLAS. The seed cells of these clusters are cells with four times the energy expected due to electronic and pile-up noise [50] while adjacent cells that are clustered with the seed are expected to have an energy that is two times the expected energy due to pile-up and electronic noise with the noise due to pile-up dominating in the current data taking conditions [51]. The topological clustering method used previously by ATLAS cannot separate energy deposits from different particles and also a large proportion of low-energy particles are unable to seed their own clusters. Currently the Pflow algorithm is used during jet reconstruction which removes the calorimeter energy deposits due to charge hadrons during jet reconstruction. The remaining calorimeter energy deposits and tracks matched to the particle flow objects are then used to reconstruct the jet. Pflow uses signals from the inner tracker and the calorimeter (see Figure 3.3) and results in improved charged-hadron measurement and improvements in the pile-up stability and resolution [52]. The anti-k_t [53] algorithm, which is a form of a sequential recombination algorithm is typically used by ATLAS to reconstruct jets, using information from the pflow algorithm. The anti-k_t algorithm is such that in event consisting of some hard particles with transverse momenta p_{t_k}, p_{t_l}.... that are well separated and also many soft particles. The distance between a hard particle k and a soft particle l is

$$d_{kl} = Min(p_{T_k}^{-2}, p_{T_l}^{-2})\Delta R_{kl}^2 / R^2$$

and the distance between particle k and the beam direction is

$$d_{kB} = p_{T_k}^{-2}$$

In clustering, the smallest value among d_{kl} and d_{kB} is determined and if it is the d_{kl}, then k and l inputs are merged, however if the smallest is d_{kB}, then the kth input is considered a jet and it is no longer considered as an input. This continues until all the inputs are clustered as jets. Typically, these jets are the small radius (small-R) jets R = 0.4 primarily used by ATLAS for physics searches. There are large radius (large-R) jets R = 1.0 used for studying the physics of massive particles decaying with high transverse momenta. For the case of large-R jets, the last step is jet grooming to remove pile-up topological clusters from the jet. This jet algorithm combines the hardest and softer inputs in close proximity and does not allow for the modification of the shape of the jet by soft particles (infrared safe). It is also collinear safe because splitting of one parton into two partons does not change the result of the jet clustering. The anti-k_t jet algorithm results in hard regular (circular) jets with only softer jets exhibiting more complex shapes when compared to other jets algorithm as seen in Figure 3.4.

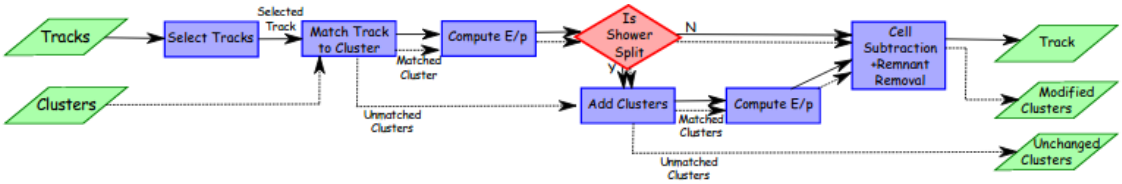


Figure 3.3: *A flow chart of the particle flow algorithm showing the steps involved and the inputs. At the end, charged particles, topoclusters not modified by the algorithm and remnants of topo-clusters whose part of their energy have been removed will remain [52].*

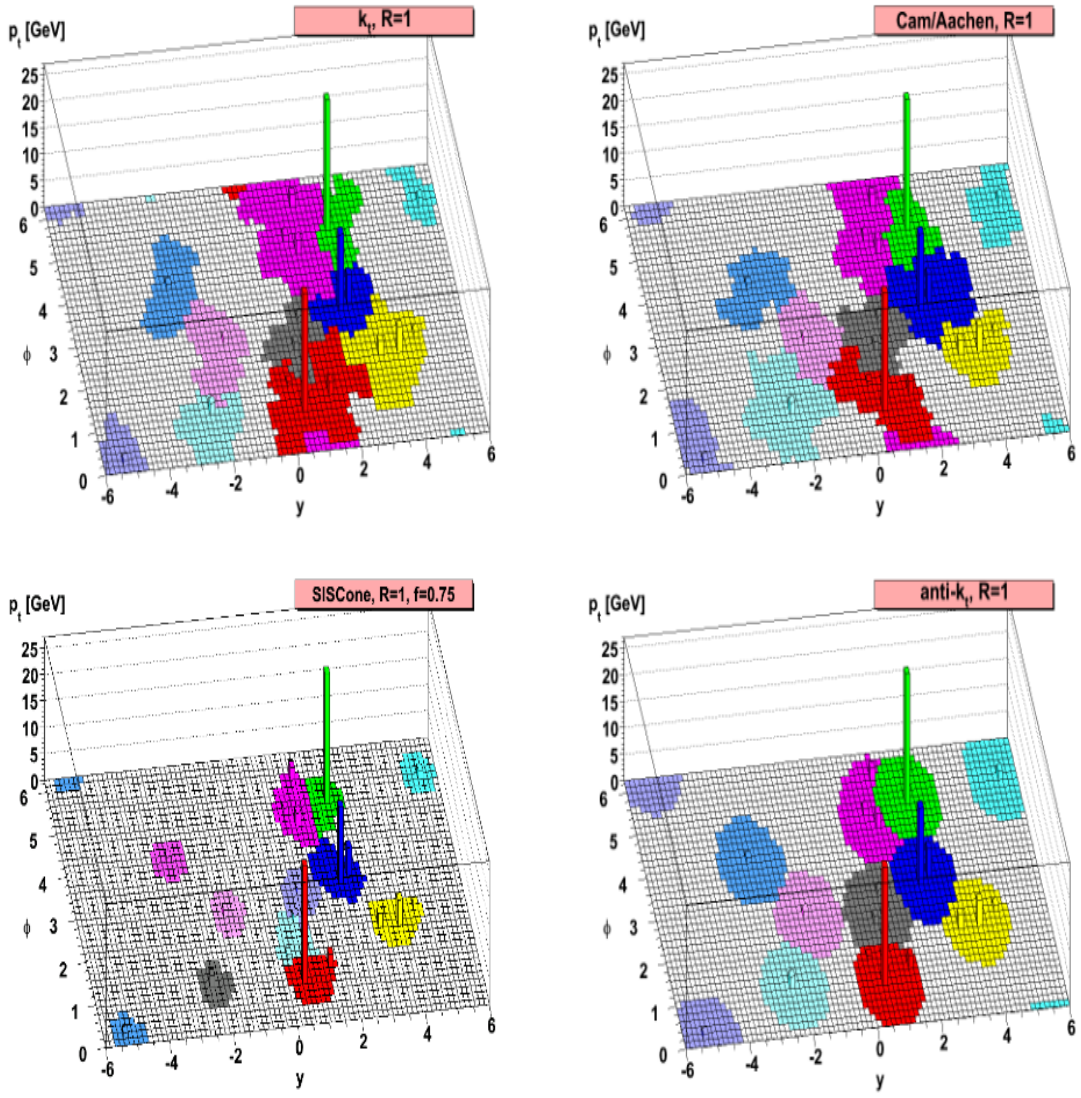


Figure 3.4: *Jets obtained with the k_t (top left), Cambridge–Aachen (top right), SIScone (bottom left) and anti-k_t (bottom right) with radius 1.0. The colour is only showing individual jets according to the algorithm[53].*

4. Boosted right-handed heavy neutrino search

The SM of particle physics is by no means complete due to limitations outlined in section 1. There are many proposed extensions of the Standard Model theory (BSM theories) aimed at addressing the shortcomings of the Standard Model. There are different BSM models with different signatures depending on their final-state topologies. Experimentalists involved in the search for new physics, hoping to observe rare processes have to devise and adopt novel techniques to search for this new physics signals which have low cross section and are hidden by large background. Unexplored kinematic regimes and final states may be hiding new physics. In this chapter, a search for new physics is presented. This search is aimed at addressing the question of small neutrino masses which is not explained by the SM of particle interactions

4.1 Introduction

There have been several important developments in the past decades at the theoretical and experimental frontiers aimed at explaining neutrino mass generation. An approach that is widely adopted to explain small neutrino masses is the so-called seesaw mechanism [54], where dimension 5 operators give Majorana mass to light neutrinos through electroweak symmetry breaking. The seesaw mechanism can be simply categorized into classes such as Type-I [55–57], Type-II[58–60], and Type-III[58, 61]. Type-I and Type-II models can be further be embedded into the Left-Right Symmetric Model (LRSM) [62–64]. The LRSM contains a right-handed boson W_R and SM-singlet heavy neutrinos N_R that are introduced as parity gauge partners of the corresponding left-handed neutrino fields.

The natural set-up for the seesaw mechanism is provided by the LRSM framework, which offers features such as parity symmetry at high energy, parity violation within the Standard Model, mass generation of light and heavy neutrinos, and the right-handed charged current existence. With this model, small neutrino masses can be explained. It also supports the coexistence of contributions from both Type-I and Type-II seesaws.

Searches by the ATLAS [65–67] and CMS [68–71] collaborations have considered LRSM final state signatures with two charged leptons and two jets and have excluded up to several TeV the mass regions of the parameter space for m_{W_R} and m_{N_R}, with m_{W_R} and m_{N_R} denoting the masses of the W_R and N_R respectively. The 6.7 TeV bound for m_{W_R} from the ATLAS dijet search [72] is applicable to this model. However, no exclusion limits above this value exist for hierarchical masses, i.e, $(m_{N_R}/m_{W_R}) \leq 0.1$. This analysis is complementary to the resolved channel analysis in ATLAS [73] and is performed with the full Run 2 data set.

This analysis uses a high-mass right-handed (RH) gauge boson W_R, a feature of the LRSM [62–64, 74], which decays into a Majorana heavy neutrino(N_R) through the

Keung-Senjanovic process [75], as shown in Figure 4.1. The focus of this search is in a regime where the W_R is much heavier than the N_R ($m_{N_R} / m_{W_R} \leq 0.1$), and investigates an alternative signature for $W_R \rightarrow N_R$ following [76]. In this regime, the Majorana neutrinos produced are highly boosted. Subsequently, their decays via off-shell W_R to jets, i.e., $N_R \rightarrow \ell^{\pm}$ j j are highly collimated all forming a single large radius neutrino jet (j_N). The signature of the final state becomes $\ell^{\pm}$ j_N rather than the complementary resolved final state of $\ell^{\pm}\ell^{\pm}$ j j [66].

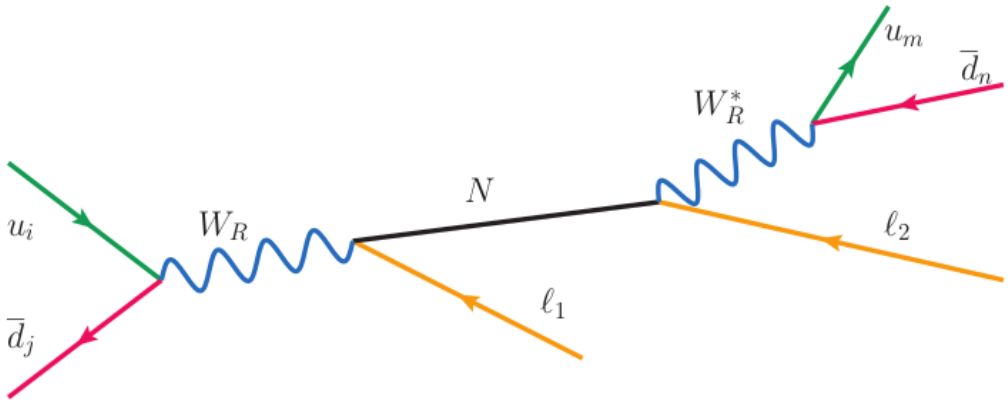


Figure 4.1: *Feynman diagram of the production of W_R in a proton-proton collision and decay via the N_R to quarks and charged leptons [67]. The leptons have to be of the same flavor and maybe opposite or the same charges.*

This search is applicable to other LRSM variations containing leptons and a right-handed gauge boson such as inverse seesaw models [77], in addition, it can also be applied to R-parity-violating supersymmetry[78, 79] where a resonantly produced selectron decays subsequently into a neutralino and an electron, with the former decaying through a non-zero λ' coupling into quarks and a lepton. If the neutralino is boosted, its decay products can be reconstructed as a single large-radius jet, similar to the final state probed in this analysis.

4.2 Analysis strategy

The definition of objects, events selection, and triggers adopted in this analysis are motivated by the ATLAS partial Run 2 boosted heavy neutrino paper [67] and other well-established analyses. The selection of electrons and jets follows the ATLAS partial Run 2 boosted heavy neutrino paper. So in the electron channel, the electron coming from the decay of N_R will be inside the large-radius jet, meaning that the large-radius jet will be the N_R. The addition of the leading p_T electron to the N_R will then result in the W_R. The masses of W_R and N_R are selected in this search as (m_{W_R}, m_{N_R}) = (3.5

TeV, 350 GeV), (4.5 TeV, 450 GeV), (5.5 TeV, 5500 GeV), (6.5 TeV, 650 GeV) with a ratio of $m_{N_R}/m_{W_R} \leq 0.1$.

4.3 Overview of the analysis

The key feature of this analysis is the use of a boosted large-radius jet (R = 1.0) to reconstruct part or all of the N_R depending on the channel. The quark and anti-quark initiated jets (R = 0.4) and the lepton (qql) which are the decay products of the N_R are required to be within the large-radius jet using the selection criteria in Section 5.5. In the electron channel, the large-radius jet acts as a proxy for N_R since the electron energy clusters are included in its reconstruction. Some difficulties arise in the event of the presence of a non-negligible fraction of EM clusters since the calibration of these clusters is done at local cell signal weighting (LCW) assuming potentially hadronic clusters:

- There might be an effect on the energy scale, calibration, and the resolution of the large-radius jet. It has been studied in [80] and the result showed no significant discrepancies. The study was done by comparing the performance of the large-radius jet from our signal sample with other large-radius jets such as from hadronic top-quark decay (qqb), from collinear W-boson decay from a jet (R= 0.4), (lq), and from leptonic top quark decay (bl). No isolation requirement is imposed on the sub-leading electron
- The standard overlap removal method is meant to prevent double-counting of objects and as a result, it will remove any electron with $\Delta R < 0.4$, and since a large proportion of our signal event falls within this ΔR, The standard overlap removal is not applicable to this analysis because it will remove a large proportion of the signal events. In place of the standard overlap removal, a looser overlap removal criteria is adopted which uses $\Delta R < 0.04$. The study [80] showed that this looser overlap removal criteria is effective in isolating events with real jets close to an electron from events with misreconstructed jets.

The process of adding the four-vector of the N_R with the leading lepton's four-vector reconstructs the W_R. This is the main observable used in this analysis to determine the control region $m_{W_R} < 2$ TeV (region already excluded by published CMS and ATLAS searches) and the signal region $m_{W_R} > 2$ TeV.

4.4 Signal and background MC samples

The signal samples are generated with MADGRAPH [81] event generator at leading order and showered with PYTHIA8 [82] and NNPDF2.3LO parton distribution function (PDF) set [83] and the A14 tune [84]. It is assumed in this model that the heavy neutrino couples to the same flavour charge lepton in the production and decay, and there is no constraint on the charge lepton. The background processes considered are $t\bar{t}$, Z+jets, single top, W+jets, and diboson, summarized in Table 4.1. The cross-sections of the $t\bar{t}$ sample are scaled to next-to-leading order (NNLO) in perturbative QCD and

next-to-leading-log (NNLL) accuracy [85] for soft gluon resummation, assuming the mass of the top quark is m_t = 172.5 GeV [86]. The h_{damp}(resummation damping parameter)in the POWHEG model that controls the matrix element matching to parton showers and also regulates the high-p_T radiation was set to $1.5m_t$. Z+jets, single top quark, and W+jets samples are scaled to the NNLO theoretical cross-sections [87–90]

Process	**Top quark**	**Z+jets**	**W+jets**	**Diboson**	**Single top**
Generator	POWHEG [91–94] +PYTHIA 8	SHERPA [95]			POWHEG +PYTHIA 8
ME order in pQCD	NLO	NLO			NLO
version	v2,8.186	2.2.1			v2,8.186
PDF (ME, PS)	NNPDF3.0NLO [83], NNPDF2.3LO [96]	NNPDF3.0NNLO			NNPDF2.3LO
PS tune	A14	default			A14

Table 4.1: *Overview of the simulated background samples.*

The full ATLAS detector simulation [97] based on GEANT4 [98] was used to process the background MC samples. These samples are then reconstructed and analysed using the same procedure and software used for data. In order to simulate pile-up(the effects of additional collisions from the same and nearby bunch crossings), additional proton-proton collisions were generated using PYTHIA8, with A2 tune [99] overlaid with MSTW2008 [100] PDF set.

4.5 Object and event selection

4.5.1 Definitions of objects

Electrons are reconstructed [101] using energy deposits in the EM calorimeter with associated ID tracks satisfying $|\eta| < 2.47$ excluding $1.37 < |\eta| < 1.52$ (EM calorimeter crack region). These electrons are required to have a $p_T > 26$ GeV and are identified using shower-shape, track-cluster match, and TRT criteria.

The leading electron candidate in this analysis is required to be isolated from the nearby hadronic activity and as a result, must satisfy loose isolation and medium likelihood identification criteria [102]. No isolation criteria is imposed on the sub-leading electron, but it required to pass the medium ID. The electron tracks are required to satisfy $|d_0|/\sigma d_0$ (track's impact parameter significance) < 5 and $|z_0| \sin\theta$ (longitudinal impact parameter) < 0.5 mm. A set of standard scale factors were applied to the MCs for electron efficiencies, reconstruction, trigger, and identification calculated as the ratios between the data and MCs. Smearing is applied to MC since the MC does not reproduce the resolution in data. In this high p_T range of this analysis, these standard scale factors are close to unity and have a negligible impact on this analysis.

Large-radius jet ATLAS uses noise suppressing topological clusters [50] to construct large-radius jets. Initially, topo-clusters are reconstructed at EM scale, by measuring the energy deposited in the calorimeter due to particles produced in the electromagnetic showers. The second method of building topo-clusters is by calibrating the calorimeter cell so that hadrons can be reconstructed correctly. Local cell signal weighting (LCW) method is used in this calibration which is aimed at improving the resolution compared to the EM scale by correcting signals due to hadronic deposits, hence correcting for effects like the non-compensation of the calorimeter response and inactive material [103]. The LCW method is base on the energy density and the longitudinal shower depth classifies topo-clusters either as hadronic or electromagnetic.

The anti-k_t algorithm [53] with R = 1.0 is used to reconstruct large-radius jets where the LCW calibrated topo-clusters are massless constituents. Further trimming [104] is done so as to remove the effects of underlying events and pile-up. This is a grooming technique where a k_t algorithm [105] of distance parameter R_{sub} = 0.2 is used to recluster the original constituents of a jet so as to produce a collection of sub-jets. Any sub-jet carrying less than a certain fraction (f_{cut}= 5%) of the original jet p_T, is discarded. The surviving jets are then recalibrated following a two-step procedure that corrects the jet energy scale followed by the correction of the jet-mass scale [103, 106]. The large-radius jet is required to have p_T > 200 GeV and be within $|\eta|$ <2.0.

Jets Particle flow objects are used to reconstruct jets using the anti-k_t algorithm [53] with R = 0.4 (radius parameter). Jets are required to have $|\eta|$ 4.4 and p_T > 25 GeV. Small-R jets have quality criteria applied to them, and events associated with jets that are consistent with the calorimeter noise or non-collision backgrounds are vetoed. In order to suppress pile-up jets predominantly found at low p_T, a jet vertex tagger is applied on jets with p_T <60 GeV and $|\eta|$ < 2.4 so as to select jets that originate at the primary vertex with high probability.

Overlap removal Electron and jet reconstruction process occur independently in ATLAS and as a result, an overlap removal procedure is applied to avoid double counting of physics objects. In the electron channel, the standard overlap removal approach is applied for the leading electron(highest p_T electron). In this approach, if there exists a small-R jet with ΔR(electron, jet) <0.2, the jet is rejected. Subsequently, if any electron is found within ΔR(electron, jet) < 0.4, the electron is rejected (this is because it is assumed that the jet originates from a real hadronic activity with the electron either coming from semileptonic decays inside the jet or is misreconstructed). The reason for the standard overlap removal approach is because every reconstructed jet and reconstructed electron share the same energy clusters. While the subleading (other) electron in this analysis which is inside the large-radius jet lies within ΔR = 0.4 of a small radius jet coming from the decay of the W_R. Applying the standard overlap removal to this electron will result in losing the signal event.

To address this, a modified overlap removal procedure is adopted. Here instead of removing electron within ΔR(electron, jet) < 0.4 as in the standard overlap removal, rather any electron within ΔR(electron, jet) < 0.04 of a jet is removed. This is based on the electron in jet performance study [80] where it was found that for non-isolated events, in most cases the electron ends up within ΔR > 0.04 of the reconstructed jet, as

part of the jet cluster is not shared with the electron.

4.6 Event selection

The data samples used in this analysis, collected from 2015-2018 during normal operation of the detector, corresponding to an integrated luminosity of 139 fb^{-1}. Only data that passed the final Good Run List (GRL) released by the Data Quality group for the periods was used and in addition, the electrons must pass though single-lepton triggers having p_T threshold of either 60 GeV or 140 GeV depending on the identification requirement. Table 4.2 summarizes the object selection citeria for the analysis.

Object	**Kinematic range**	**Quality**
Leading electron	$p_T > 26$ GeV, $\|\eta\| < 2.47$	Medium ID, Isolated
Subleading electron	$p_T > 26$ GeV, $\|\eta\| < 2.47$	Medium ID, Non isolated
Large-R jet	$p_T > 200$ GeV, $\|\eta\| < 2$, Mass > 50 GeV	

Table 4.2: *Criteria for selection of object for the analysis.*

Based on the signal topology, the selection of events is designed so as to optimize the selection of signal events while rejecting background events. Events with exactly two electrons are selected (without any charge requirement) and at least 1 large-R jet having $p_T > 200$ GeV, $|\eta| < 2$ and mass > 50 GeV. This mass cut helps to reduce the background since the sub-leading electron is part of the large-radius jet. The leading electron is required to be back-to-back in azimuth with the large -radius jet so as to balance the large-R jet, while the sub-leading electron is required to have ΔR (large-radius jet, sub-leading electron) < 1.0 so that it will be inside the large-radius jet. Events with dilepton invariant mass < 200 GeV are vetoed so as to reduce Z+jets backgrounds. The difference in ϕ ($\Delta\phi$) between the leading electron and subleading electron is required in order to further reduce Z+jets backgrounds. Simulation studies after applying these requirements show that the background consists predominantly of $t\bar{t}$ followed by Z+jets processes (with off-shell Z/γ^* production), While W+jets, single-top-quark, and multijet processes had a negligible contribution. No b-tagged jets requirement is applied in the analysis since the W_R signal can decay into a pair of top and bottom quarks. A 2 TeV blinding cut is applied on the m_{W_R}. This is the discriminating observable used in the analysis. The control region (CR) is the low m_{W_R} region which corresponds to the parameter space excluded by previous searches [107], while the signal region (SR) is the region of high m_{W_R} which in the background is evaluated from a combined fit of data and MC events in the CR. The different regions are defined in Table 4.3 based on the range of the reconstructed m_{W_R}.

Region	m_{W_R} Range	Lepton flavour
Signal Region (SR)	> 2 TeV,	Same flavour
Control Region (CR)	< 2 TeV	Same flavour

Table 4.3: *SR and CR region definition.*

4.7 The electron-in-jet identification study

In the usual ATLAS standard overlap removal process for electron and jet, if there exist any small radius jet within $\Delta R < 0.2$ of an electron, that jet is rejected because the electron's energy deposit in the EM calorimeter is always reconstructed as a nearby jet, meaning the nearby reconstructed jet is coming from the reconstructed electron. After this first overlap removal, if an electron is found to be within $\Delta R < 0.4$ of a jet, the electron is rejected. This is because it is assumed that the jet is from a real hadronic activity and the electron is either coming from semileptonic decays inside the jet or misreconstructed.

This study is motivated by the fact that the boosted heavy neutrino analysis [67] suffered a significant loss of signal selection efficiency seen in Figure 4.2. This is because the standard electron and jet reconstruction procedure in ATLAS occur independently and as a result, energy deposits due to an electron may end up being reconstructed as a jet, also a real jet may end up being reconstructed as a fake electron. To avoid this, the standard electron reconstruction and identification process use an overlap removal [108] procedure since every reconstructed electron will have a close by jet associated with it, that needs to be removed to avoid double-counting of these objects. Also if the electron has more jet close to it, the electron is discarded based on the assumption that the jet is a real jet coming from real hadronic activity. The standard electron reconstruction, and identification process is ideal for isolated electrons i.e electrons that are isolated from hadronic activity. The electron performance results from the process has been presented by the ATLAS Collaboration right from the inception of data taking in 2010 [109–111].

It is difficult to use such reconstruction and identification procedure in topologies where the electron and jet overlap like the boosted regime because in a boosted regime with jets and electrons in the final state such as semi-leptonic decays, some top-antitop pair decay modes and new physics model such as the ATLAS heavy neutrino analysis seen in Figure 4.3 [67], the electron can be very close to a real jet as seen in Figure 4.4. This makes it difficult to use the standard electron reconstruction and identification (ID) procedure and in addition, the standard efficiency scale factors are inadequate for such an electron because the are derived for isolated physics processes such as $Z \rightarrow ee$ and $J/\psi \rightarrow ee$ [42] events that have no nearby jets.

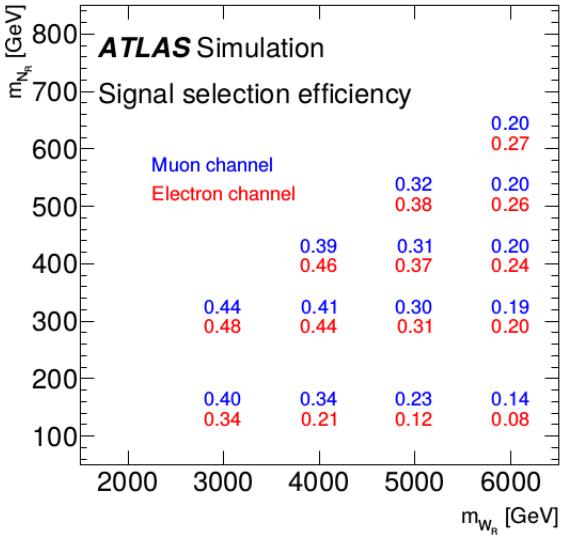


Figure 4.2: *Signal selection efficiency for a number of mass points using simulated signal samples at 80 fb^{-1} luminosity [67].*

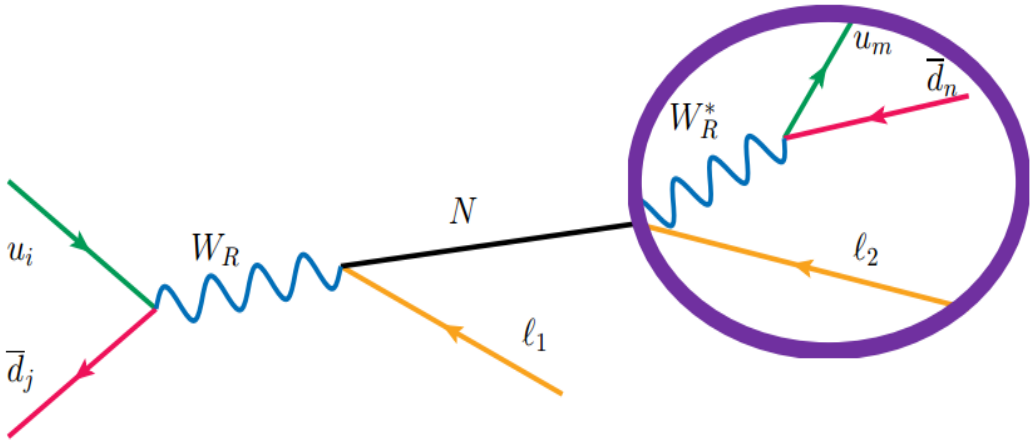


Figure 4.3: *Diagram of the W_R decaying via N_R into charged leptons and quarks. The purple circle indicating that the N_R decay products can be in a large-radius jet when they are boosted [67].*

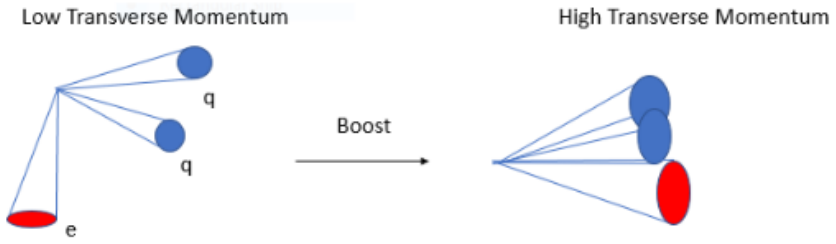


Figure 4.4: *Diagram showing how the decay products of the heavy neutrino system overlap as a result of the boosted nature of the heavy neutrino.*

This effect can be seen on the left of Figure 4.5 when comparing the efficiency in transverse energy (E_T) for an electron from Z→ee events (isolated electron) and an electron from the boosted neutrino (electron close to jet) using the standard electron ID. We can see a higher efficiency for the electron from Z→ee events than for the electron from the boosted neutrino. This trend is also seen when we compare the efficiencies of these 2 electrons in η seen on the right of Figure 4.5. We can see the efficiency plots as a function of ΔR (distance between jet and electron) for the electron in jet for different likelihoods. For all the likelihoods we can see a drop in efficiency inside the jet radius(jet radius is 0.4). This is because an electron is identified by shower shape variables that are calculated with respect to the barycenter of the electron cluster by summing all the surrounding cells. Any nearby jet will deposit some of its energy in some of these cells. This is what results in the drop in efficiency in ΔR seen in Figure 4.6.

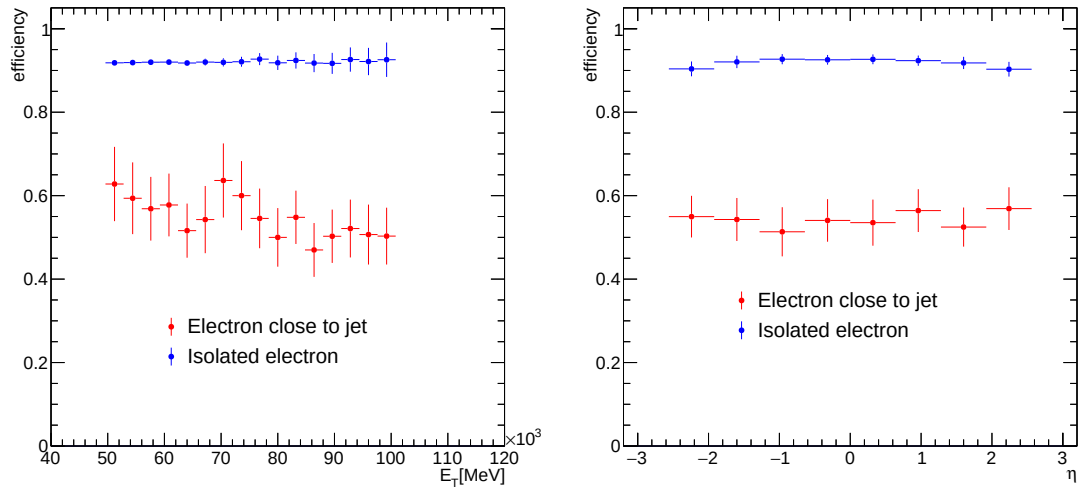


Figure 4.5: *Plot of Efficiency vs E_T and η for isolated electron and electron close to jet.*

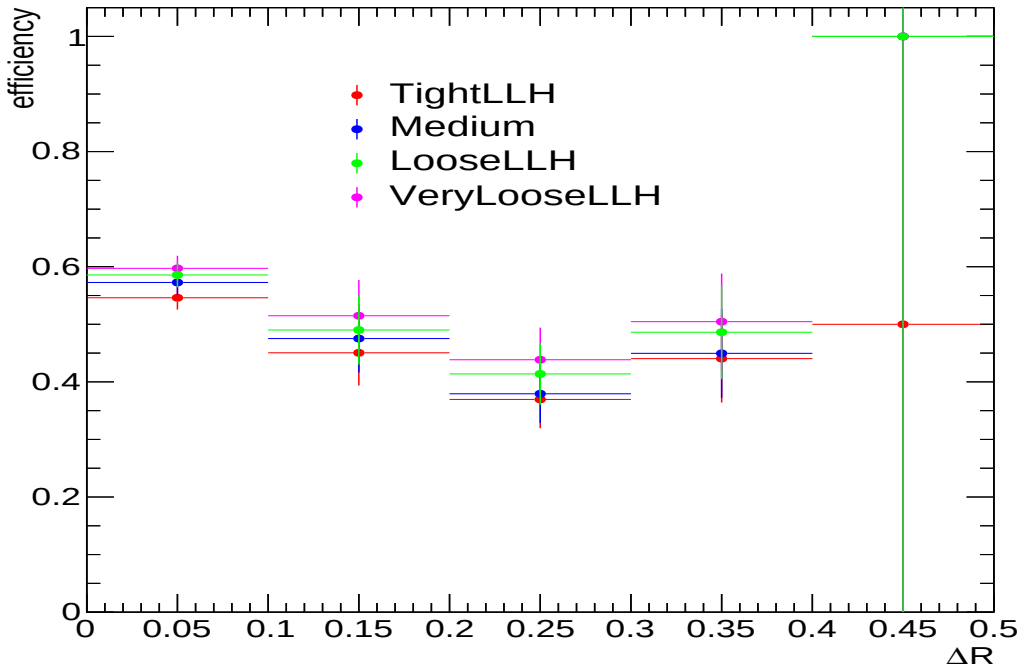


Figure 4.6: *Plots showing the efficiency as a function of ΔR for the electron close to jet for the different likelihoods.*

Several current ATLAS searches and measurements, especially in the boosted regime, suffer from this problem. We explored the possibility of a robust electron identification for this scenario. This study is aimed at improving the efficiency of the ATLAS full Run 2 boosted neutrino search and other future searches with this kind of topology.

4.8 Variables used in electron identification

In order to construct an electron ID that can be used for the identification of electrons in jets, the variables that are used in the standard electron ID were studied for an isolated electron and an electron close to jet. These are the discriminating variables that are used in electron identification in the central region of the ATLAS detector. The summary of the variables used in electron identification are summarized in Table 4.4.

Name	Description	Type
R_{had}	This is the ratio of E_T in the hadronic calorimeter to the E_T in the EM calorimeter.	Hadronic leakage
R_η	This is the ratio of energy in 3×7 cells over the energy in 7×7 cells centered at the position of the electron cluster.	Second layer of EM calorimeter
$w_{\eta 2}$	$w_{\eta 2}$ measures the lateral width of the shower. It is defined as $$w_{\eta 2} = \sqrt{\left(\frac{\Sigma E_i \eta_i{}^2}{\Sigma E_i}\right) - \left(\frac{\Sigma E_i \eta_i}{\Sigma E_i{}^2}\right)}$$ with E_i being the energy and η_i the pseudorapidity of the ith cell, with the sum calculated within a window of 3×5 cells.	Second layer of Electromagnetic (EM) calorimeter
R_ϕ	is the ratio of the energy in 3×3 cells to the energy in 3×7 cells with the center at the position of the electron cluster.	
f_3	is the energy ratio in the third layer to the total energy in the EM calorimeter.	Third layer of EM calorimeter
f_1	is the energy ratio in the first layer to the total energy in the EM calorimeter.	First layer of EM calorimeter
w_{tots1}	is the width of the shower in the first layer of the electromagnetic calorimeter. It is defined as $$w_{\text{tots1}} = \sqrt{\left(\frac{\Sigma E_i (i - i_{\max})^2}{\Sigma E_i}\right)}$$ with i running over all the strips in a $\Delta\eta \times \Delta\phi$ window of $\approx 0.0625 \times 0.2$ corresponding to 20 strips in η, and i_{max} is the highest energy strip index.	First layer of EM calorimeter
E_{ratio}	is the ratio of the difference in energy between the maximum energy deposit and the second maximum energy deposit in the cluster to their energy sum. This is evaluated in the first layer of the electromagnetic calorimeter.	First layer of EM calorimeter
d_0	is the transverse impact parameter relative to the beam line.	Track condition
$\lvert d_0 \rvert / \sigma d_0$	is the ratio of the d_0 to its significance.	Track condition
$\Delta p/p$	This is the ratio of the momentum lost by the track between the perigee and the last point of measurement with the momentum at the perigee.	Track condition
n_{Blayer}, n_{pixel},and n_{Si}	Number of hits in the innermost pixel layer, Number of hits in the pixel detector and Total number of hits in the pixel and SCT detectors.	Track condition
$\Delta\eta 1$	is the difference in η of the extrapolated track to the cluster position in the first layer.	Track-cluster matching
$\Delta\phi_{rescaled2}$	is the difference in ϕ between the position of the cluster in the second layer of the electromagnetic calorimeter and the extrapolated momentum- rescaled track from the perigee, multiplied by the charge.	Track-cluster matching
E/p	is the ratio of the energy of the cluster to the momentum of the track. It is used for $E_T > 150$ GeV	Track-cluster matching
eProbabilityHT	is the likelihood probability based on information (transition radiation) from the transition radiation tracker (TRT).	TRT

Table 4.4: *Type and description of variables used in electron identification [42].*

4.9 Comparison of electron ID variables for electron-in-jet and isolated electron

We need electrons from two different topologies that will give isolated electrons and electrons-in-jet. The source of our isolated electron is Z→ee events because this is a clean source of Drell Yan events with no extra jets. The electron-in-jet is the subleading electron from the boosted neutrino sample that is inside a jet with the ΔR(e,j) of 0.4. Figure 4.7 is a plot of the energy width variables used to distinguish narrow electron showers from diffuse hadronic showers. From the distributions, we can see that the electron in jet (red curve) is twisted, this is due to nearby jet activity.

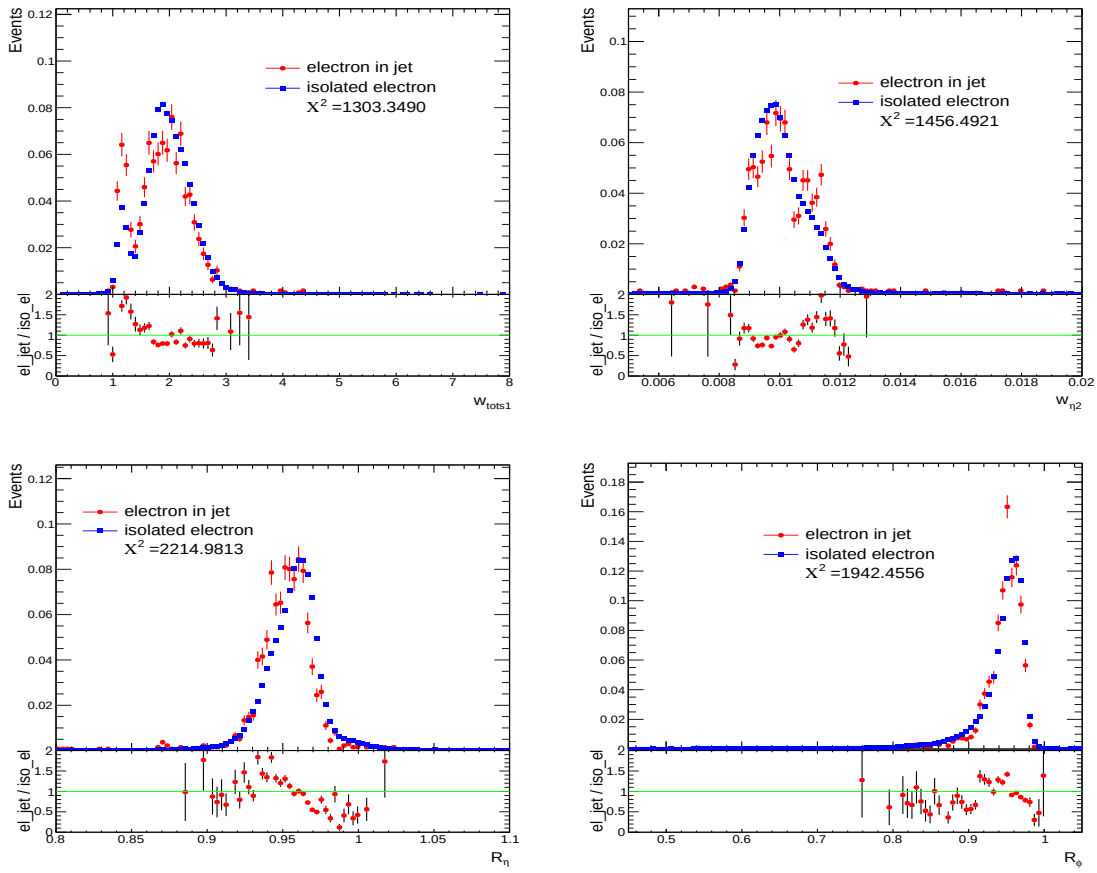


Figure 4.7: *Plots of the w_{tots1}, $w_{\eta 2}$, R_η and R_ϕ for electron in jet and isolated electron.*

The highest difference in these variables between these two electrons is seen in R_η, this is because for the electron in jet, there is an additional energy due to the nearby jet polluting the 7 ×7 window resulting in lower values for this electron. The same effect is responsible for the difference in R_ϕ. The difference in $w_{\eta 2}$ is as a result of the nearby jet broadening the width the shower of this electron closest to it. The variable with the least variation among them is w_{tots1} which peak at a higher value for electron in jet due

to the nearby jet. The second peak seen is a contribution from the endcap.

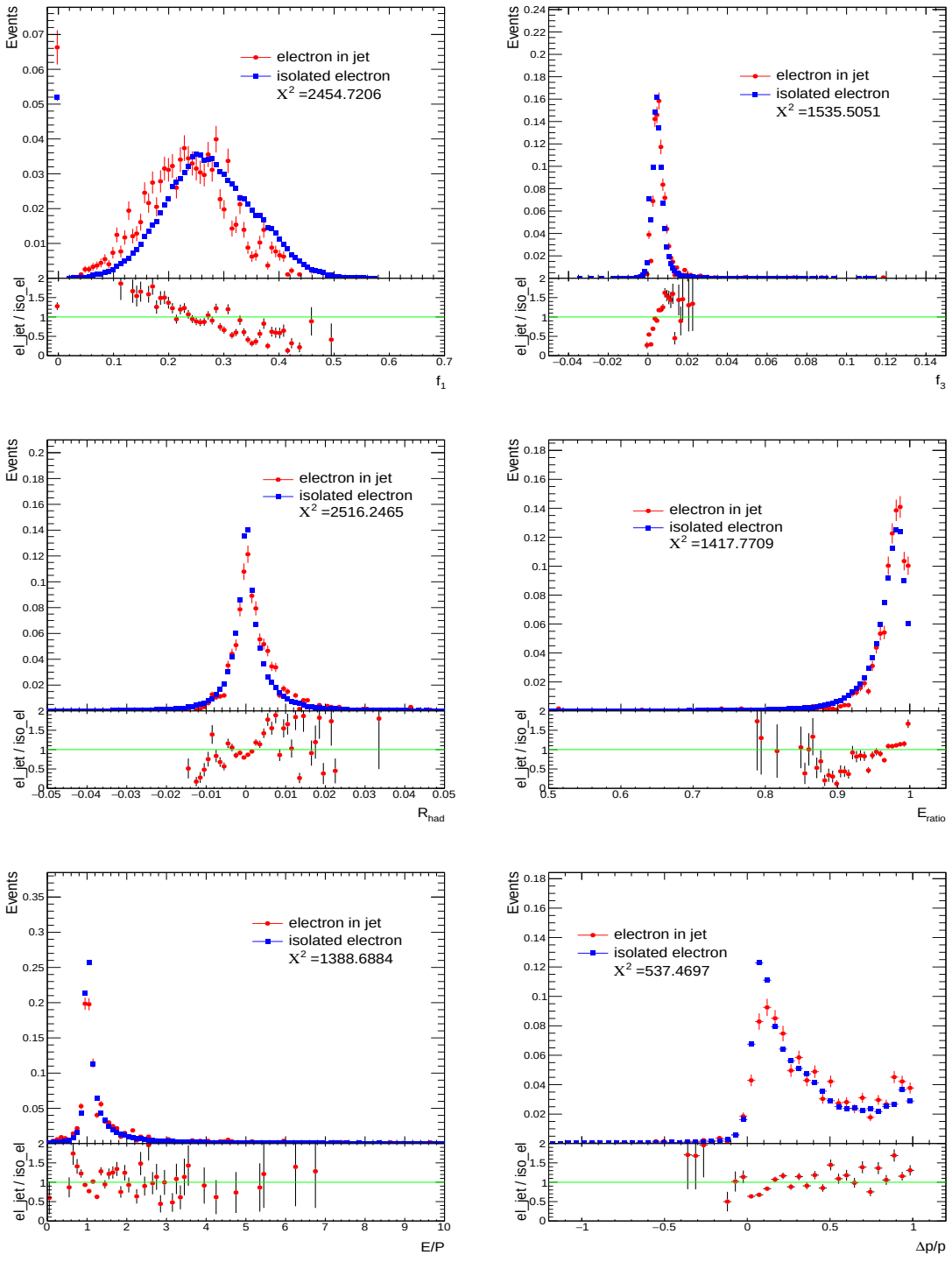


Figure 4.8: *Plots showing f_1, f_3, R_{had} and E_{ratio} for electron in jet and isolated electron.*

We can see the extent of variation of the energy ratio variables for the two types of electrons in Figure 4.8 with the highest seen in R_{had}, which indicates more hadronic leakage associated with the showers of the electron close to the jet due to contributions from the closeby jet. The next is f_1 showing lower values for the electron close to jet because an isolated electron will deposit most of its energy in the first layer of the EM calorimeter that is why we have higher values for the isolated electron, for the electron in jet we expect it to deposit most of its energy in the third layer rather than the first layer of the calorimeter. This is responsible for the observed difference in f_1 and f_3. The effect of the nearby jet is seen with E_{ratio} even though this is the variable with the least variation amount the energy ratio variables. Figure 4.9 shows the remaining

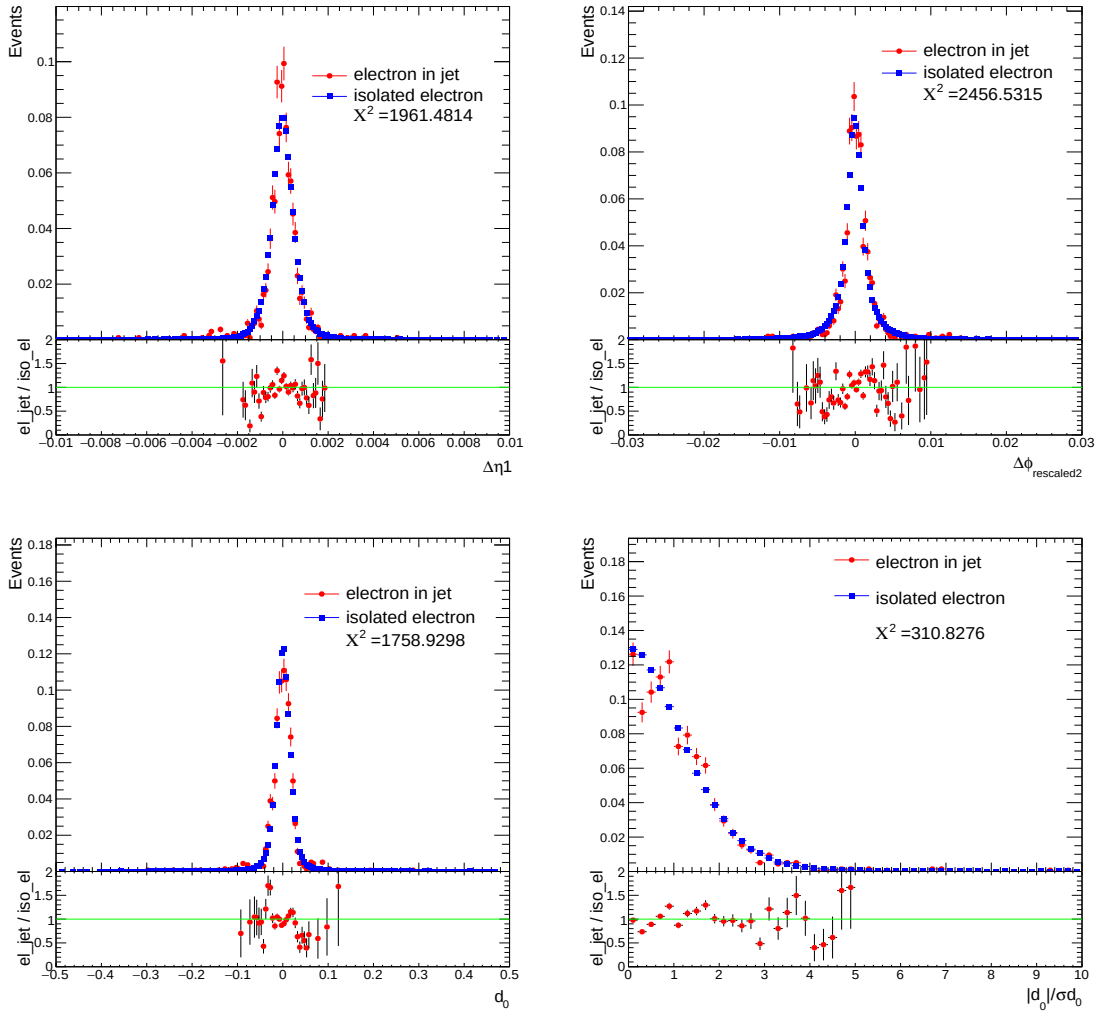


Figure 4.9: *Plots of E/p, Δp/p, Δη1, $\Delta\phi_{rescaled2}$, d_0 and $|d_0|/\sigma d_0$ for electron in jet and isolated electron.*

discriminating variables for the two electron types. The highest difference for this set of variables is $\Delta\phi_{\text{rescaled2}}$ followed by $\Delta\eta 1$, d_0, E/p, Δp/p and $|d_0|/\sigma d_0$ in that order. In

all the variables considered, the least discriminating variables are $|d_0|/\sigma d_0$ and $\Delta p/p$.

4.10 Profile plots of electron in jet ID as a function of angular distance

Profiles are used to display the average value of a variable and its uncertainty for each bin or number of bins. Since small radius jets have radius of 0.4, the profile plots will show the extent of average variation of the electron ID variables within the jet radius. Figures 4.10, 4.11 show the profile plots of the ID variables as a function of angular distance. This profile is shown for two angular distance bins, i.e from $0-0.2$ and $0.2-0.4$. For some of the variables, the value of the ID variable within angular distance of 0-0.2 is higher than that of angular distance of $0.2-0.4$ while the reverse is the case for other variables. The variable with the highest average variation within the two angular distance bins (difference in the position of the ID variables in the two bins) is E/p followed by $|d_0|/\sigma d_0$, W_{tots1}, f_1, R_η, E_{ratio}, R_{had}, R_ϕ, $\Delta p/p$, f_3, d_0, $\Delta\phi_{\text{rescaled2}}$, and $\Delta\eta 1$ in that order.

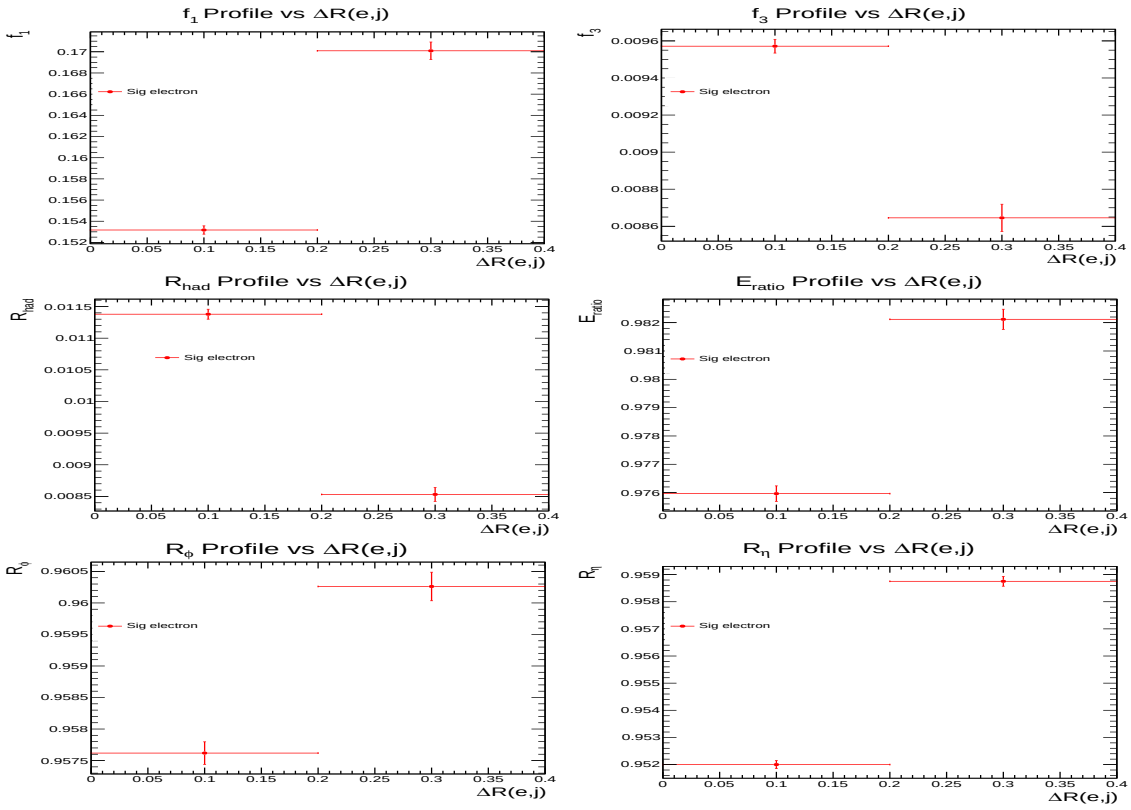


Figure 4.10: *Profile plot of f_1, f_3, R_{had}, E_{ratio}, R_ϕ, R_η as a function of ΔR for electron close to jet.*

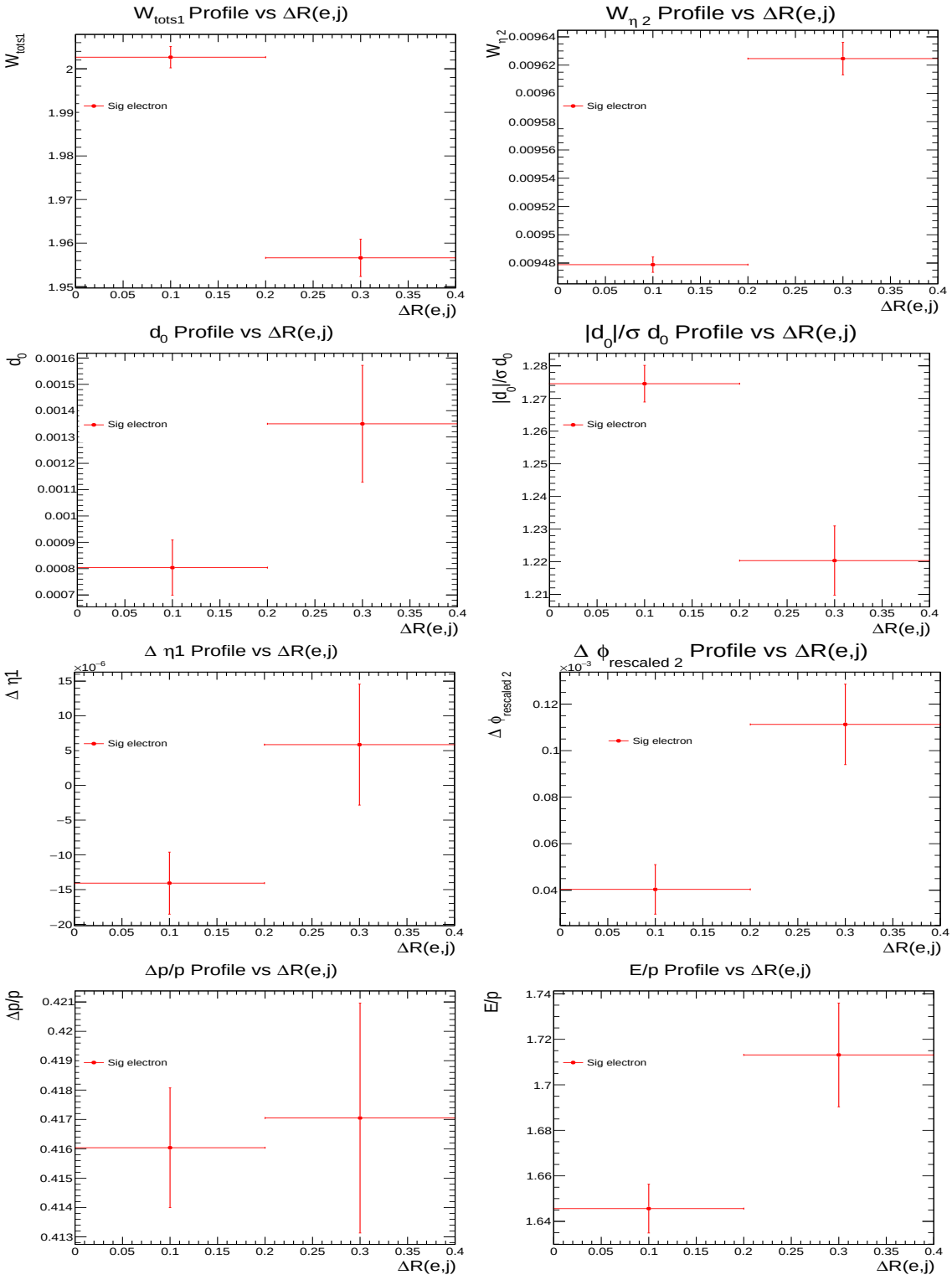


Figure 4.11: *Profile plot of w_{tots1}, $W_{\eta 2}$, d_0, $d_{0significance}$, $\Delta\eta 1$, $\Delta\phi_{rescaled2}$, $\Delta p/p$ and E/p as a function of ΔR for electron close to jet.*

4.11 Electron in jet identification variables inside a jet

In order to identify electron identification variables that are robust against nearby hadronic activity, the electron ID variables for the electron in jet were plotted as a function of angular distance to see how they vary close to the jet.

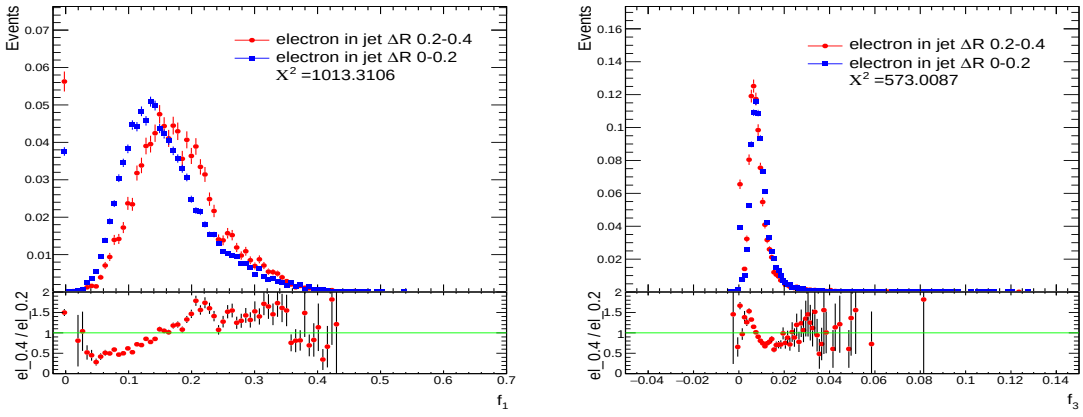


Figure 4.12: *Plot of f_1, and f_3 for an electron within distance 0 - 0.2 and 0.2 - 0.4 of a jet.*

Since ATLAS uses small radius jets of 0.4, variables with low variation within this jet radius will signify robustness against nearby jets activity and will be variables that can be used in identifying an electron within the vicinity of a jet. Figures 4.12 - 4.14 show a comparison of the electron ID variables for angular distance of $0-0.2$ and angular distance of $0.2-0.4$. The variation in these two bins is attributed to the close by jet, R_η is the variable that is affected the most by this closeby jet seen on Figure 4.14. This implies that the nearby jet deposits some of its energy in the electron energy cluster which affects the ratio of the electron's cell energies in a 3×7 window to that of a 7×7 window in the second sampling. It is closely followed by f_1 seen in Figure 4.12, where the energy fraction within angular distance of $0.2-0.4$ is higher than the energy fraction within angular distance of $0-0.2$, this implies the effect of jet activity dominates as the electron is closer to the jet since jets deposit less energy in the first layer of the EM calorimeter. The ratio of d_0 to its significance exhibit the least variation closely followed by d_0 as seen in Figure 4.13. This implies that the transverse impact parameter of the electron relative to the beam line is not significantly affected by the nearby jet. The current standard electron ID uses the following input variables for the different likelihoods: R_{had}, R_η, $\Delta\eta 1$, $w_{\eta 2}$, f_1, f_3, r_ϕ, $\Delta p/p$, $\Delta\phi_{\text{rescaled2}}$, d0, $|d_0|/\sigma(d_0)$, w_{tots1}, E/p and TRT-PID. Variables with the least variation within ΔR of 0.4 will be the robust variables that can be used in identifying an electron close to jet. The summary of variation of these variables seen from their χ^2 values is shown on Table 4.5. The variables that show the least variation in Table 4.5 are the candidates for the new electron in jet ID.

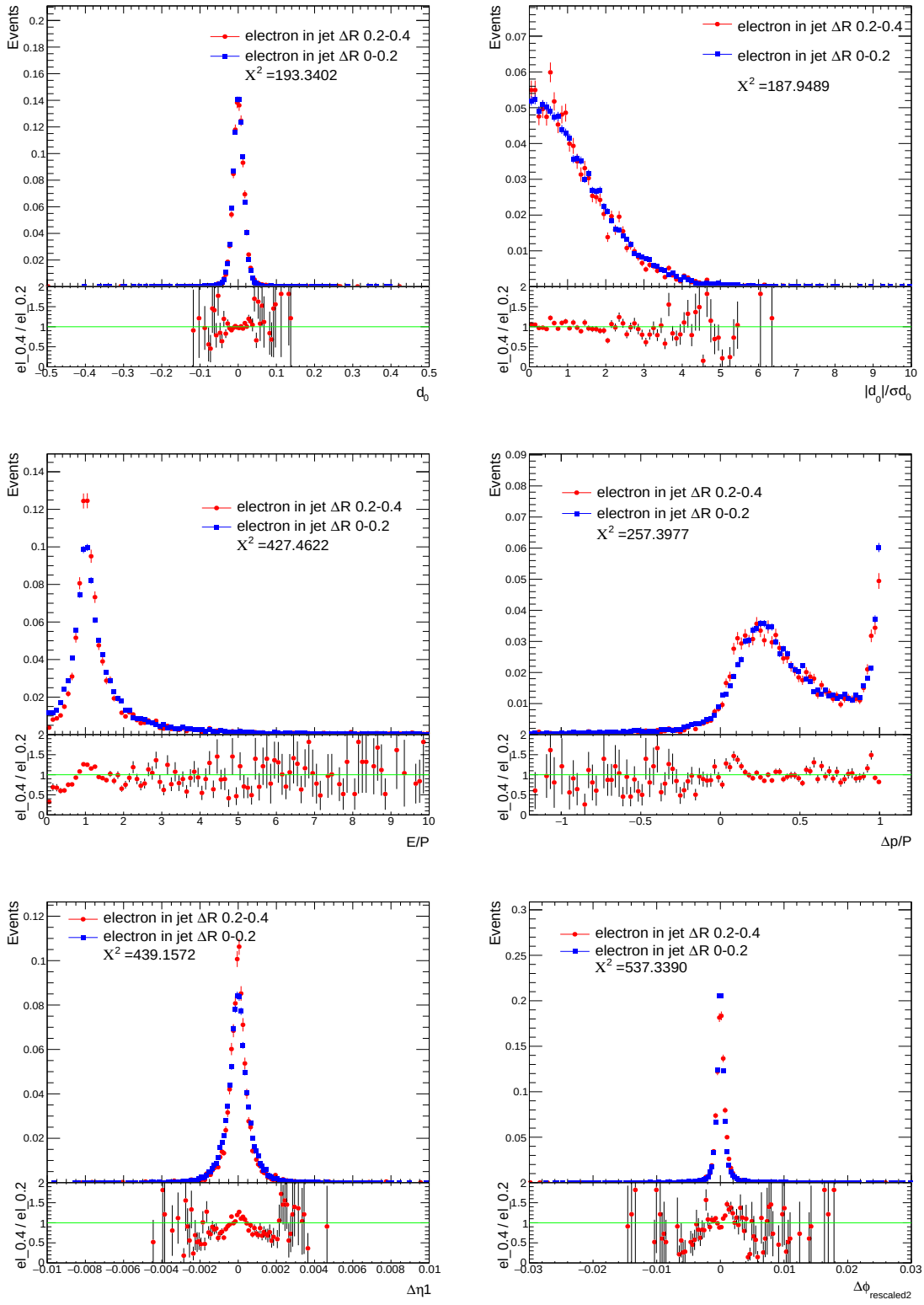


Figure 4.13: *Comparison of the track variables and the track-cluster match variables for an electron within distance 0 - 0.2 and 0.2 - 0.4 of a jet.*

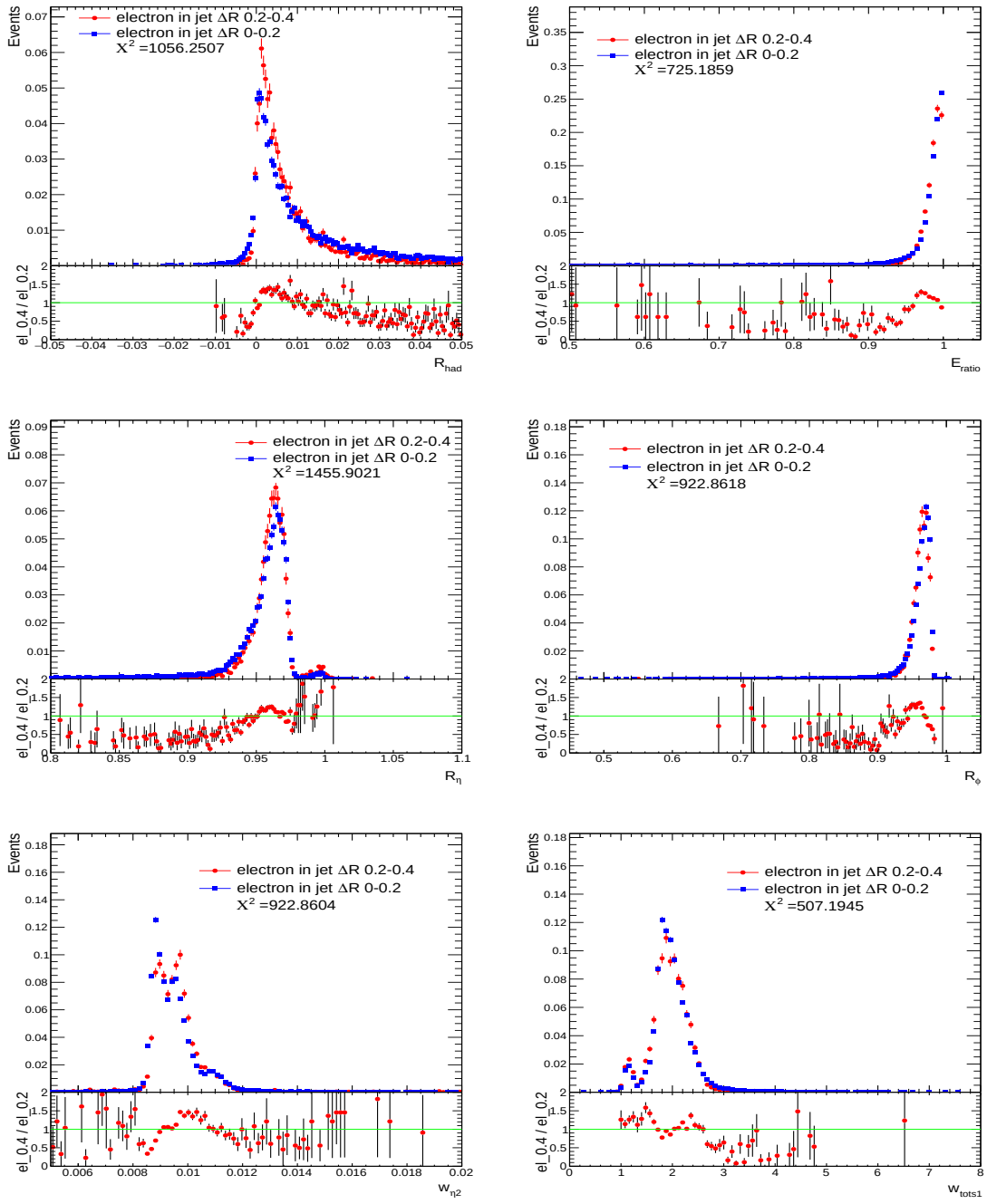


Figure 4.14: *Comparison of R_{had}, E_{ratio}, R_{η}, R_{ϕ}, $w_{\eta 2}$, and w_{tots1} for electron within distance 0 - 0.2 and 0.2 - 0.4 of a jet.*

We used our choice variables and developed a new ID for electrons in jets. We attempted to use the Z→ee process to make the ID using our choice variables on Table 4.5, this resulted into a slight improvement seen in Figure 4.15. This approach looks very promising, since we are aiming for an electron efficiency of about 70%, when we

used a boosted neutrino sample for tuning, we got an efficiency of about 70% but there was also a significant lost in background rejection. A detail study of the background rejection and how it can be improved is been done before it is implemented in ATLAS.

ID variables	χ^2	Remark
R_{had}	1056.2507	not suitable for new ID
R_{η}	1455.9021	not suitable for new ID
$\Delta\eta 1$	439.1572	suitable for new ID
$w_{\eta 2}$	922.8604	not suitable for new ID
f_1	1013.3108	not suitable for new ID
R_{ϕ}	922.8618	not suitable for new ID
f_3	573.0087	suitable for new ID
$\Delta p/p$	257.3977	suitable for new ID
$\Delta\phi_{\text{rescaled2}}$	537.3390	suitable for new ID
$\lvert d_0\rvert/_0$	187.9489	suitable for new ID
d_0	193.3402	suitable for new ID
E/p	427.4622	suitable for new ID
w_{tots1}	507.1945	suitable for new ID
E_{ratio}	725.1859	not suitable for new ID

Table 4.5: *Table showing ID variables, their χ^2, and the variables chosen for our electron in jet ID. Variables with the least χ^2 values(in green) are the best candidates for our electron in jet ID while those in red are those that are affected most by nearby jet activity and will not be included in the ID for electrons close to jet.*

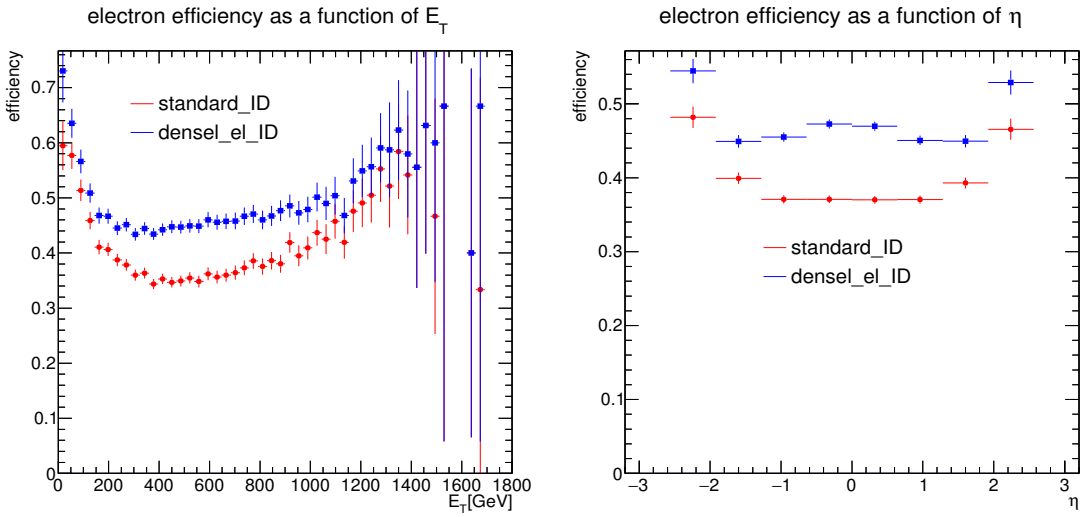


Figure 4.15: *Electron efficiency as a function of E_T and η for the medium Likelihood using the standard electron ID and the electron in jet ID.*

4.12 Control region

The control region is defined in the region of low reconstructed m_{W_R} mass which corresponds to the parameter space that has been excluded by previous searches [73]. In Figure 4.16, the data-MC agreement of the leading electron p_T and η are shown.

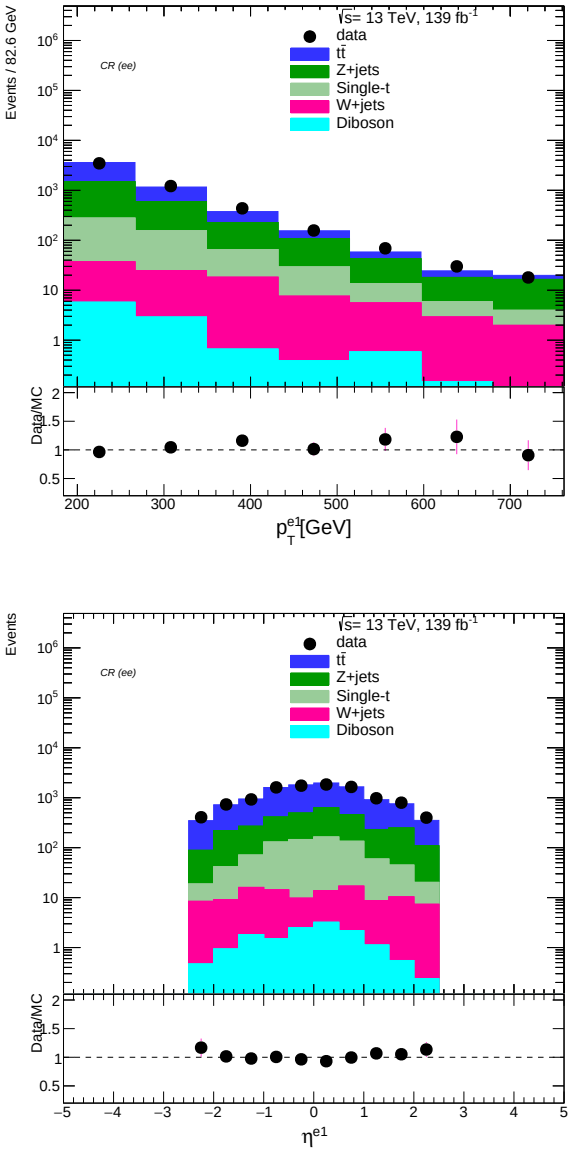


Figure 4.16: *A comparison of the leading electron kinematics in the CR from data and MC samples with only statistical uncertainties.*

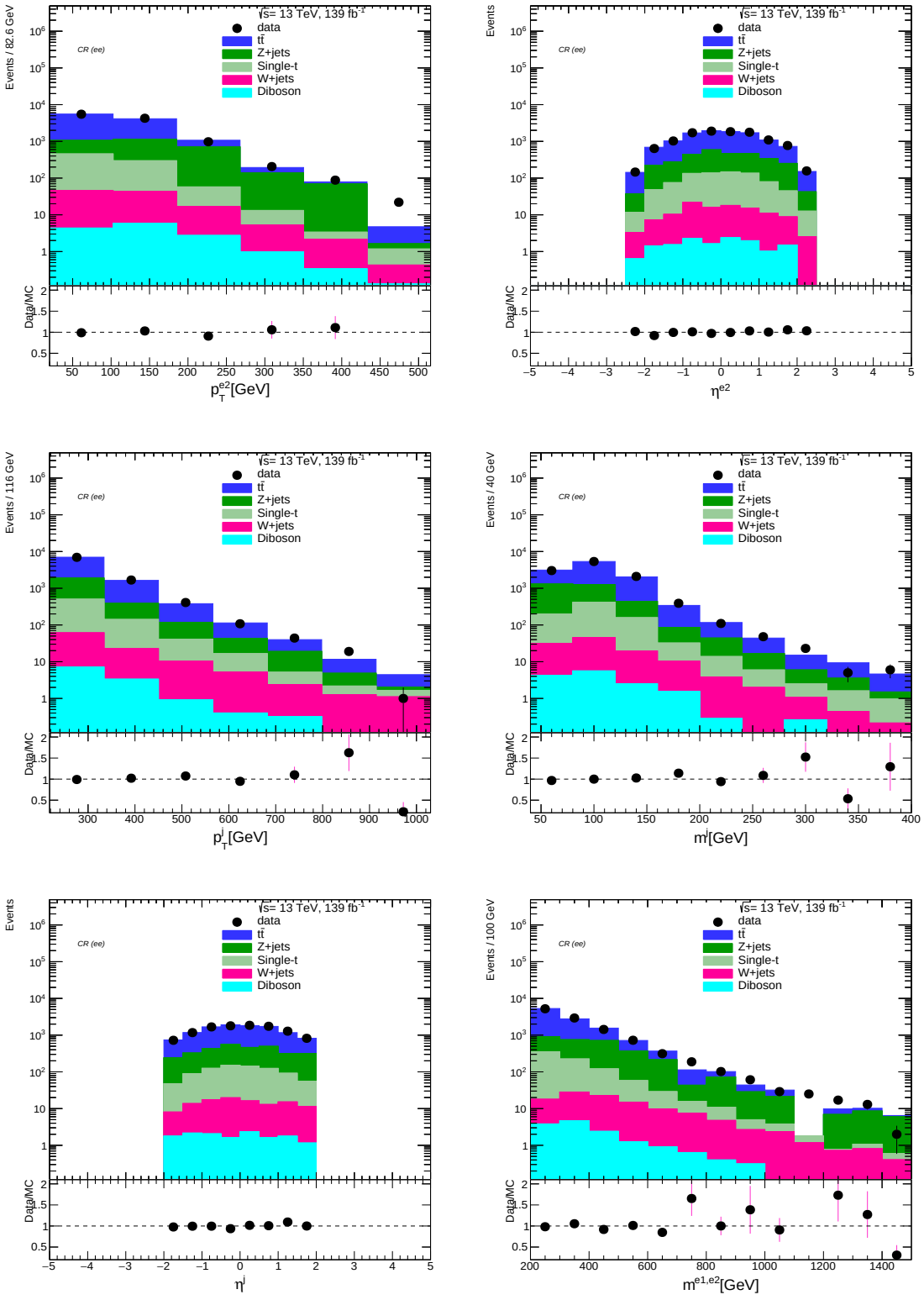


Figure 4.17: *A comparison of the sub-leading electron, large radius jet and di-electron invariant mass kinematics in the CR from data and MC samples with only statistical uncertainties.*

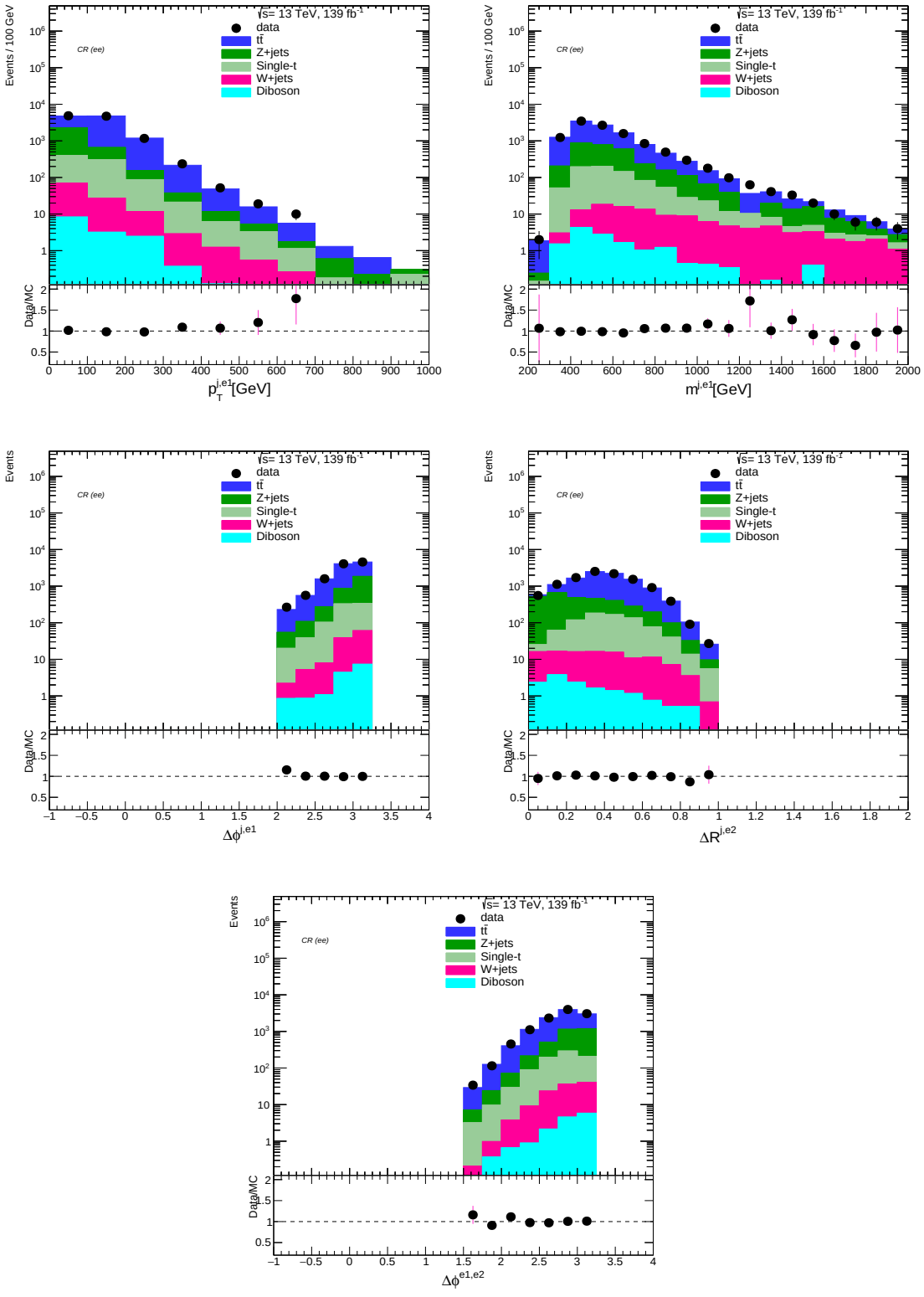


Figure 4.18: *W_R kinematics and angular distributions in the CR from data and MC samples with only statistical uncertainties.*

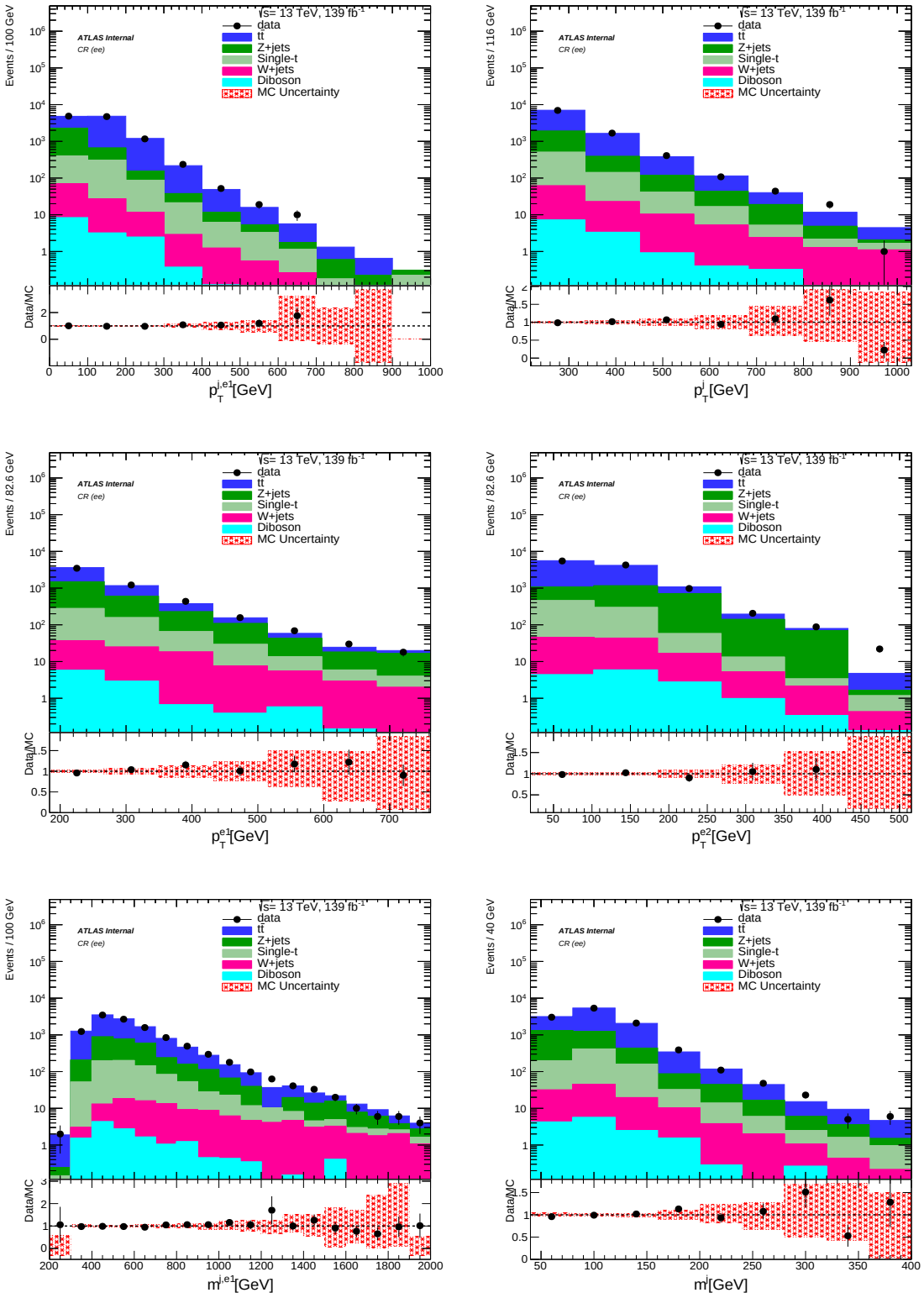


Figure 4.19: *W_R, N_R and electron kinematic distributions in the CR from data and MC samples with systematic uncertainties.*

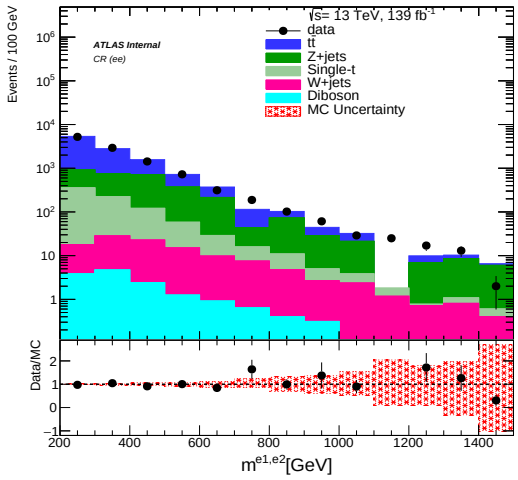


Figure 4.20: *Di-electron invariant mass distribution in the CR from data and MC samples with systematic uncertainties.*

Figure 4.17 show the data-MC agreement of the sub-leading electron p_{T}, η, large-radius jet p_{T}, mass, η, and the invariant mass of the electron pair. Figure 4.18 show the data-MC agreement of the W_R p_{T}, mass, and the angular distributions. Finally, Figures 4.19 and 4.20 show the data-MC agreement of the p_{T} of the W_R, large-radius jet, leading electron, sub-leading electron, the invariant mass of the W_R, large-radius jet, and the di-electron in that order with systematic uncertainties added. A reasonable agreement can be seen for all the distributions in this region. This data-MC agreement is a sanity check performed in this region since the background estimation adopted in this study is an extrapolated data-driven fit from the CR to the SR.

4.13 Control region summary

An excellent agreement can be seen between data and MC from the comparison of the CR yields in Table 4.6 The dominant contribution comes from $t\bar{t}$ followed by Z+jets while the least contribution is from diboson.

Process	Yield	Uncertainty
$t\bar{t}$	8002	$\pm$34
Single top	714	$\pm$10
Z+jets	2327	$\pm$140
W+jets	99	$\pm$10
Diboson	15	$\pm$4
Total MC	11157	$\pm$145
Data	11066	$\pm$105

Table 4.6: *Yields in CR from background and data with statistical uncertainties.*

4.14 Systematic uncertainty

A full details of systematic uncertainties pertaining to the background estimate and signal used in this analysis is given in this section. Systematic uncertainties as a result of the selection and propagation of objects are propagated through the analysis framework, a summary is shown in Table 4.7. Systematics are assessed in all cases from the difference in yield between the nominal and 1σ up or down variation of the parameter distributions. Systematic uncertainties can either be experimental uncertainties, which are related to the modeling of the response of the detector in the simulation, or theoretical uncertainties, which are related to the background process modeling in the MC simulation. Systematic uncertainties associated with large-radius jets and electrons are discussed in this section.

The combined 2015-2018 integrated luminosity is 2%[112]. This is derived from a method similar to that in [113], with the baseline luminosity measurement achieved with the LUCID-2 detector[114], from the luminosity scale calibration using scans from x-y beam separation. Data from $Z \rightarrow ee$ decays[101] are used to derive uncertainties in electron trigger, reconstruction, identification efficiencies, energy, and resolution. Uncertainties in large-radius jet energy scale (JES) is evaluated in events where the large-radius jet recoils against a well-defined reference object which can either be as Z + jets, multi jets, and γ + jets events[115]. Dijet balance measurements are used to evaluate the jet energy resolution and forward jets calibration. Two methods are used in measuring jet mass response, they are the Forward Folding technique and the Rtrk method. The Forward folding technique fits the W boson and the top quark mass peaks in semi-leptonic $t\bar{t}$ events so as to extract both the mass scale and resolution difference between data and simulation. The kinematic regime is within 200 GeV $< p_T <$ 1000 GeV and it is restricted to the region around the mass peaks of the top and W. This is complemented by the R_{trk} approach, which exploits the tracker so as to determine the uncertainty on jets measured by the calorimeter using the double-ratio of track-only quantities vs calorimeter-only quantities in data vs simulation. These two approaches are finally combined vs p_T in a given mass bin and interpolated between mass bins. The final combined measurement of the mass scale for the large radius jet is valid for the kinematic regime of 200 GeV $< p_T <$ 3000 GeV, mass $<$ 600 GeV, and $|\eta| < 2.0$. For the large radius jets uncertainties in this analysis, we ran category reductions for JES, full for jet energy resolution (JER), and full for jet mass scale (JMS), corresponding to 24, 16, and 12 nuisance parameters in that order. For the jet mass resolution (JMR), we used FullJMR which consists of 10 nuisance parameters. All MC simulations are reweighted in order for the distributions of the average number of interactions per bunch crossing will correspond to the data distribution. The reweighting is varied within its uncertainty so as to assess the associated systematic uncertainty. The effect of the different components of the uncertainties on the mass of the large-radius jet are shown in Figures 4.21, 4.22 and 4.23 for the dominant background. They are all within 5% of the nominal value.

Component	variation
Large-radius jet JES	up / down
Large-radius jet JER	up / down
Large-radius jet JMS	up / down
Large-radius jet JMR	up / down
Lepton energy-scale	up / down
Lepton energy-resolution	up / down
Lepton identification	up / down
L epton isolation	up / down
Lepton reconstruction	up / down
Lepton trigger	up / down
Pileup	up / down
Luminosity	overall
Theory	overall

Table 4.7: *Summary of systematic uncertainties for the background estimate and signal.*

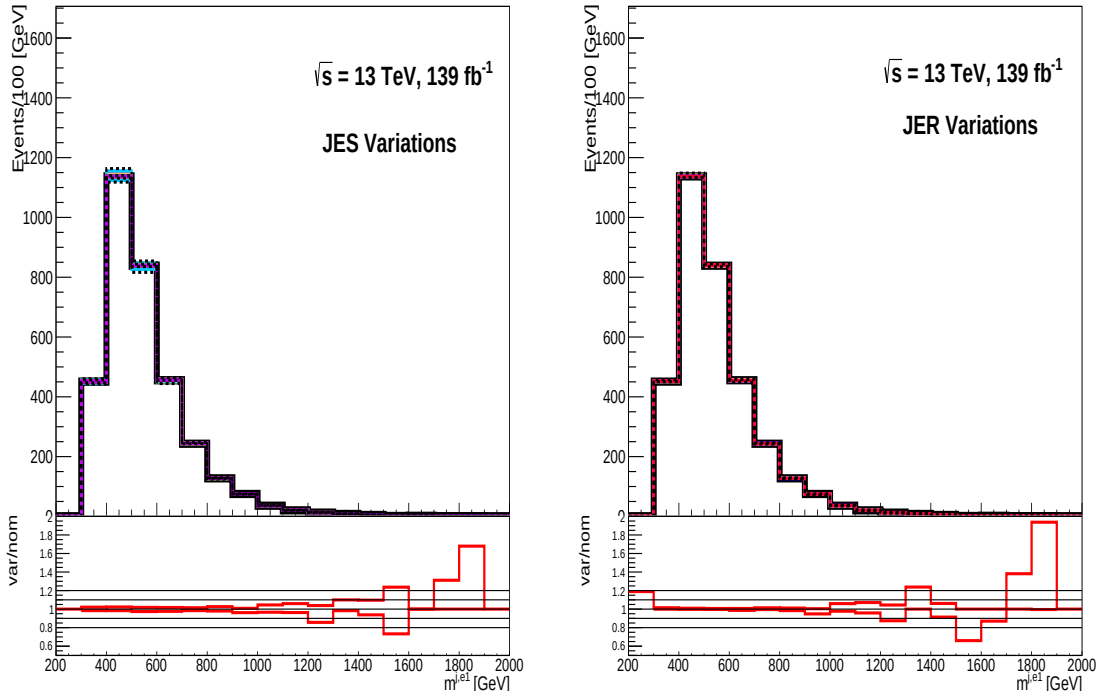


Figure 4.21: *Uncertainties due to large-radius-jet energy scale and energy resolution for the dominant background contribution.*

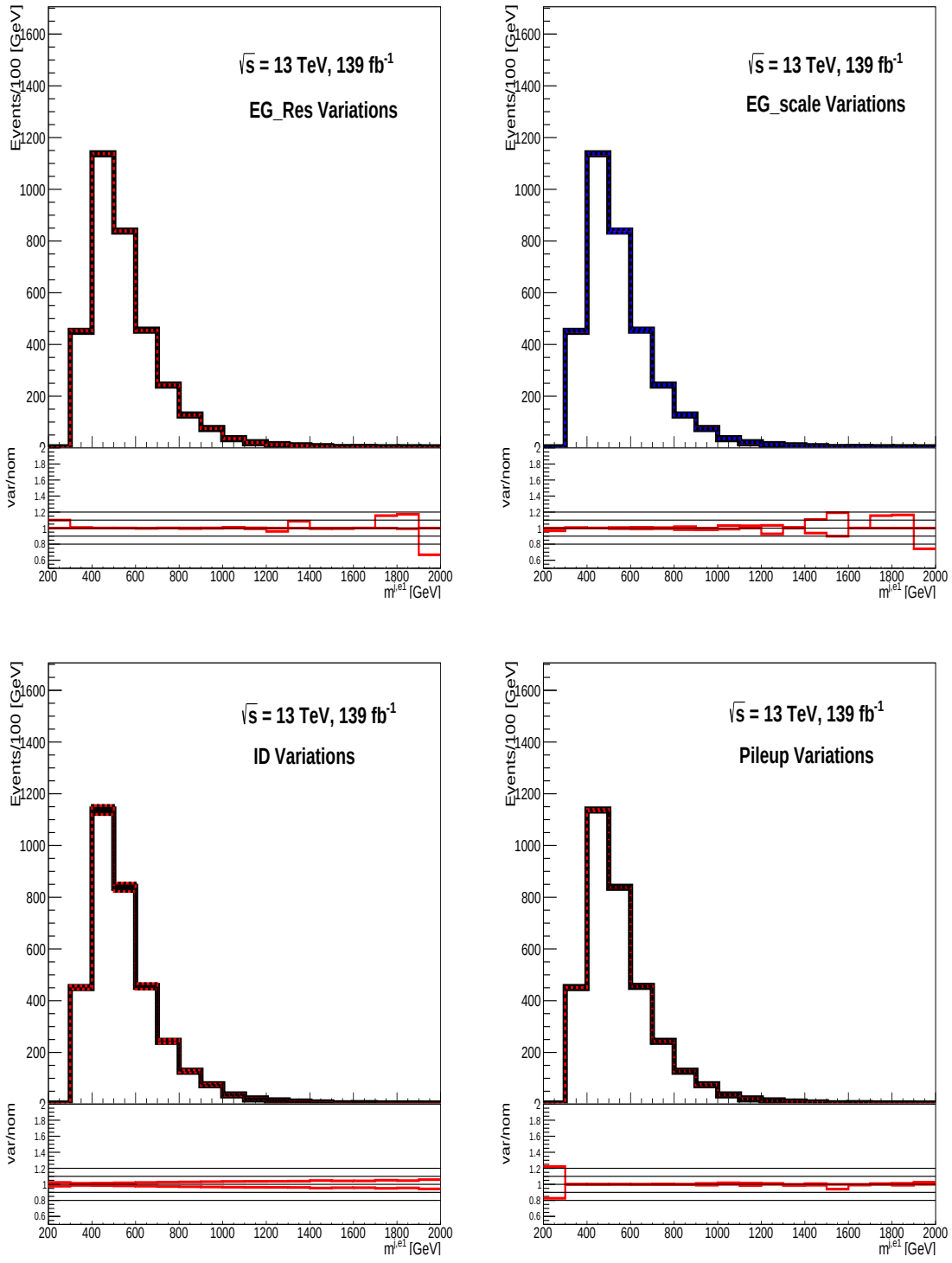


Figure 4.22: *Electron uncertainties due to energy resolution, energy scale, Identification, and pileup for the dominant background.*

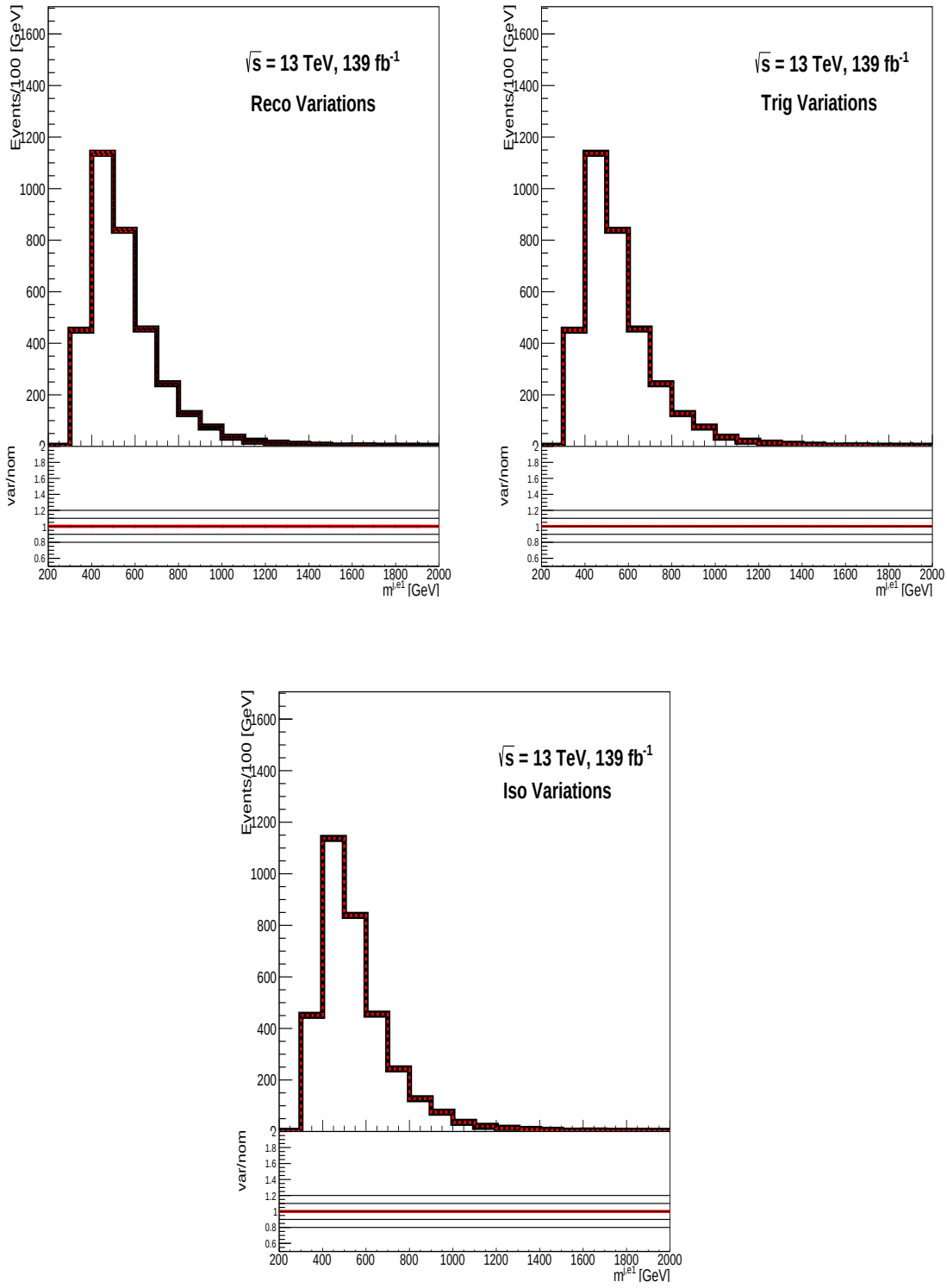


Figure 4.23: *Uncertainties due to electron reconstruction, trigger, and isolation for the dominant background.*

4.15 Background estimation in the SR

The signal region is defined in the region of high reconstructed m_{W_R} which corresponds to the parameter space that has not been excluded by previous searches. The background is estimated using a data-driven approach so as to avoid mis-modelling of the MC. The backgrounds used are $t\bar{t}$ and Z+jets. This is because $t\bar{t}$ is the dominant background and at higher masses, the proportion of Z+jets becomes larger. The fit that is obtained from this estimation in the CR is extrapolated to the SR.

The estimation uses different damped exponentially falling fit functions which are used mostly for fitting distributions that are steeply falling such as the H_T from multi-jet events or the dijet mass in previous searches [116, 117]. The following fit functions were tried in the estimation:

- A exp $(-B\mu)/\mu^C$
- A$(1-\mu)^B$ exp (Cμ)
- A$(1-\mu)^B$ $\mu^{(C\mu)}$
- A exp $(-B\mu+C\sqrt{\mu})$
- A$(1-\mu)^B$ $(1+\mu)^{(C\mu)}$
- A$(1-\mu)^B$ $(1+\mu)^{(C\log\mu)}$
- (A$/\mu$) $(1-\mu)^{(B-C\log\mu)}$
- (A$/\mu^2$) $(1-\mu)^{(B-C\log\mu)}$
- A exp $(-B\mu$ + C $\sqrt{\mu})$

Where $\mu = x/\sqrt{s}$ and A, B, and C are free fit parameters. These functions are fitted with the background MC and data distributions in the control region. The data distribution is fitted to the first function based on goodness of fit (GoF = χ^2/DoF) and also showing the best agreement in yields from in the CR from background MC. The background MC is best described by the 3rd function based on the conservative nature of the background estimate even though the GoF of this background estimate is 2.3 as seen in Figure 4.24. A W_R mass range of 600 GeV$-$ 2000 GeV was to determine the fit parameters A, B and C. A final fit on data comprising of the combination of the first and 3rd fit function is done using the W_R mass range of 600 GeV$-$ 1800 GeV based on the GoF to obtain the fit parameters A, B, and C.

The function was further fitted in different windows within the CR range, and the range of the nominal fit is chosen based on the best GoF. For background data-driven fit systematic uncertainty, the largest deviation in the SR yield obtained from the variations of the fit range when fitted to data in the CR is chosen as the uncertainty. This is also done for the fit for background MC. The statistical fluctuations of the final background fit function are accounted for by varying the input data points of pseudo experiments within statistical uncertainties. The solid black line on the bottom of Figure 4.24 is the nominal, the pink line on top is the higher uncertainty while the blue line is the

lower uncertainty. The green line is unfeasible in terms of modeling the background and it was dropped.

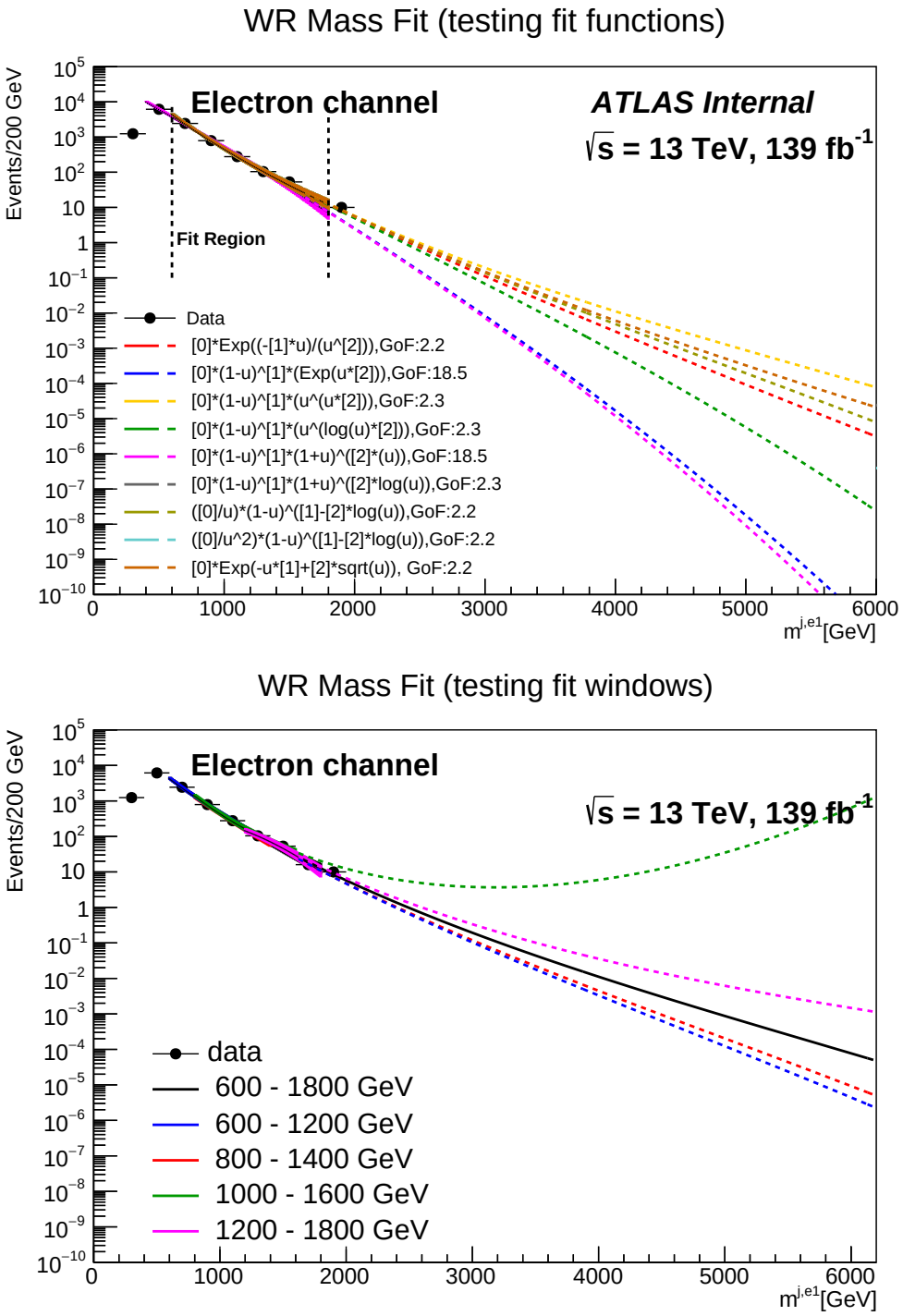


Figure 4.24: *Top is the background fit functions from CR to SR. Bottom is the nominal fit function fitted across different windows for data.*

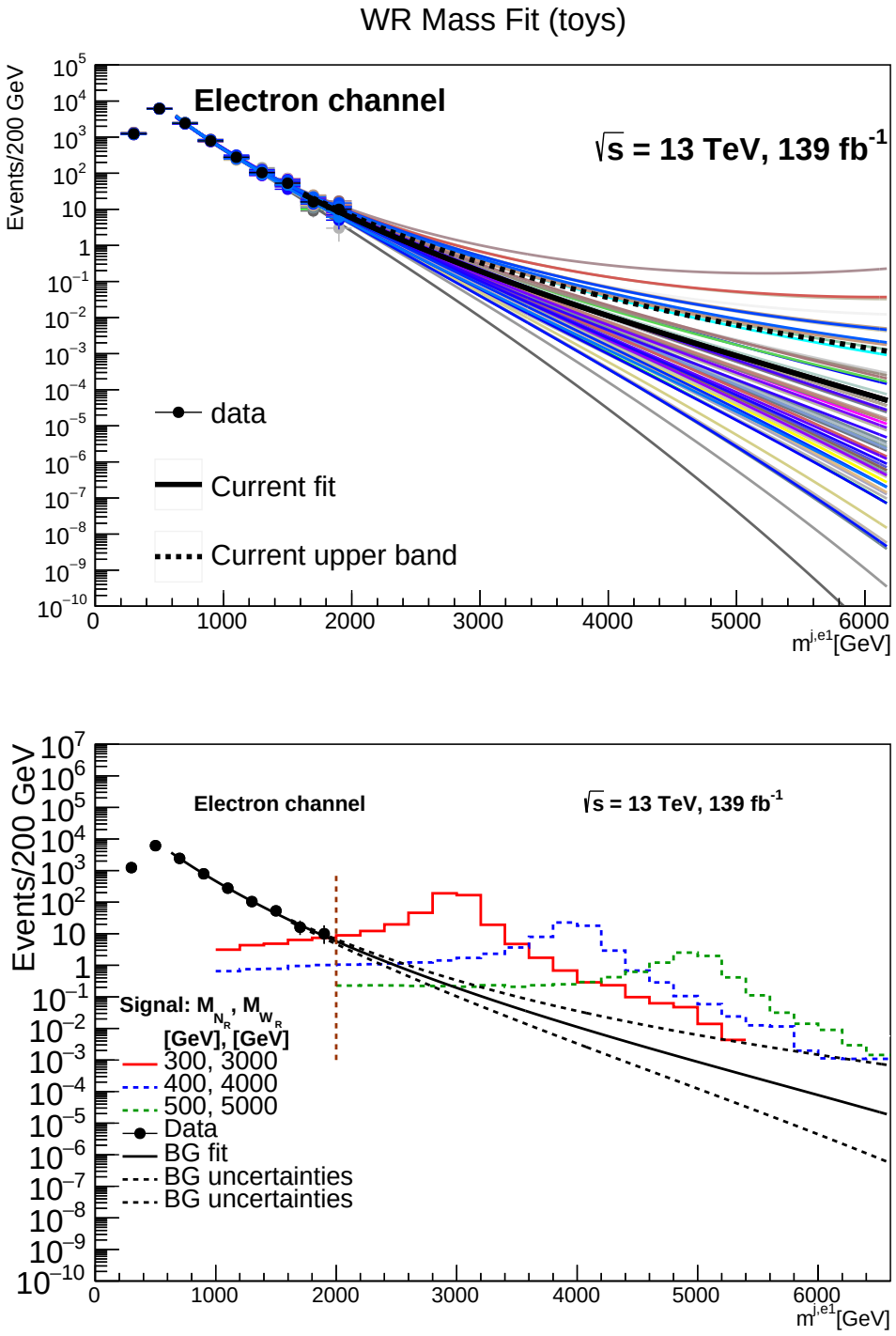


Figure 4.25: *On the top are the toys for the nominal fit while on the bottom is the background fit function in the signal region.*

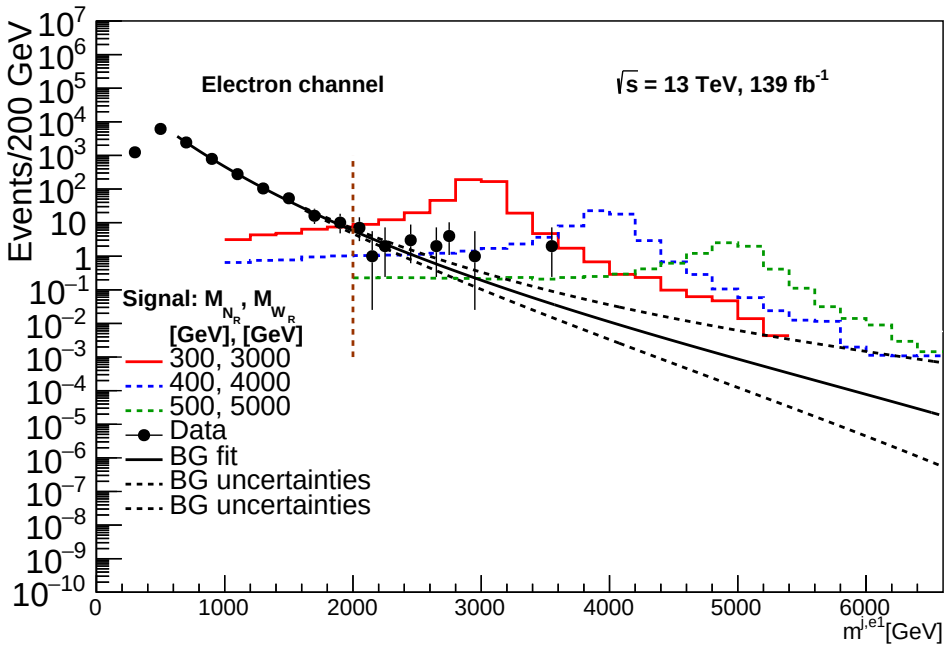


Figure 4.26: *Comparison of the reconstructed W_R mass distribution between data and the fitted background prediction. The dashed brown lines at 2000 GeV shows the boundary between the Cr and the SR. The dashed black lines are the uncertainty on the background fit. The solid black lines on the data points are the Poisson uncertainties.*

All the points in the nominal fit that we have chosen are further smeared with a Poisson distribution and refitted to get the W_R mass fit (toys) on the top of Figure 4.25. This is done to assess the statistical uncertainty on the nominal fit. Here the solid black line is our nominal fit and the black dash line is the higher uncertainty. We can see that about 90% of all the lines are under the solid black line and the dashed line is our apparent uncertainty. The final background fit function is then extrapolated to the signal region to obtain the final fit with associated uncertainty bands shown with signal sample distributions on the bottom of Figure 4.25. Figure 4.26 shows the reconstructed m_{WR} distribution in the SR. The yields in the signal region which corresponds to $m_{WR} > 2000$ GeV for the data-driven background estimate, signal points and the data are shown in Table 4.8. From the event yield in Table 4.8, we see an excess of 5.6 events in the signal region from data (22 events) compared to the 16.4 events from the background estimate. The data does not show a peak at any of the signal mass (m_{WR} mass) points in Figure 4.26.

Sample	Nominal	Up	Down
Background	16.4	19.9	12.9
m_{WR} 3000, m_{NR} 300	502		
m_{WR} 4000, m_{NR} 400	76		
m_{WR} 5000, m_{NR} 500	15		
Data	22		

Table 4.8: *Event yield in the signal region.*

4.16 Conclusion

A search was presented for a right-handed heavy boson (W_R) decaying into a boosted right-handed neutrino N_R using 139 fb^{-1} of $\sqrt{s}$ = 13 TeV proton-proton collision data from the ATLAS detector at the LHC. Only the electron final state is reported in this thesis which makes use of the large-radius jet that contains an electron as our N_R so as to significantly reduce the background contribution. The W_R reconstructed is consistent with background prediction. The partial Run 2 result exclude W_R mass above 4.8 TeV for N_R mass 0.4-0.5 TeV. The full Run 2 result show a significance of 1.4 σ which is lower than the 2.4 σ obtained using the partial Run 2 data [80]. We do not see any significant deviation to the prediction of the Standard Model.

5. Search for single leptoquarks in final states with electrons and muons

5.1 Introduction

Lepton Flavour Universality (LFU) is one of the fundamental predictions of the SM. The Z-boson and the photon couples independently with the same strength to all the three generations of leptons. This was tested at LEP [118] and ATLAS [119]. New physics beyond the Standard Model may be implied to exist if there is any deviation from the LFU prediction. Recently, in the flavor sector, a variety of models are trying to explain the several anomalies observed in various rare B decays and the recent moun g-2 measurement [120–127].

The realm of leptoquarks (LQ) offers one possible explanation. Several theories of beyond the Standard Model physics such as Grand Unified Theories [128], or Pati-Salam models [62, 129, 130] predict the existence of LQs. These are colour charged particles that couples to one lepton and one quark. LQs carry a fractional electric charge and can either be spin-0 (scalar) or spin-1 (vector). Recently, LQs attracted significant attention as they might be linked to observed flavor anomalies in various rare B decays [131–134].

The production and decay of LQs at proton-proton colliders is characterized by the LQ mass m_{LQ}, the Yukawa coupling λ at the LQ-lepton-quark vertex and the decay branching fraction into a certain quark and a lepton, β. LQs at hadron colliders could be produced in pairs via quark anti-quark annihilation and gluon fusion, and singly via quark-gluon fusion. The LO contributions for the single LQ production are summarized in Figure 5.1. Single production of LQs depends on the Yukawa coupling while pair production does not. The production cross-section depends on the mass and the couplings. The cross-sections for pair production are larger at lower masses, while at higher mass and sufficiently high couplings, single production dominates. It has been shown in [135] that the cross-section is independent on the lepton flavor and only dependent on the quark flavour.

Previous searches for LQs have been carried out with the most recently performed by the CMS collaboration, which provides the most stringent limits using proton-proton collision data at a center-of-mass energy of $\sqrt{s}$ = 8 TeV corresponding to an integrated luminosity of 19.5 fb^{-1} [136]. LQ masses (at λ = 1.0) below 1730 (530) GeV in the electron (muon) channel have been excluded in this search. In this study, the search for LQs in single production decaying into one charged lepton and one jet is presented, using proton-proton collision produced by the LHC at a center-of-mass energy is $\sqrt{s}$ = 13 TeV. Selections requiring the absence or presence of b-tagged jets are applied.

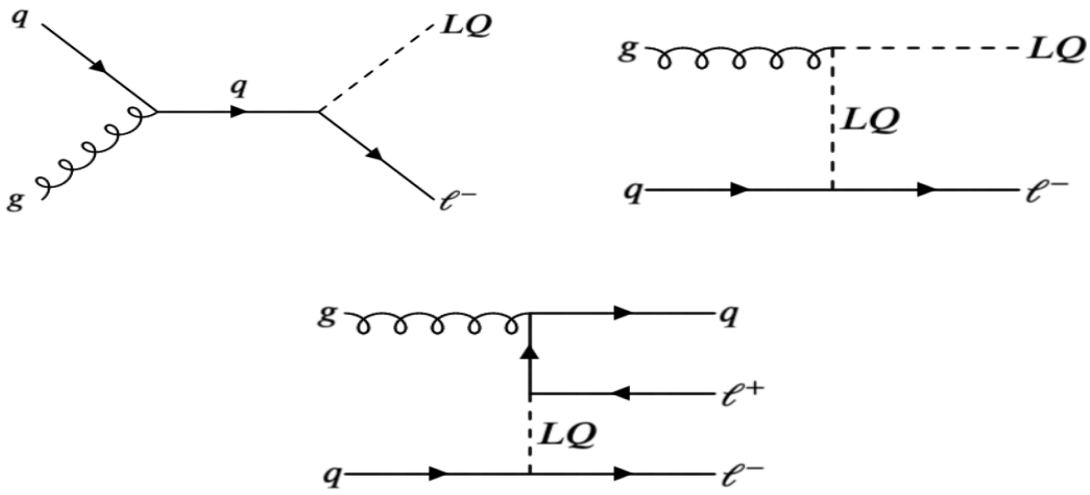


Figure 5.1: *Feynman diagrams for single LQ production. On the top row is the resonant production while the bottom is the LO non-resonant contribution.*

5.2 Data

This analysis used pp collision data with 25 ns bunch crossing collected between 2015 to 2018 at $\sqrt{s}$ = 13 TeV corresponding to 139 fb^{-1} total integrated luminosity. Events considered are those taken during stable beam conditions and in which all the relevant detector components were operational. Events are required to have a primary vertex plus, at least two tracks having a minimum p_T of 400 MeV. In situations where there are several vertices, the highest $\sum_{tracks} p_T^2$ track is chosen as the hard-scatter vertex [137]. Events are rejected if they satisfy the criteria [138] designed to reject beam-induced background and backgrounds from calorimeter noise and cosmic rays showers. Electrons and muons pass through single-lepton triggers with different p_T thresholds. The threshold for electron energy is either 60 GeV or 140 GeV depending on the identification requirement, while it is 50 GeV for muons. There is no isolation requirement applied for either of the triggers.

5.3 Signal and background samples

The event yields for signal and backgrounds are estimated using MC. Geant4 [98] was used to simulate the ATLAS detector response and the reconstruction of all MC events were done the same way as data [97] with the exception of signal samples that are reconstructed using fast simulation [97].

5.3.1 Signal MC

To simulate the LQ production, MADGRAPH 5 [81] was used with the "ToolBox" UFO model [135], that implements the Lagrangian described in [139], using the PDF set NNPDF3.0NLO [83]. Madgraph was interfaced to PYTHIA 8 [140] with the A14 set of

tuned parameters. Four different signal samples have been arrived at from the independent treatment of the couplings to electrons/muons and strange/bottom quarks which models the sensitivity of light-/b-jets. A scalar representation which corresponds to $\tilde{S}_1$ in [139] is studied for the LQ. The m_{LQ} range of samples from 500 to 3500 GeV with a benchmark coupling of $\lambda = 1.0$ was generated.

5.3.2 Background Processes

The background processes considered for this study include Z + jets, W + jets, $t\bar{t}$ (+V), single top, and diboson. Details of the generators used to model them is given in Table 5.1. For this analysis, events containing Z and W bosons with associated jets are simulated with Sherpa 2.2.1 [95] generator using the NNPDF3.0 [83] next-to-next-to-leading order PDFs (parton distribution functions set), normalized to NNLO cross-section in QCD calculated using FEWZ [141, 142] and the MSTW 2008 [143–145] NNLO PDF set. The generation is split into bins of (truth-level) max(HT,pVT)so as to ensure sufficient statistics in all the phase space explored in the analysis. The filters: c veto + b veto, c filter + b veto, and b filter were also used to filter the quark flavors.

Modelling the production of $t\bar{t}$ events is done using the POWHEGBOX [91–94] v2 generator at NLO with the NNPDF3.0NLO [83] PDF set setting the h_{damp} parameter to 1.5 m_{top} [86]. The A14 tune [84] and the PDF set NNPDF23LO was used to interface events with PYTHIA8.230 [82].

The production of Single-top tW associated production is modeled using the POWHEGBOX [91, 93, 94, 146] v2 generator at NLO in QCD in the five flavor scheme with the PDF set NNPDF3.0NLO [83]. In order to handle the interference with $t\bar{t}$ production [86], The diagram removal scheme [147] was employed. The A14 tune [84] and the PDF set NNPDF23LO was used to interface events with PYTHIA8.230 [82].

The production of single-top t-channel (s-channel) is modeled using the POWHEGBOX [91, 93, 94, 148] v2 at NLO in QCD in the four (five) flavour scheme with the NNPDF3.0NLO [83] PDF set. The A14 tune [84] and the PDF set NNPDF23LO was used to interface events with PYTHIA8.230 [82].

Modelling of the production of $t\bar{t}$+V events is done using the MADGRAPH5_AMC@NLO v2.3.3 [81] generator at NLO with the PDF set NNPDF3.0NLO [83]. The A14 tune [84] and the PDF set NNPDF23LO was used to interface events with PYTHIA8.230 [82].

Diboson processes containing 4 charged leptons, 3 charged leptons + 1 neutrino or 2 charged leptons + 2 neutrinos are simulated with the SHERPA 2.2.2 generator [95]. All the diagrams with four electroweak vertices are contained in the matrix elements. They are calculated for up to 1 (4ℓ, $2\ell + 2\nu$) or 0 partons ($3\ell + 1\ \nu$) at NLO and up to 3 partons at LO using the Comix [149] and OpenLoops [150] matrix element generators merged with the Sherpa parton shower using the ME+PS@NLO prescription [151]. The cross-section of the diboson samples have been scaled down so as to account for its use of α_{QED}=1/129 instead of the corresponding 1/132 which uses the current PDG parameters as the G_μ scheme input.

Process	Matrix element	Non-perturbative	Refs
$Z/W/\gamma^*$	SHERPA 2.2.1, NNPDF3.0	SHERPA 2.2.1	[95]
Top ($t\bar{t}$ + single-top)	POWHEG-BOX 2	PYTHIA 8	[91, 93, 94, 140, 146, 148]
$t\bar{t}$ + V	MADGRAPH5_aMC@NLO	PYTHIA 8	[140, 152]
Diboson	SHERPA 2.2.2, NNPDF 3.0	SHERPA 2.2.1	[95]

Table 5.1: *Overview of the event generators and other software packages used to simulate the background samples.*

5.4 Object reconstruction and selection

In this analysis, reconstructed jets, electrons, and muons are used. Electrons are reconstructed by matching the energy clusters in the electromagnetic calorimeter with tracks from the ID, detailed procedure in section 3.2. The "tight likelihood" identification criteria [102] must be fulfilled by these electrons and their energy scale is calibrated [101, 153]. The electrons are required to have at least 30 GeV minimum transverse energy and to be within $|\eta_{\text{cluster}}| < 2.47$ excluding the EM calorimeter crack region. They are required to satisfy the track conditions in section 5.5.1 and also required to satisfy an isolation criteria applied using the calorimeter and the track-based information in order to obtain 90% efficiency for electrons with 25 GeV p_T, which goes rises to 99% for p_T = 60 GeV in case of $Z \to \ell\ell$ events.

In reconstructing muons [154], tracks in the MS and the ID are used. The p_T muons is calibrated [154], and they are required to fulfill the "high" p_T identification criteria [154]. A 30 GeV minimum p_T is required and also, they must be within $|\eta| < 2.5$. The muons tracks are required to have an impact parameter significance of less than 3 and a longitudinal impact parameter of < 0.5 mm to ensure that the track point to the primary vertex. The smallest between ΔR = 10 GeV $/p_T$ and ΔR = 0.3 gives the track isolation cone radius for muons.

Topological clusters of the calorimeter cells [50] and the particle flow algorithm [52] with radius parameter of R = 0.4 are used to reconstruct jets. Jets are required to be within $|\eta| < 2.5$ and are calibrated to the JES at particle level [103]. The minimum p_T requirements of jets is 30 GeV. For jets with p_T < 60 GeV within $|\eta| < 2.4$, the jet vertex tagger [155] is used to suppress pileup contributions. b-tagging using the DL1 algorithm [156] is performed on jets within $|\eta| < 2.5$ where several basic b-tagging algorithms [156, 157] are combined in a boosted decision tree (BDT). A b-tagging efficiency of 77% for b-jets and a rejection factor of ≈6 for c-jets and 110 for other light jets is achieved with the DL1 algorithm based on simulated $t\bar{t}$ events. A sequential overlap-removal procedure is applied for electrons, muons and jets depending on their proximity in η-ϕ space so as to avoid double counting of objects. In the first step, any electron sharing a track with a muon is removed. In the second step, any jet with ΔR < 0.2 to an electron is removed,, while in the third step, any electron with ΔR < 0.4 of a jet is removed. Finally, any jet with $\Delta R < 0.04 + 10\ \text{GeV}/p_T(\mu)$ to a muon is removed if there exist at most two associate tracks with $p_{\text{track}} > 0.5$ GeV, else the muon is removed.

5.5 Event selection

Targeting the high mass LQ signature decaying into one light lepton and one jet, events must satisfy the trigger and object criteria defined in sections 5.2 and 5.4 respectively. Two same-flavor leptons with opposite electric charge are required to be present. Both leptons are required to be isolated and at least one has to geometrically match the object that fired the trigger. In order to ensure that the efficiency of the trigger is at the plateau, the threshold p_{T} on the leading lepton is raised to 65 GeV in both the muon and the electron channel.

After applying the preselection, several orthogonal signal regions (SR) are defined. For this search, at least one jet with $p_{\mathrm{T}} > 30$ GeV is required. Each channel is split into two orthogonal regions depending on the flavor tagging decision on the leading jet so as to increase the sensitivity to different LQ couplings. In the b-veto category, b-tagged jets are rejected while the leading jet is required to be b-tagged in the b-tag category. In the signal regions events with more than one b-tagged jet are discarded. The invariant di-lepton mass is required to be at least 400 GeV so as to reduce contributions from Z+jets backgrounds. In the lower di-lepton invariant mass range (ZCR), events with di-lepton invariant mass outside this range are vetoed so as to test the modelling of the Z+jets and top backgrounds. In the intermediate di-lepton invariant mass range which is the validation region (VR), events with di-lepton invariant mass outside this range are vetoed in order to test the modelling after constraining the nuisance parameters in the background only fit. However, the di-lepton invariant mass in the top control region is lower compared to the other regions so as to have enough statistics in this region. In order to reduce top initiated backgrounds, events for which the scalar sum of the transverse momenta of all leptons and jets, H_{T}, is below 350 GeV are discarded. In order to increase the sensitivity to different LQ couplings, each channel is splitted into two orthogonal regions depending on the flavour tagging of the leading jet while the events with less or greater than two b-tagged jets are vetoed in the top control region. A lower bound on the invariant mass of the highest-p_{T} lepton and jet (m_{LQ}^{max}) is applied finally. The actual cut value is optimized for each LQ mass hypothesis based on the expected 95% confidence level (CL) upper limit on the production cross-section. A summary of the event selection for this analysis is shown in Table 5.2 with a schematic description in Figure 5.2.

SR	**Z CR**	**VR**	**$\mathrm{t\bar{t}}$ CR**
Preselection			
$p_{\mathrm{T}}^{lead.lep} > 65$ GeV, $p_{\mathrm{T}}^{jets} > 30$ GeV, $\mathrm{N}_{jet} > 0$			
$m_{\mathrm{ll}} > 400$ GeV	130 GeV $< m_{\mathrm{ll}} <$ 250 GeV	250 GeV $< m_{\mathrm{ll}} <$ 400 GeV	$m_{\mathrm{ll}} > 130$ GeV
$H_{\mathrm{T}} > 350$ GeV			
0,1 b-tagged jet			2 b-tagged jets
$m_{\mathrm{LQ}}^{max} > 300$ GeV			

Table 5.2: *A summary of event selection for the four signal regions.*

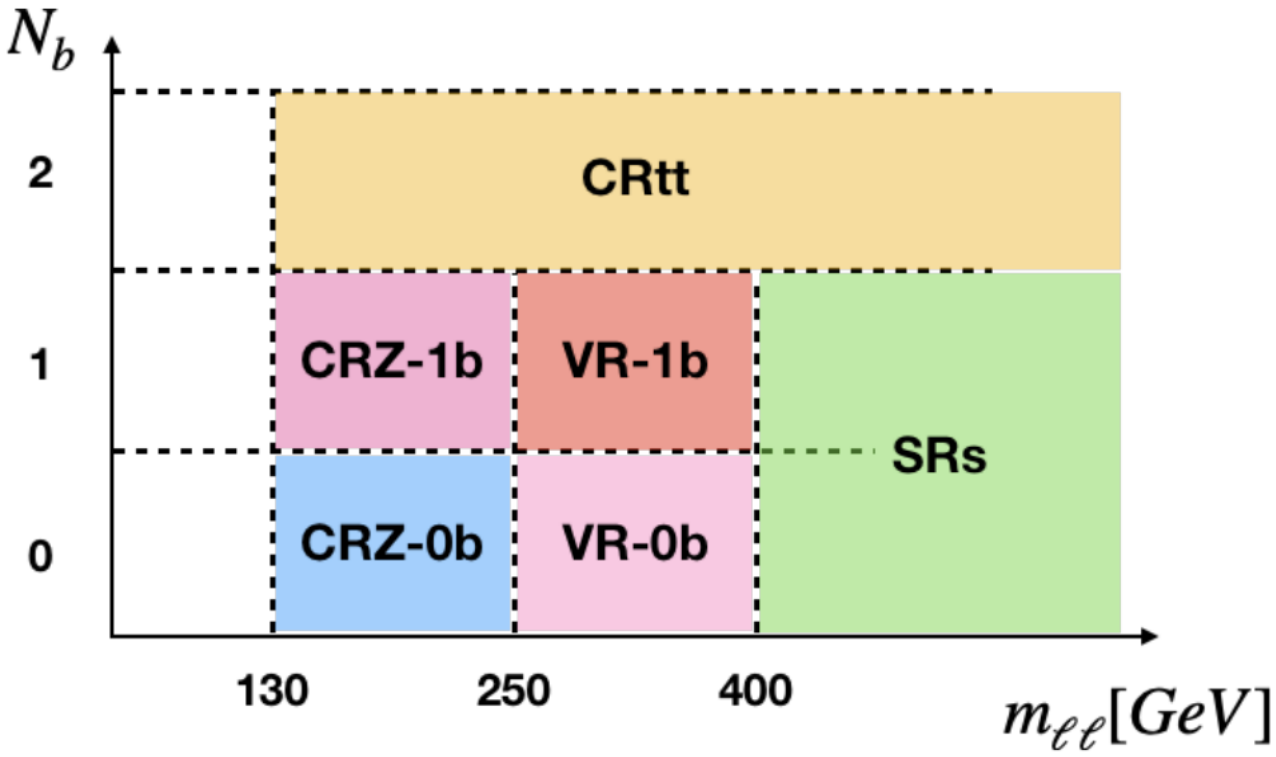


Figure 5.2: *A schematic representation of the event selection of the analysis.*

5.6 Background estimation

Backgrounds from Z + jets and $t\bar{t}$ processes are the main reducible backgrounds. Since each of these backgrounds are from MC simulation, it is important to validate the modelling in data. This is seen in subsection 5.6.1 and 5.6.2. In addition, the electron channel has a non-negligible contribution due to fake electrons that are estimated from data-driven approach using the matrix method. This estimate results in low statistics in the high m_{LQ}^{max} tail. To address this problem, an extrapolation is performed using multiple fits with two different functions having three free parameters, while the start and endpoint of the range of the fit in the mass spectrum is varied. The quantity Q which describes the agreement between the MC prediction in the tail and the different fits is determined. The central value is the fit with the lowest Q, while all other fits with smaller values of Q than the fixed value are used to estimate the uncertainty. A summary of the Q cut values and the range in m_{LQ}^{max} are shown in Table 5.5

The quantity Q is defined as

$$Q = \frac{1}{NOB} \sum_{b>b_0}^{N_b^{est}>0} \frac{(N_b^{est} - N_b^{fit})^2}{\sigma_b^2} \tag{5.6.1}$$

Where NOB is the number of bins, b_0 is a manually set threshold, N_b^{est} and N_b^{fit} are the number of emtries in the MC prediction and the fit while σ_b is the uncertainty in a certain bin b.

5.6.1 Z control region

The modelling of the Z + jets MC samples is tested in the control regions defined in section 5.5 summarized in Table 5.2. The sensitive variable in the analysis, m_{LQ}^{max}. The pre-fit and post-fit plots are presented for the electron and muon channel Z + jets control regions on Figures 5.3 and 5.4 respectively. A good data-MC agreement is seen in this region from the plots and also from the post-fit event yield in Table 5.3.

	ee b-veto	ee b-tag	$\mu\mu$ b-veto	$\mu\mu$ b-tag
Z + jets	20345 ± 667	1226±306	20917±710	1131±239
$t\bar{t}$	3418±344	4113 ±219	3099±328	3883±222
Others	1434±92	34±4	1295±83	30±3
Fakes	1655 ±40	145±12		
Total	26852±590	5519 ±138	25311±862	5044±102
Data	26852	5519	25311	5044

Table 5.3: *Post-fit event yield in all channels in the ZCR. The uncertainties are both systematic and statistical uncertainties.*

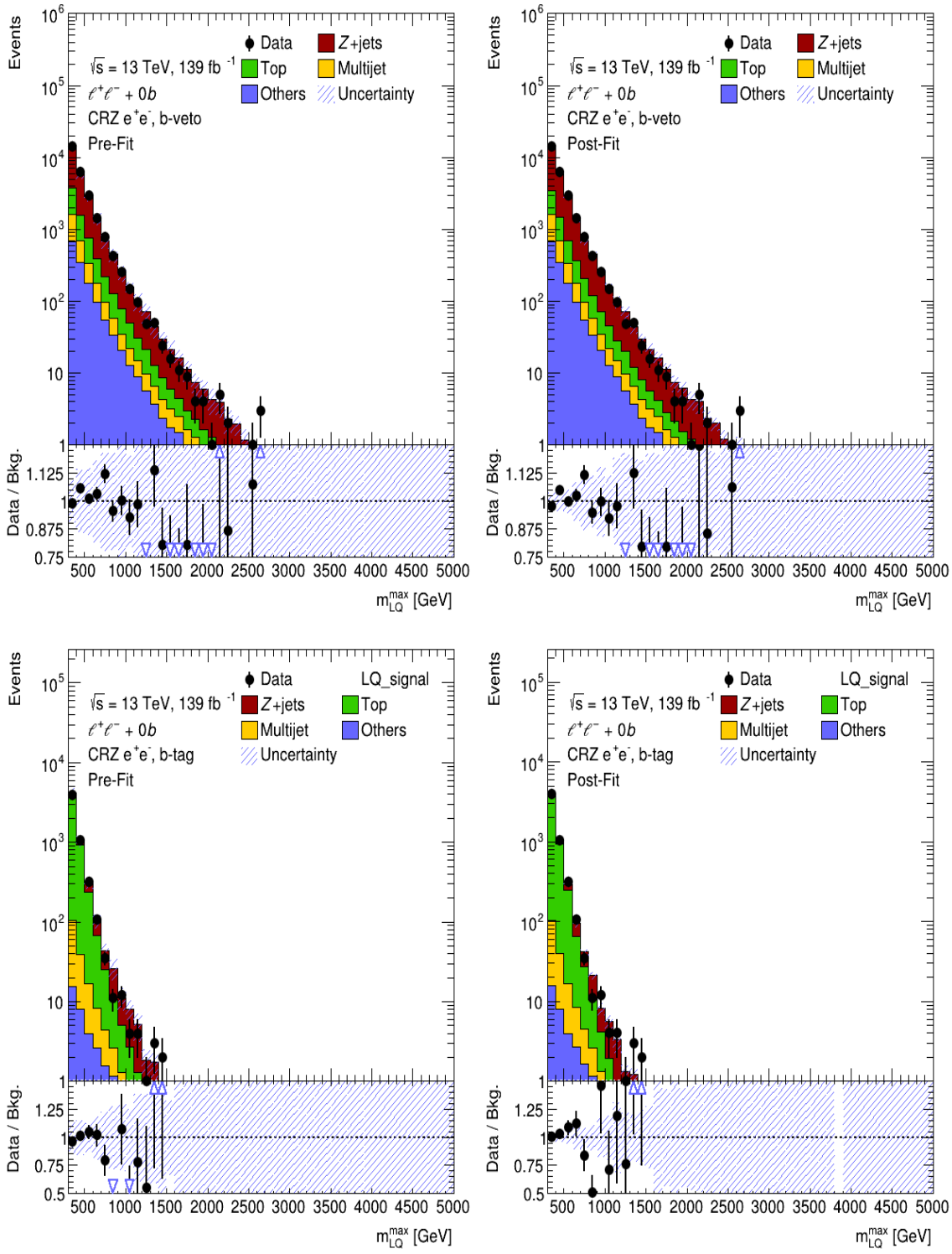


Figure 5.3: *Plots for the electron channel showing the pre-fit and post-fit m_{LQ}^{max} distributions in the Z+jets control region. Top:b-veto, Bottom: b-tag category respectively with the uncertainties both statistical and systematic.*

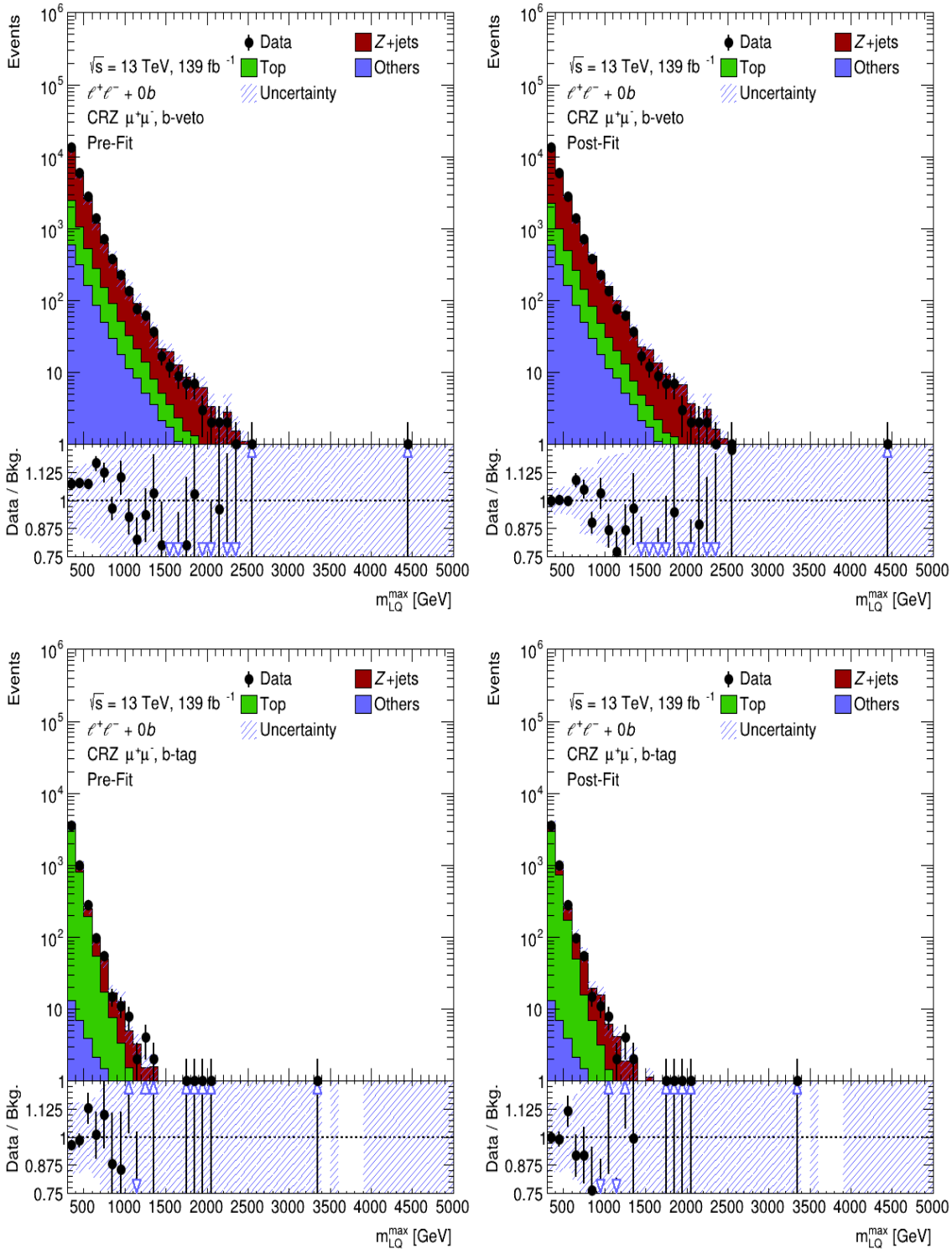


Figure 5.4: *Plots for the muon channel showing the pre-fit and post-fit m_{LQ}^{max} distributions in the Z+jets control region. Top:b-veto, Bottom: b-tag category respectively with the uncertainties both statistical and systematic.*

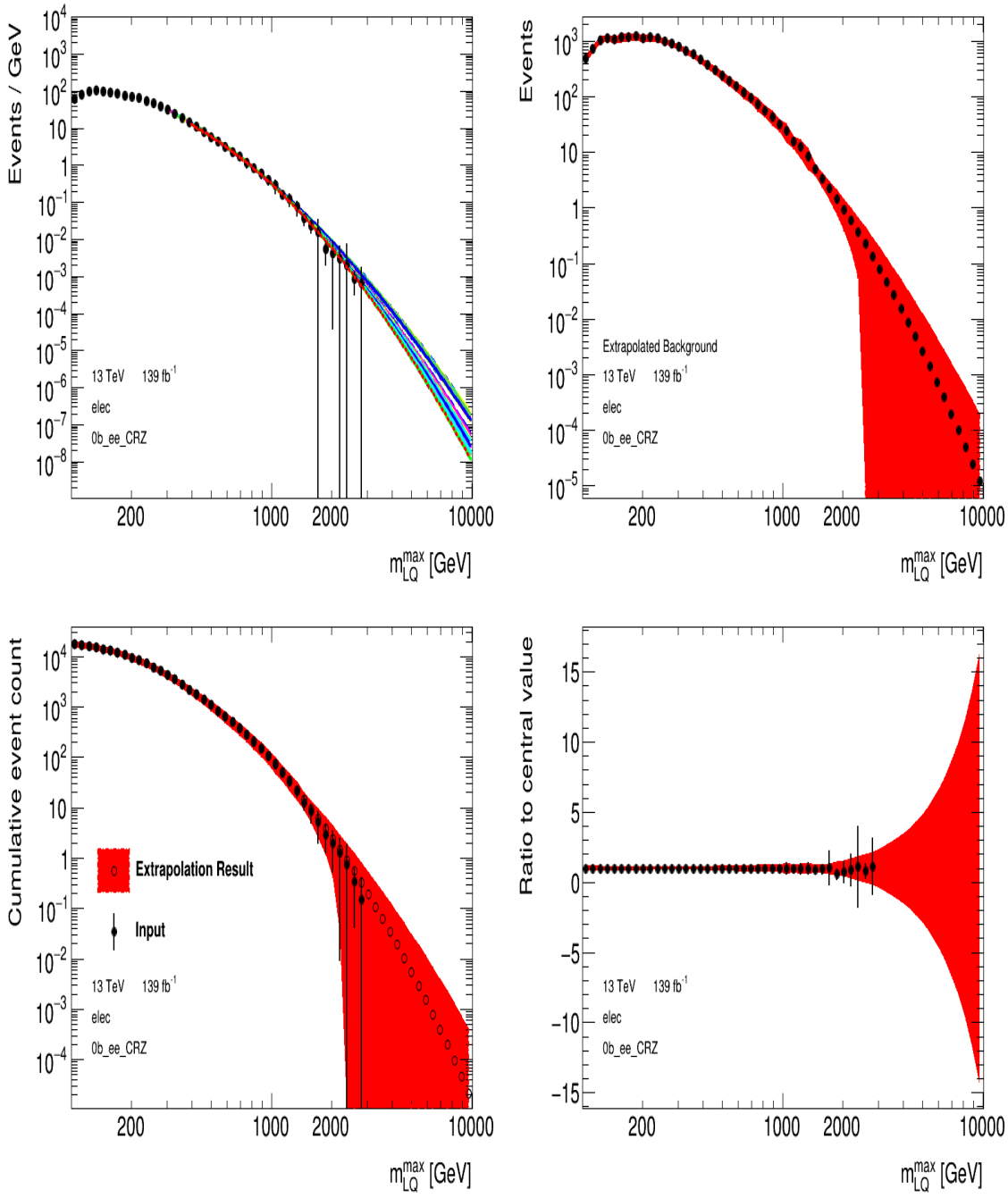


Figure 5.5: *Extrapolation of the high mass LQ top background for the electron b-veto channel in the Z-Control region. Top left are the fits while considering the envelope as uncertainty, where the dash read line is the fit taken as the central value. Top right is the central value with the uncertainty that is obtained from the final estimate. The bottom left shows the cumulative event count that was integrated from the right side of the distribution with the uncertainty shown as the red area while the bottom right shows the ratio of the MC prediction and the central value on the bottom left.*

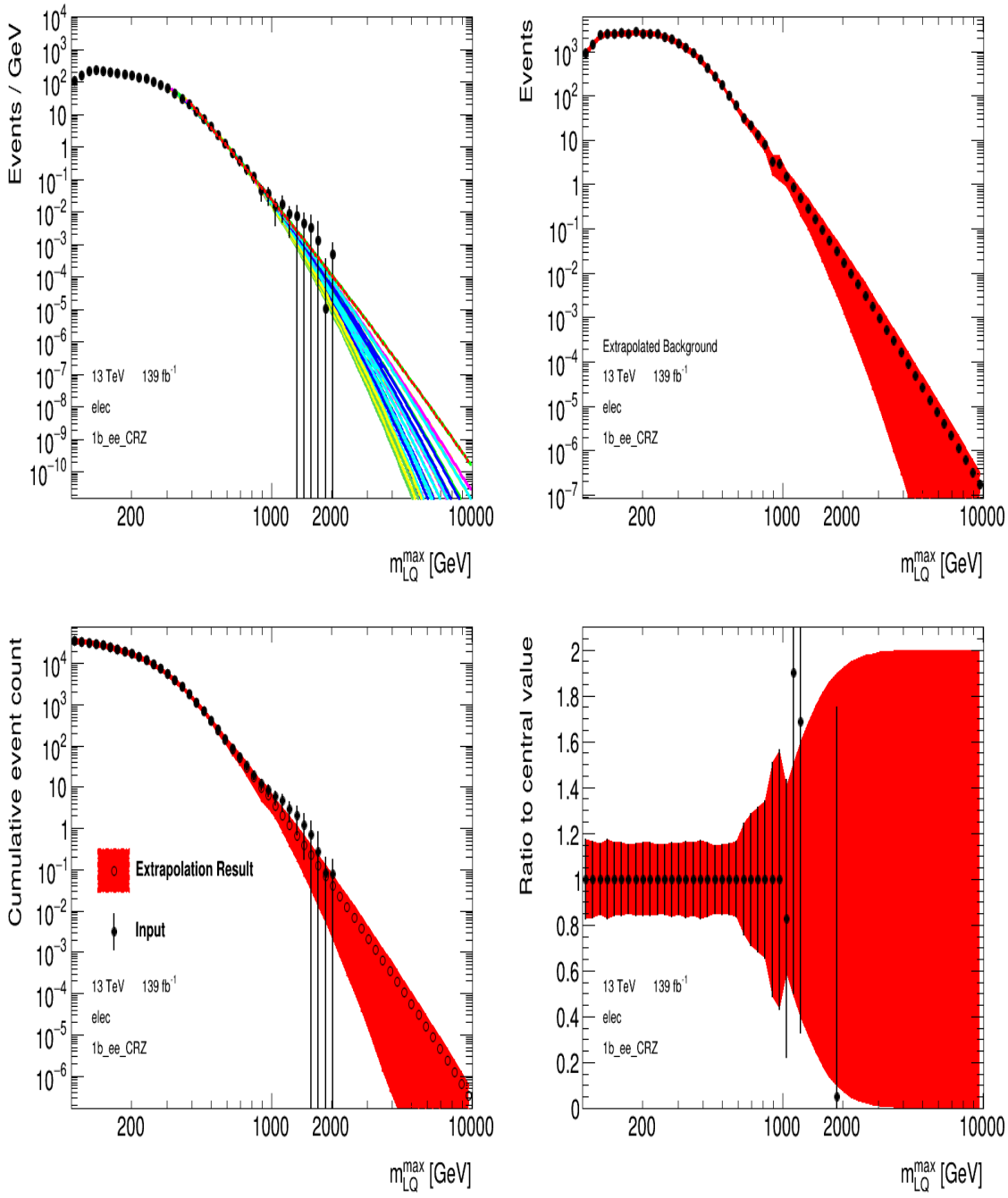


Figure 5.6: *Extrapolation of the high mass LQ top background for the electron b-tag channel in the Z-Control region. Top left are the fits while considering the envelope as uncertainty, where the dash read line is the fit taken as the central value. Top right is the central value with the uncertainty that is obtained from the final estimate. The bottom left shows the cumulative event count that was integrated from the right side of the distribution with the uncertainty shown as the red area while the bottom right shows the ratio of the MC prediction and the central value on the bottom left.*

5.6.2 Top control region (TCR)

The background estimate of the top samples suffered from low statistics in the tails as a result of the inclusive nature of the generation of the samples. To address this problem, an extrapolation is performed using multiple fits with two different functions and varying fit ranges for the m_{LQ}^{max}. The quality factor Q quantifies the agreement of the fit to the tail of the initial distribution, and the nominal value is the function with the best description. The uncertainty is the envelope of all fits that satisfy a certain requirement on Q. A summary of the fit ranges and the various Q-cut values for the various regions is seen on Table 5.5. This model is tested and shows a good data-MC agreement in this region seen in Figures 5.7, 5.8 and Table 5.4. Plots of the extrapolation for some selected channels are shown in Figures 5.5, 5.6, 5.9 and 5.10.

	ee b-veto	ee b-tag	$\mu\mu$ b-veto	$\mu\mu$ b-tag
Z + jets	20345±667	1226±306	20916±909	1131±239
$t\bar{t}$	3418±344	4114±219	3099±328	3883±223
Others	1434±92	34±4	1295±83	30±3
Fakes	1655±40	145±12		
Total	26852±590	5519±243	25310±862	5044±102
Data	26852	5519	25311	5044

Table 5.4: *Post-fit event yield in all channels in the TCR. The uncertainties are both systematic and statistical uncertainties.*

Channel	Region	Background	Lower Range/GeV	Upper Range/GeV	Q-cut Val
Electron	SR b-veto	Top	[200,300]	[1300,1900]	3
	SR b-tag	Top	[400,600]	[1400,1900]	10
	ZCR b-veto	Top	[300,400]	[1300,1800]	30
	ZCR b-tag	Top	[300,400]	[1000,1300]	10
	TCR	Top	[400,600]	[1300,1900]	3
	SR b-veto	Fake	[200,300]	[1300,1900]	1
	SR b-tag	Fake	[200,300]	[1000,1400]	10
	ZCR b-veto	Fake	[200,400]	[1000,1400]	3
	ZCR b-tag	Fake	[180,250]	[700,1000]	0.8
	TCR	Fake	[200,300]	[700,1000]	0.7
Muon	SR b-veto	Top	[400,600]	[1400,1900]	10
	SR b-tag	Top	[400,700]	[1400,1900]	5
	ZCR b-veto	Top	[400,600]	[1200,1800]	10
	ZCR b-tag	Top	[200,400]	[800,1300]	10
	TCR	Top	[300,500]	[1100,1800]	4

Table 5.5: *A summary of the fit ranges and the Q-cut values implemented in the extrapolation for the electron and muon channels for various regions for the analysis.*

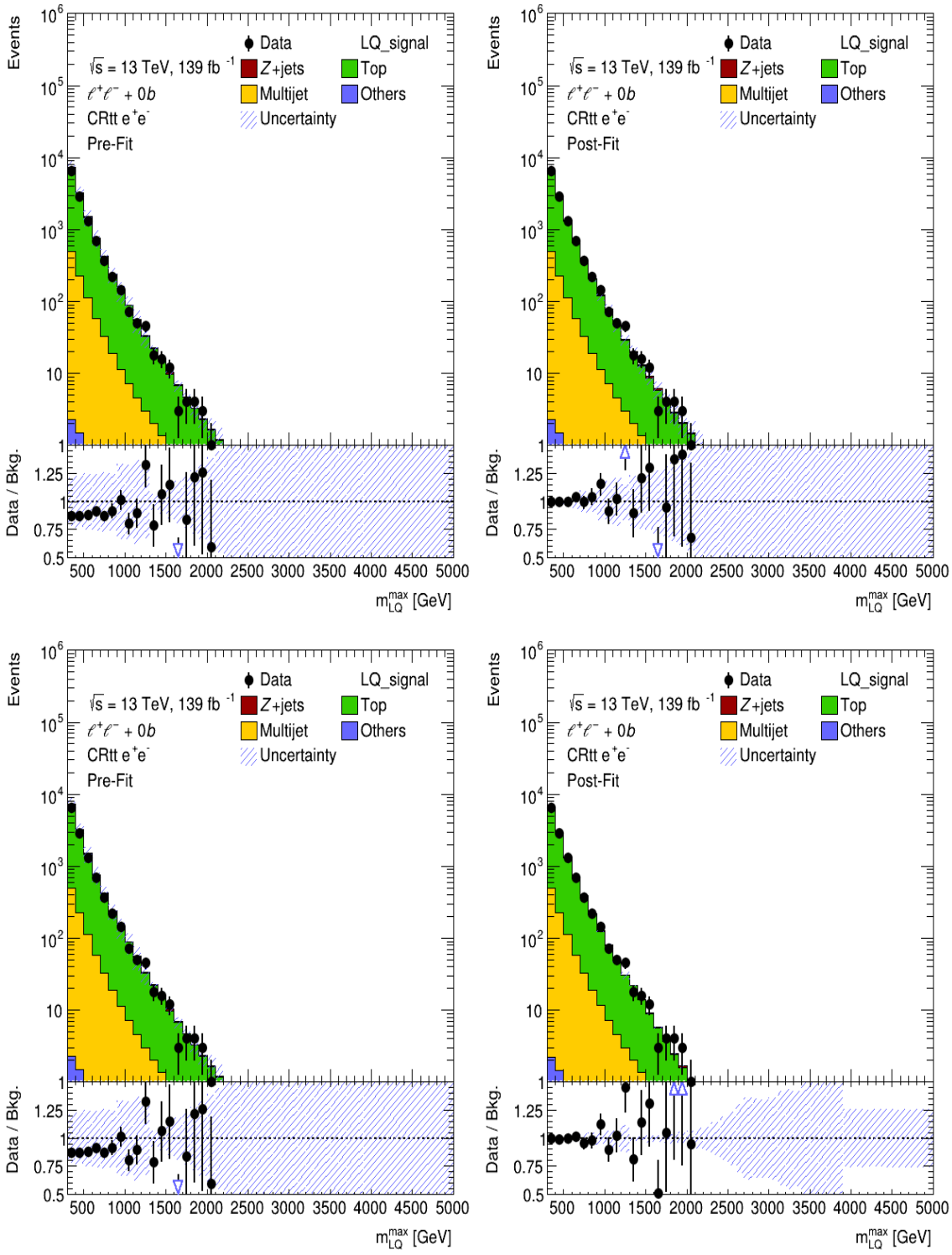


Figure 5.7: *Plots for the electron channel showing the pre-fit and post-fit m_{LQ}^{max} distributions in the TCR control region. Top:b-veto, Bottom: b-tag category respectively with the uncertainties both statistical and systematic.*

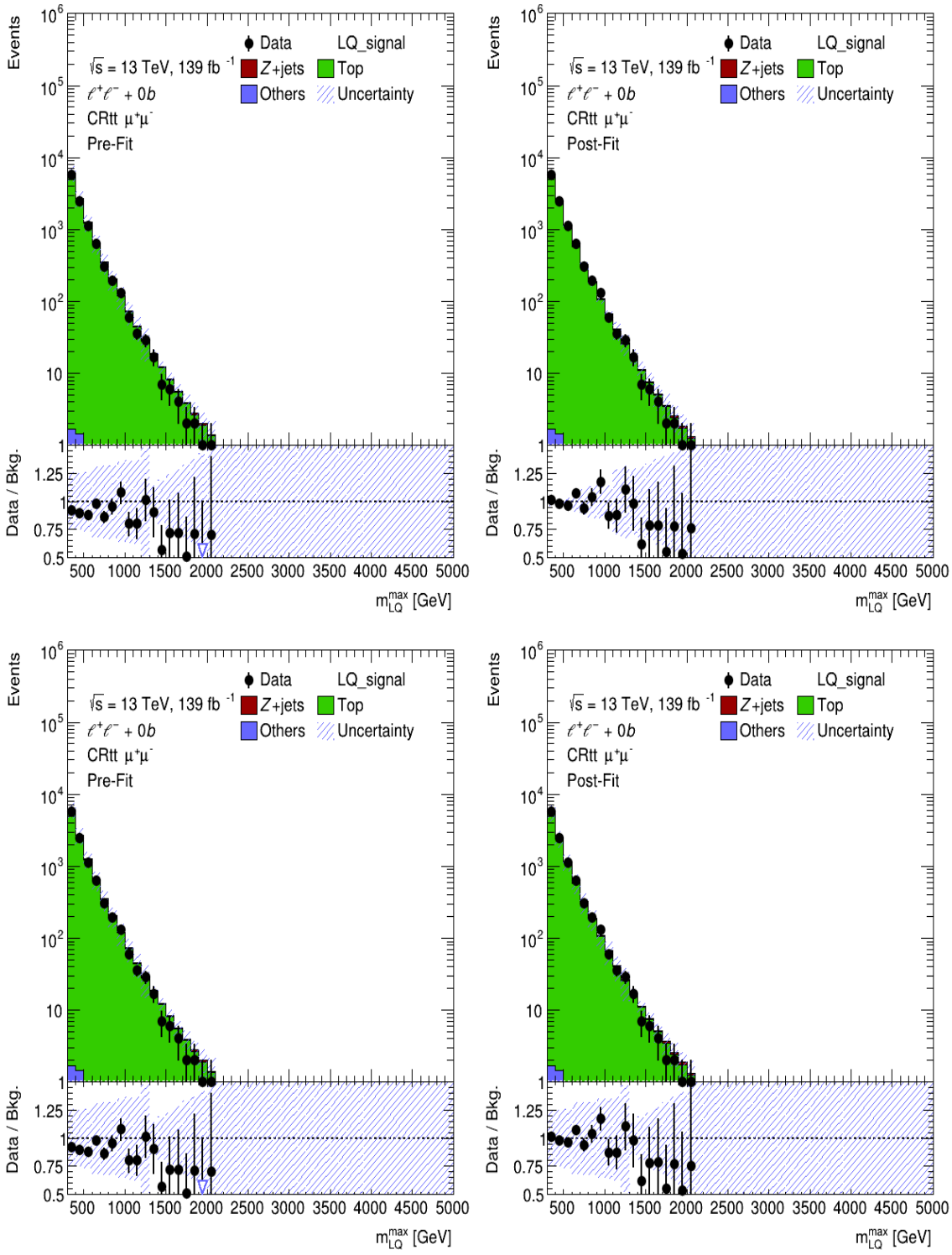


Figure 5.8: *Plots for the muon channel showing the pre-fit and post-fit m_{LQ}^{max} distributions in the TCR control region. Top:b-veto, Bottom: b-tag category respectively with the uncertainties both statistical and systematic.*

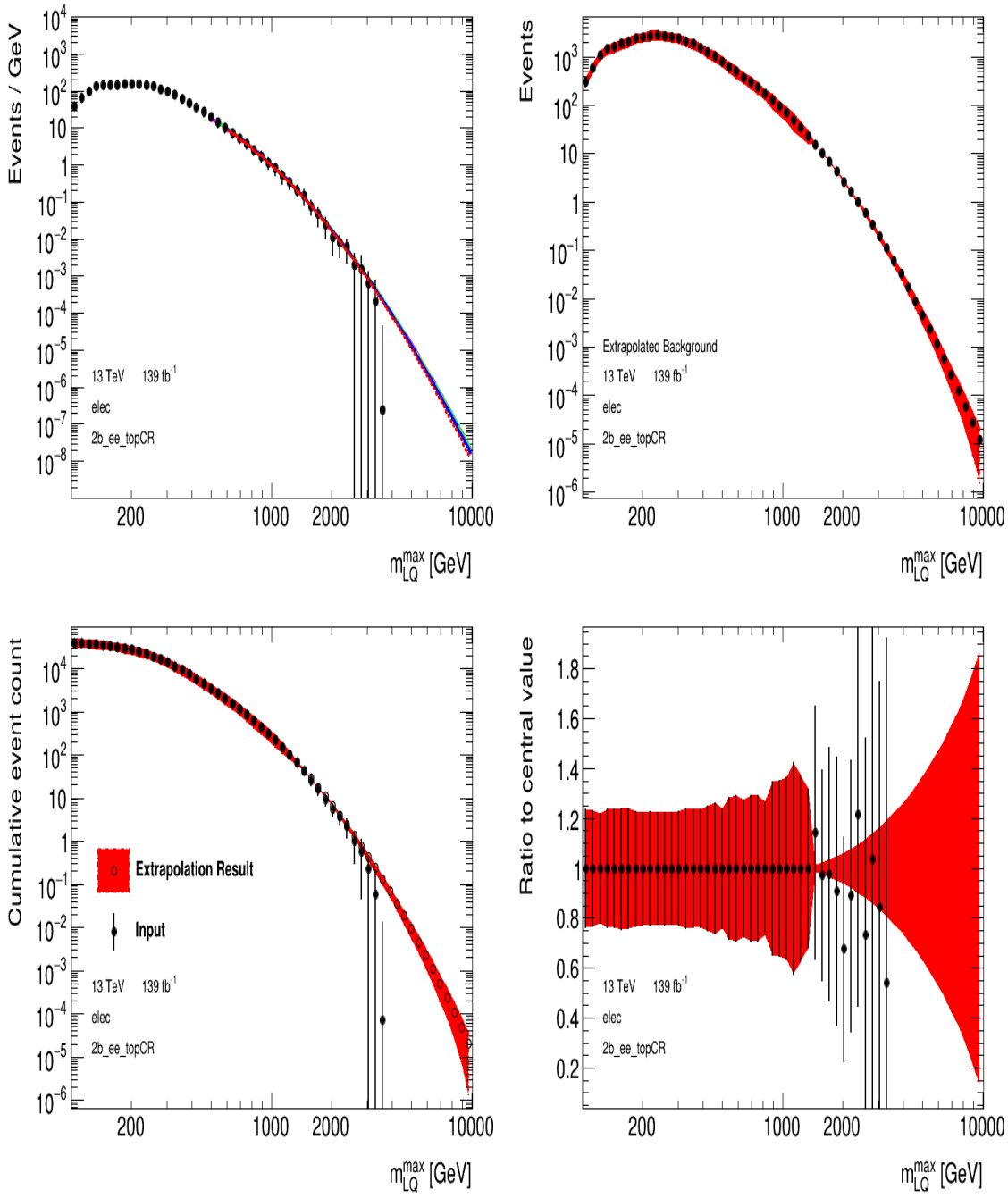


Figure 5.9: *Extrapolation of the high mass LQ top background for the electron channel in the top-Control region. Top left are the fits while considering the envelope as uncertainty, where the dash read line is the fit taken as the central value. Top right is the central value with the uncertainty that is obtained from the final estimate. The bottom left shows the cumulative event count that was integrated from the right side of the distribution with the uncertainty shown as the red area while the bottom right shows the ratio of the MC prediction and the central value on the bottom left.*

5.6.3 Validation region

The aim of this region is to validate the modelling of the main background, (Z + jets and top). A reasonable agreement between data and MC is seen in this region as seen on Table 5.6 and the pre-fit and post-fit plots in Figures 5.11 and 5.12.

	ee b-veto	ee b-tag	$\mu\mu$ b-veto	$\mu\mu$ b-tag
Z + jets	6021±395	330±77	5919±418	261±63
$t\bar{t}$	1768±164	2940±176	1573±155	2745±158
Others	656±45	15±2	579±38	13±2
Fakes	553±23	155±8		
Total	8997±411	3440±131	8071±445	3018±117
Data	9639	3609	8326	3072

Table 5.6: *Post-fit event yield for all channels in the validation region. The uncertainties are both systematic and statistical uncertainties.*

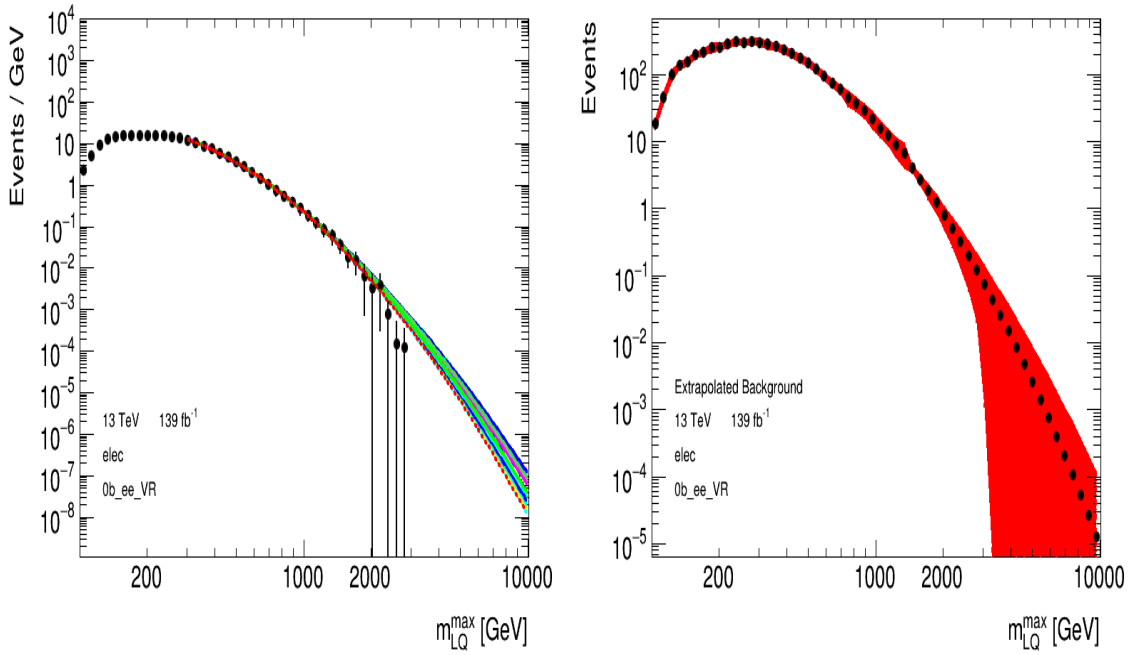


Figure 5.10: *Extrapolation of the high mass LQ top background for the electron channel in the VR region. Left are the fits while considering the envelope as uncertainty, where the dash read line is the fit taken as the central value. Right is the central value with the uncertainty that is obtained from the final estimate.*

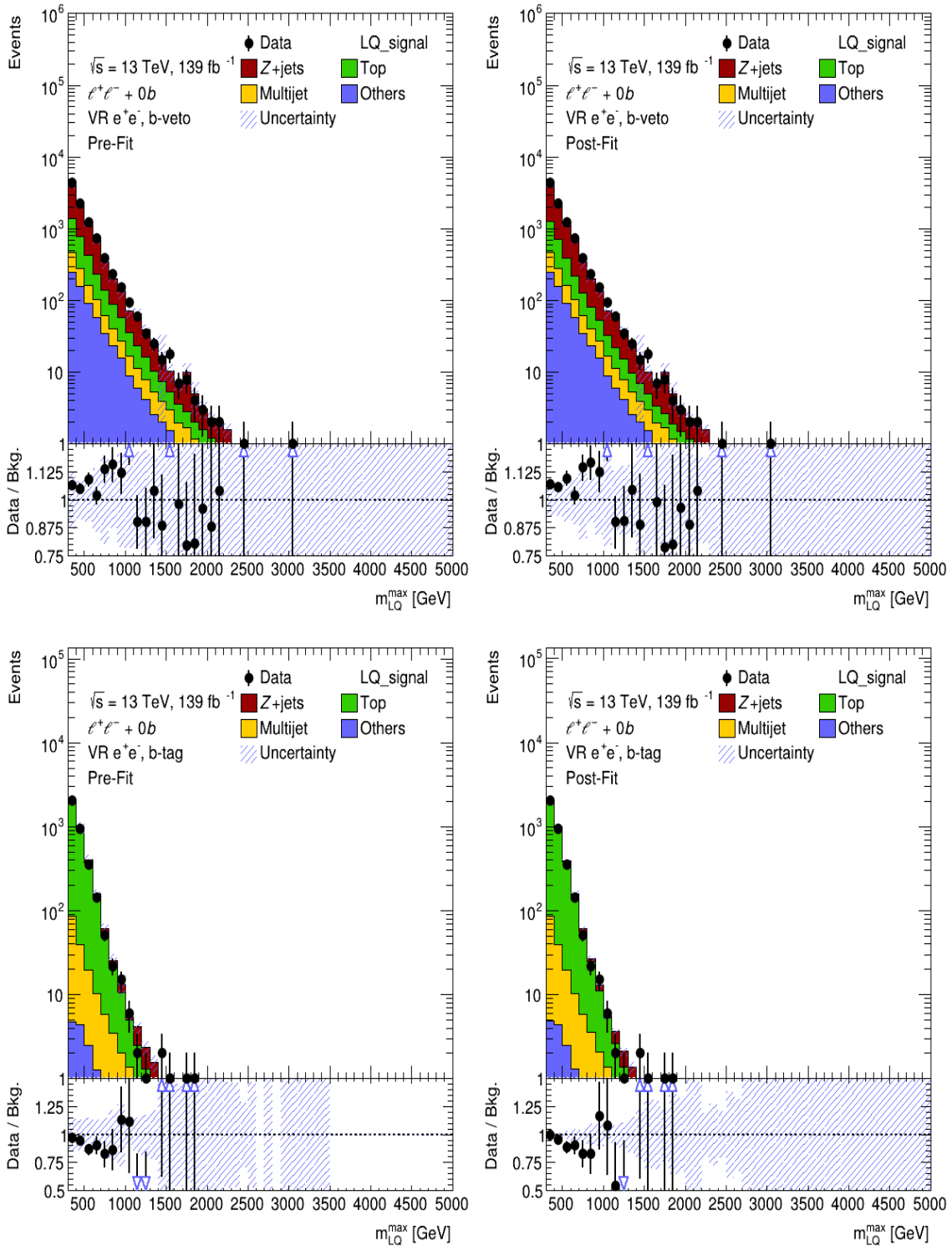


Figure 5.11: *Plots for the electron channel showing the pre-fit and post-fit m_{LQ}^{max} distributions in the VR region. Top:b-veto, Bottom: b-tag category respectively with the uncertainties both statistical and systematic.*

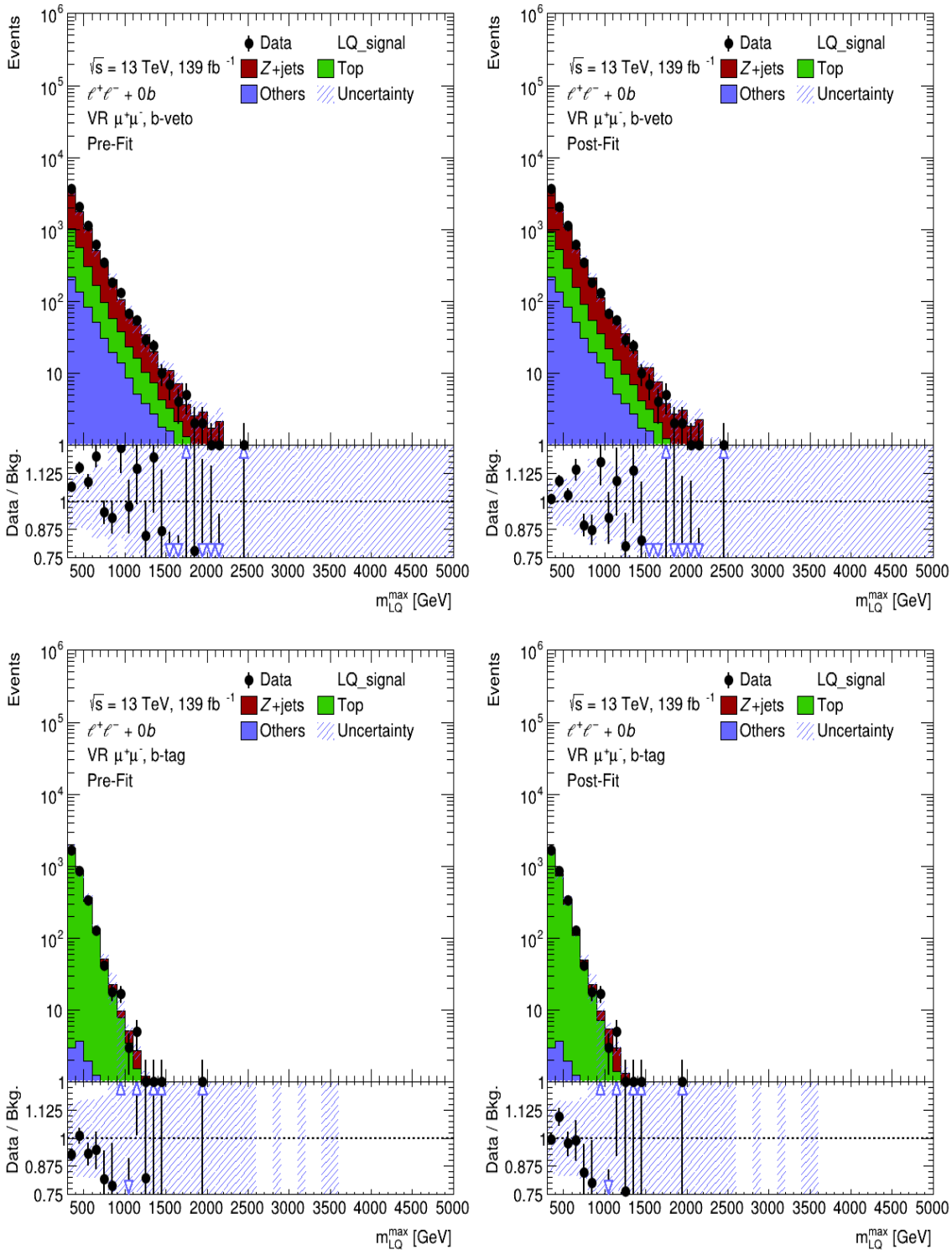


Figure 5.12: *Plots for the muon channel showing the pre-fit and post-fit m_{LQ}^{max} distributions in the VR region. Top:b-veto, Bottom: b-tag category respectively with the uncertainties both statistical and systematic.*

5.7 Systematic uncertainty

Systematic uncertainties have been discussed in section 4.14. The uncertainties for muons are derived from data using Z→ $\mu\mu$ decays [158] similar procedure for electron uncertainties discussed in section 4.14. This analysis uses small-radius jets but the uncertainties are derived similarly to those of the large-radius jet discussed in section 4.14. In this analysis, the *StrongReduction* settings were applied for the JES uncertainty which consists of 7 nuisance parameters. The *SimpleJER* settings were applied for the JER [159] uncertainty which consists of 8 nuisance parameters. Data [160] for c-jets, b-jetsc and other light jets are used to derive uncertainties in the b-tagging efficiency. Events from dileptonic $t\bar{t}$ are used [161] to derive the uncertainty and the b-tagging efficiency for b-jets. MC simulations are used in order to derive additional uncertainties by extrapolating this efficiency beyond the kinematic reach of the calibration. All MC distributions are reweighted so that they correspond to data distribution. The reweighting is varied within its uncertainty so as to assess the associate systematic uncertainty.

5.7.1 Theory uncertainties

Evaluation of theoretical uncertainties was done for all the MC samples. In order to model the Z+jets and multiboson background (SHERPA samples), the additional stored event weights in the truth record are applied to derive the impact of their systematics instead of the nominal event weights. These weights account for the choice of the PDF as well as variation of the renormalization, μ_r and factorization, μ_f scale. A 7-point variation of the renormalization and factorization scales in the matrix elements is used to evaluate QCD scale uncertainties on the fly [162]. While avoiding opposite factors, the scales are independently varied by factors of 0.5 and 2. The 100 variation replicas together with the ± 0.001 α_S are used to evaluate that nominal PDF set uncertainties. In addition, the uncertainty is the difference between the nominal and the central values of the CT14NNLO [163] and MMHT2014NNLO [164] PDF sets. By calculating the envelope and symmetrization, the uncertainties are combined into one nuisance parameter.

The cross-section uncertainty for $t\bar{t}$ production has the value of +5.6%/-6.1% [165] assigned to it. This is derived from the PDF+α_s, scale, and the top mass uncertainties. The t-channel, s-channel, and tW-channel single top processes have assigned cross-section uncertainties of +4.3%/-3.7%, +4.4%/-4.1% and +5.4%/-5.4%, respectively. The cross section uncertainties for the $t\bar{t}$ +W and $t\bar{t}$ +Z processes are +13.3%/-12.0% and +10.4%/-12.0% respectively. In this analysis, all the top processes are combined and treated with a single nuisance parameter.

In order to estimate uncertainty due to interference, a comparison was made between the nominal POWHEG + PYTHIA8 sample used for top background estimation and an alternative sample that was generated using the diagram subtraction scheme [86, 147]. The nominal was compared with aMcAtNLO sample to determine the uncertainty due to the matrix element, and HERWIG 7 sample to determine the uncertainty due to the parton shower. The factorization and renormalization scales are derived by reducing

and increasing them by a factor of 0.5 and 2.0 while comparing to the nominal to check their impact. Higher parton radiation is simulated by varying the factorization and renormalization scales by a factor of 0.5 in the ME with the var3c up variation from the A14 tune being used. The factorization and normalization scales are varied by a factor of 2 while using the PS Var3c down variation to simulate lower parton radiation. The PS weights which vary the QCD emission in the final-state-radiation (FSR) renormalization scale by a factor of 0.5 and 2.0 respectively are used to evaluate the impact of the FSR. To derive the PDF uncertainty, 30 Hessian eigenvector (EV) sets were used as recommended in [166]. The same procedure for $t\bar{t}$ production uncertainty is also used for single top production. A summary of the theory uncertainty nuisance parameters for $t\bar{t}$ and single top MC samples is seen in Table 5.7.

Nuisance parameter name	variation
Cross section	overall
Matrix element (Compare with aMcAtNlo)	symmetric
Parton shower (Compare with HERWIG 7)	symmetric
Scale μ_R/μ_F	up / down, symmetric
ISR α_s (A14 Var3c, vary ISR α_s)	up / down, symmetric
FSR α_s (A14 Var2, vary FSR α_s)	up / down, symmetric
PDF_set_90901-30	symmetric

Table 5.7: *A summary of the theory uncertainty nuisance parameters for single top and* $t\bar{t}$ *MC samples.*

A different generator for the parton shower (HERWIG 7) instead of PYTHIA 8 is used to derive the parton shower uncertainty fot the $t\bar{t}V$ samples. The factorization and renormalization scales are reduced and increased by a factor of 0.5 and 2.0 while comparing with the nominal to derive their impact. To derive the PDF uncertainty, the 30 EV recommendation in [166] was used similar to the $t\bar{t}$ sample. A summary of the theory uncertainty nuisance parameters for $t\bar{t}V$ MC samples is seen in Table 5.8.

Nuisance parameter name	variation
Cross section	overall
Parton shower (Compare with HERWIG 7)	symmetric
Scale μ_R/μ_F	up / down, symmetric
PDF_set_90901-30	symmetric

Table 5.8: *A summary of the theory uncertainty nuisance parameters for* $t\bar{t}V$ *MC samples.*

5.8 Statistical analysis and results

This section deals the statistical analysis and results of the expected and observed exclusion limits.

5.8.1 Likelihood Ratio Test

The likelihood ratio test procedure is carried out in order to search for signal-like deviations in data from the background only fit. To determine this, the test statistics used is in equation 5.8.1.

$$t = \begin{cases} 0 & if \quad \hat{\mu} < 0 \\ -2ln\frac{L(0)}{L(\hat{\mu})} & if \quad 0 \leq \hat{\mu} \end{cases} \tag{5.8.1}$$

where L is the likelihood function. The signal cross-section dependency is parameterized into $\mu = \sigma B/(\sigma B)_{LQ}$ (signal strength parameter). The value of μ with the maximum likelihood L for the measured data n is $\hat{\mu}$. The first line of equation 5.8.1 ensures no negative interference effects. Integrating the probability distribution of the test statistics under the background-only hypothesis in the tail, beginning from the observed t_obs, the observer p-value (p_0) for the given data is obtained as seen in equation 5.8.2.

$$p_0 = \int_0^\infty f(t|\mu = \hat{0}, \theta_{obs})dt \tag{5.8.2}$$

By varying the background-only hypothesis, the probability distribution function in equation 5.8.2 is obtained. Equation 5.8.3 quantifies the p-values using Gaussian standard deviations, with the Φ^{-1} (inverse Gaussian probability density function) adopted for better comparison.

$$z = \Phi^{-1}(p_0) \tag{5.8.3}$$

Where z is the significance. An asymptotic approximation using Wilk's theorem [167] is used so as to limit the computing consumption. The relationship between the significance, p_0 and t_{obs} from this approximation is seen in equation 5.8.4.

$$p_0 = 1 - \Phi(\sqrt{t_{obs}}), \; z = \sqrt{t_{obs}} \tag{5.8.4}$$

5.8.2 Exclusion limits

A single-bin likelihood fit to data is performed on the signal, validation, and control regions for the ee/$\mu\mu$ b-veto/b-tag category. The signal strength modifier μ is the parameter of interest in this case and the reconstructed mass of the LQ is the discriminating variable. A simultaneous fitting of the signal and control region is carried out including the nuisance parameters (systematic uncertainties). The two main background processes modelling in this combined fit were adjusted from the changes in the nuisance parameters in order for the background prediction in the signal region to improve. The effect of the systematic, theory, and statistical uncertainties for all the regions is seen in the correlation result. This is evaluated from the signal + background fit in both the control and signal regions. The fit is performed on data in the control region while the Asimov data with an injected signal strength μ = 10 is fitted in the signal region. The signal strength quantifies the production cross-section times the branching ratio, $\sigma \times \beta$ of the LQ. The optimal cut value is arrived at from the variation of the cut value between the range of -1000 GeV and +400 GeV of the simulated LQ mass with steps of

100 GeV to calculate the upper limit on $\sigma \times \beta$. The cut value with the strongest limit is chosen.

5.8.3 Electron b-veto channel

For each LQ mass point, the cut value that gives the strongest limit and the expected upper limit is shown on Table 5.9.

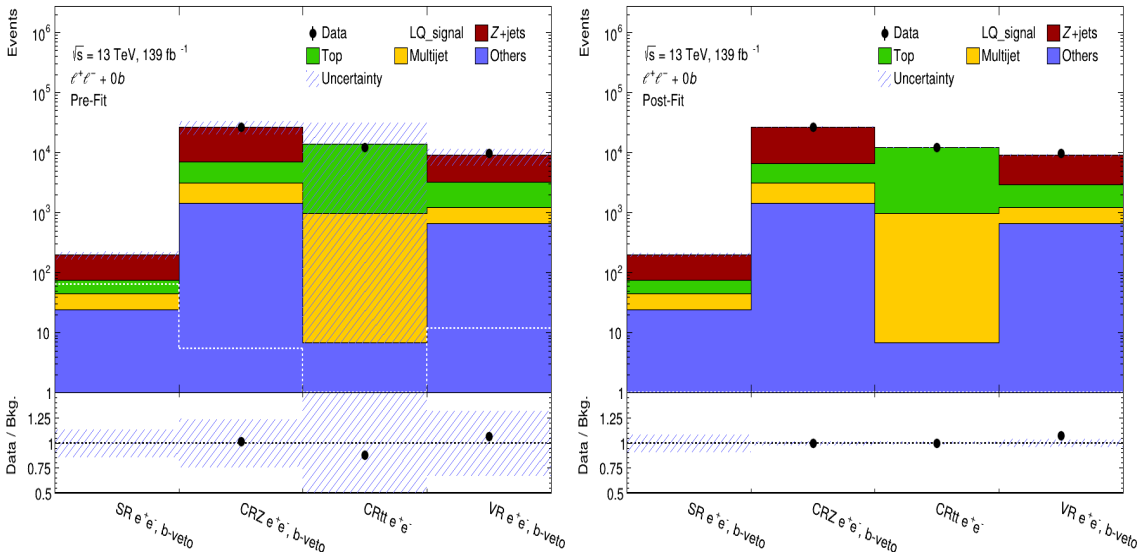


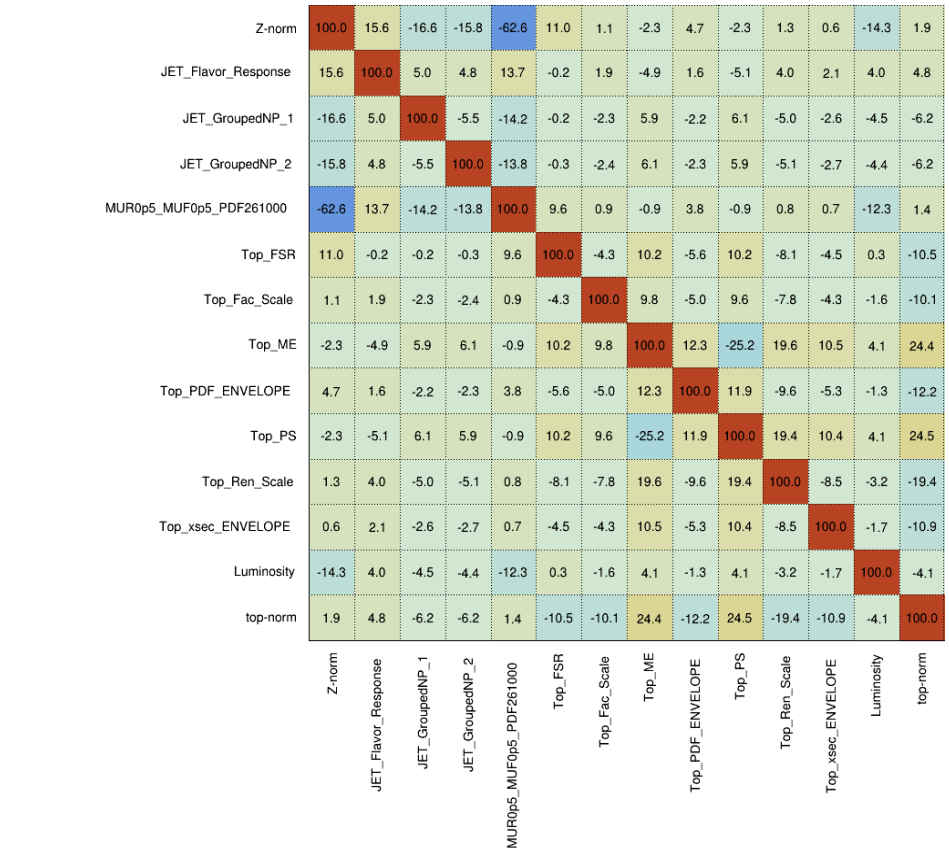
Figure 5.13: *Pre-fit and post-fit event yields in the signal, control and validation regions. The signal considered here is the 1200GeV LQ mass hypothesis, corresponding to a cut value of 1100 GeV coupling to strange quarks. The Uncertainties are both systematic and statistical uncertainties.*

A summary of the pre-fit and post-fit yields in the signal, control and validation regions with the expected number of events for the different backgrounds are shown on Figure 5.13.

m_{LQ}[GeV]	m_{LQ}^{max} cut [GeV]	UL [pb]
500	500	3.47194e-02
750	900	1.09464e-02
1000	900	2.60914e-03
1100	1100	1.90592e-03
1200	1100	1.06436e-03
1300	1200	8.91451e-04
1400	1300	7.22726e-04
1500	1300	6.27467e-04
1600	1500	5.31628e-04
1700	1500	4.60307e-04
1800	1700	3.91817e-04
1900	1700	3.36423e-04
2000	1700	3.20331e-04
2100	1900	2.90038e-04
2200	2000	2.61085e-04
2300	2100	2.32276e-04
2400	2200	2.09399e-04
2500	2300	1.92834e-04
2750	2600	1.5124e-04
3000	2700	1.21264e-04
3250	3000	1.05597e-04
3500	3200	7.3529e-05

Table 5.9: *A summary of the cut value of the LQ mass with the best upper limit on the signal strength for each LQ mass for the b-veto, e-channel.*

The extracted post-fit renormalization of the $t\bar{t}$ and z+jets using the background-only fit (where signal cross-section σ is set to zero) are shown in Figure 5.14. The normalization of the $t\bar{t}$ background changes by 0.96 ± 0.06 while that of Z+jets changes by 1.80 ± 0.04. Large uncertainties are expected to cause the poorer Z+jets background normalization. From the background-only fit, a summary of the linear correlation of the nuisance parameters is seen also in Figure 5.14. The ranking plots showing the impact of each nuisance parameter on the signal strength are shown in Figure 5.15. The expected upper limit on the production cross-section multiplied by the branching ratio for each mass of the LQ together with the model interpretation is shown in Figure 5.16.



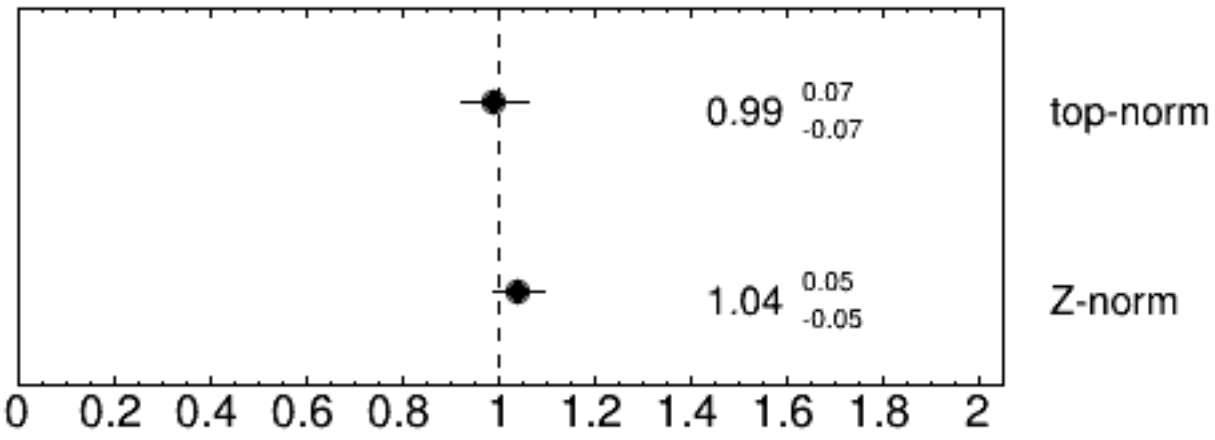


Figure 5.14: *The reduced correlation matrix of the nuisance parameters from the background only fit and the post-fit normalization parameters.*

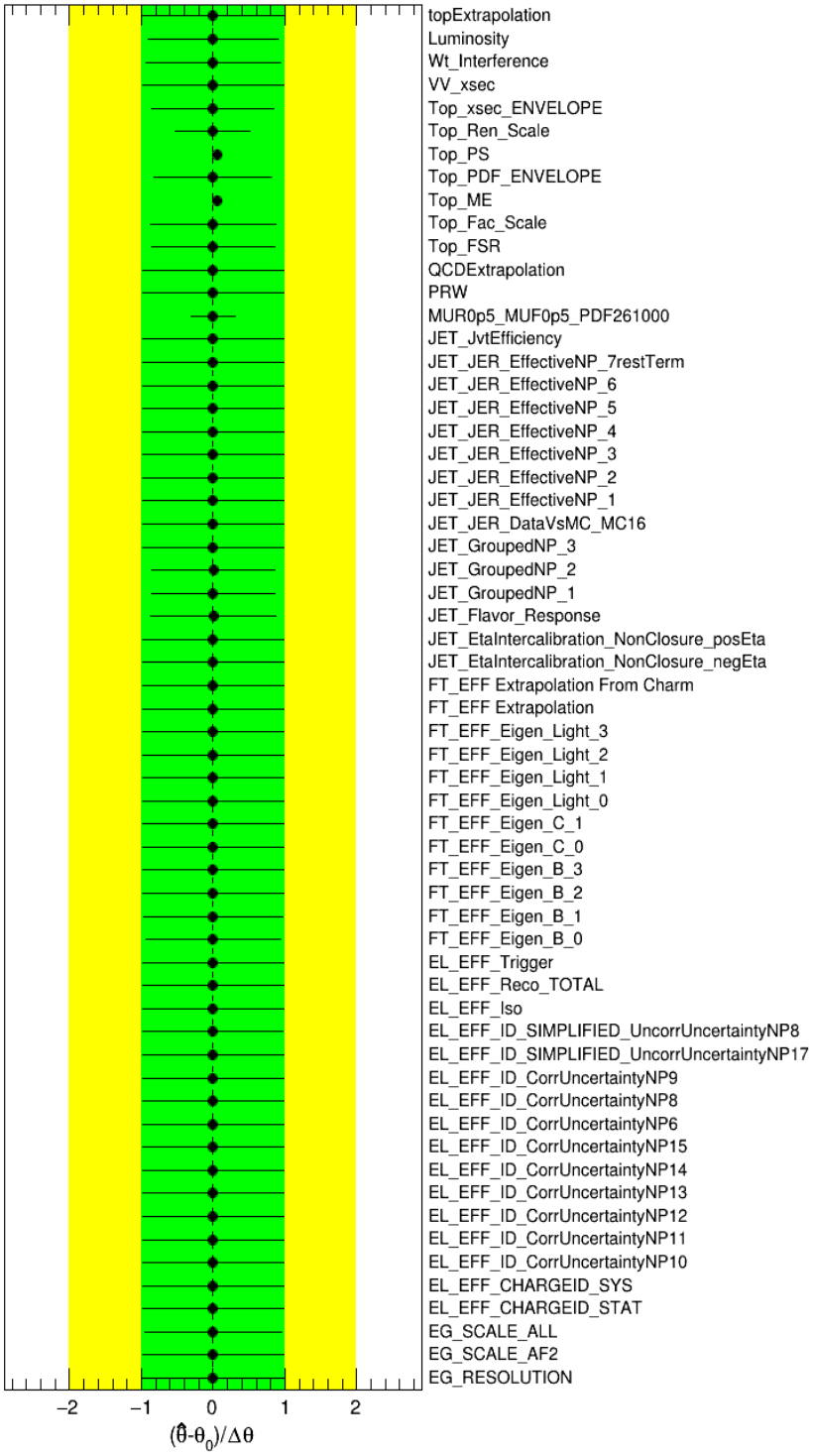


Figure 5.15: *Ranking plot of the nuisance parameters from the impact on the signal strength μ, from the variation of the uncertainty by sigma up and down.*

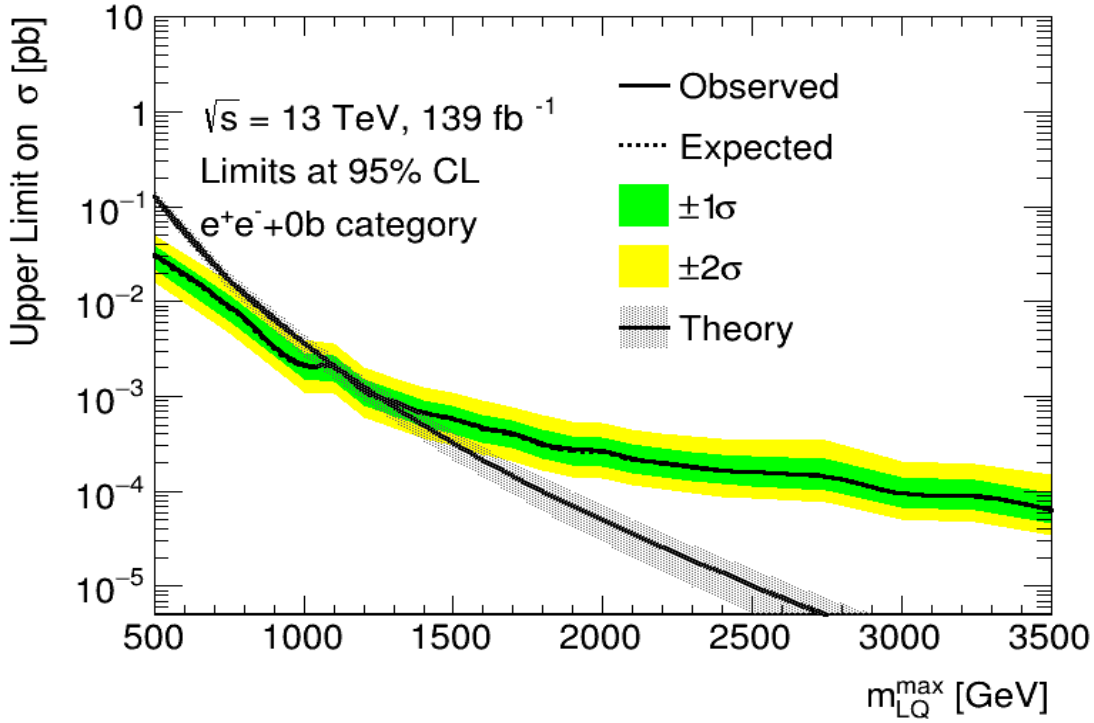


Figure 5.16: *Expected upper limit at 95 % confidence level (CL) on the LQ production cross section for different leptoquark masses. The grey line represent the LQ cross section and the hazed area, the uncertainty at leading order.*

5.8.4 Electron b-tag channel

A summary of the pre-fit and post-fit yields in the signal, control, and validation regions with the expected number of events for the different backgrounds are shown in Figure 5.17. The cut value for each LQ mass that gives the strongest limit and the expected upper limit is shown in Table 5.10. Figure 5.18 show the linear correlations of the nuisance parameters from the background only fit as well as the post-fit normalization of $t\bar{t}$ and Z+jets backgrounds. The overall top background normalization changes by 0.96 $\pm$0.06 while that of Z+jets changes by 1.80 $\pm$ 0.40. Poor purity and larger systematic uncertainties are expected to be responsible for the poor constraint of the Z+jets normalization. The impact of the nuisance parameter on the signal strength is evaluated in a similar manner as performed for b-veto. The corresponding ranking plots are shown in Figure 5.19. The expected upper limit on the production cross-section multiplied by the branching ratio for all LQ masses together with the model interpretation is shown in Figure 5.20 for this region.

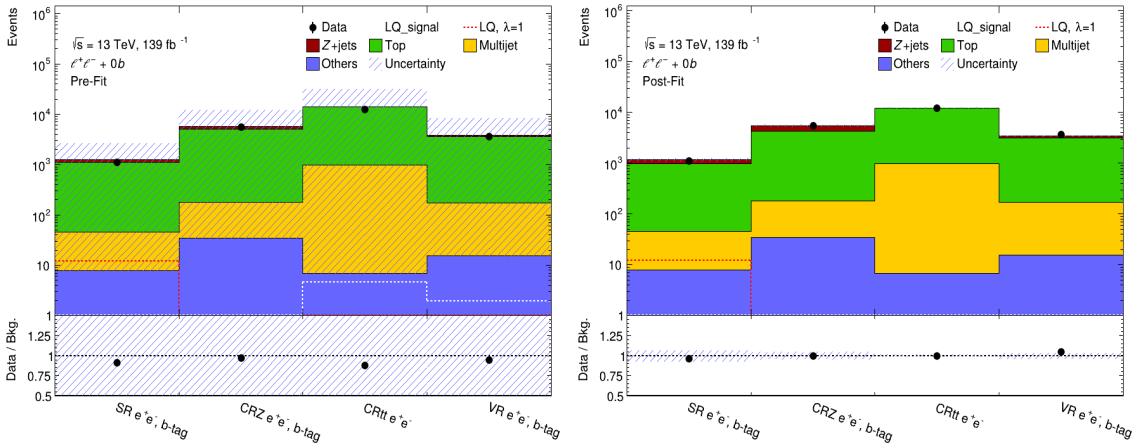
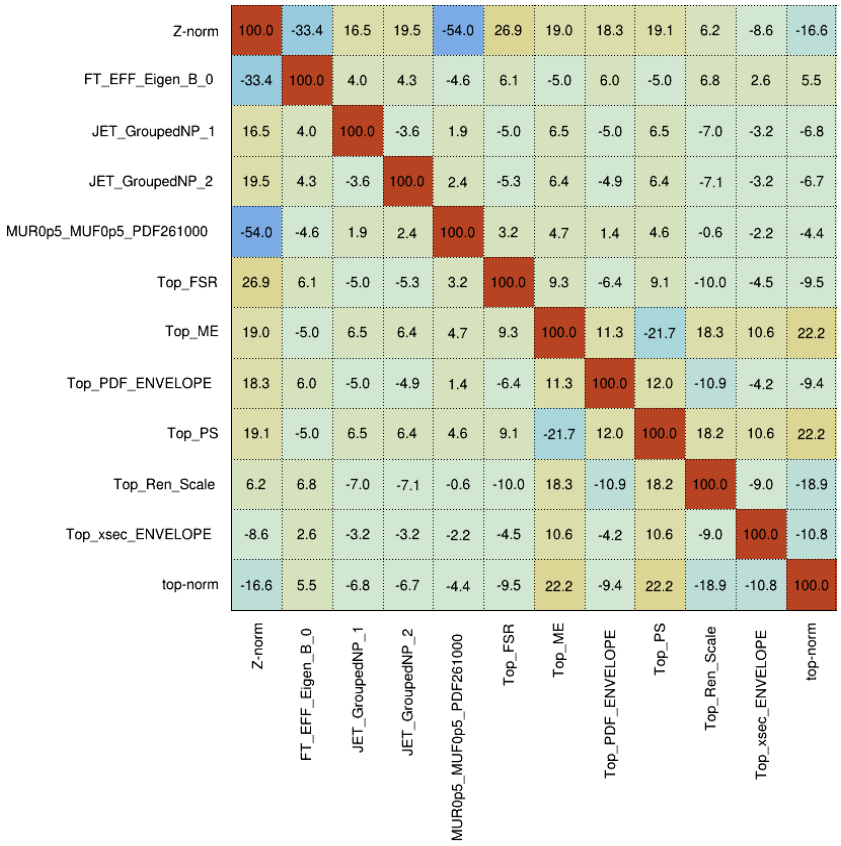


Figure 5.17: *Pre-fit and post-fit event yields in the signal, control and validation regions. The signal considered here is the 1200GeV LQ mass hypothesis, corresponding to a cut value of 1100 GeV coupling to bottom quarks. The Uncertainties are both systematic and statistical uncertainties.*

m_{LQ}[GeV]	m_{LQ}^{max} cut [GeV]	UL [pb]
500	400	1.1197e-02
750	700	2.57324e-02
1000	800	1.36933e-03
1100	800	1.211801e-03
1200	1100	1.14344e-03
1300	1100	9.39003e-04
1400	1200	8.26546e-04
1500	1300	7.00587e-04
1600	1400	6.20269e-04
1700	1400	5.69411e-04
1800	1600	5.05509e-04
1900	1600	4.57742e-04
2000	1700	4.30035e-04
2100	1800	4.16485e-04
2200	1800	3.87809e-04
2300	1900	3.72068e-04
2400	2000	3.60428e-04
2500	2000	3.47492e-04
2750	2000	3.33221e-04
3000	2300	3.30163e-04
3250	2500	3.25657e-04
3500	2700	3.26262e-05

Table 5.10: *A summary of the cut value of the LQ mass with the best upper limit on the signal strength for each LQ mass for the b-veto, e-channel.*



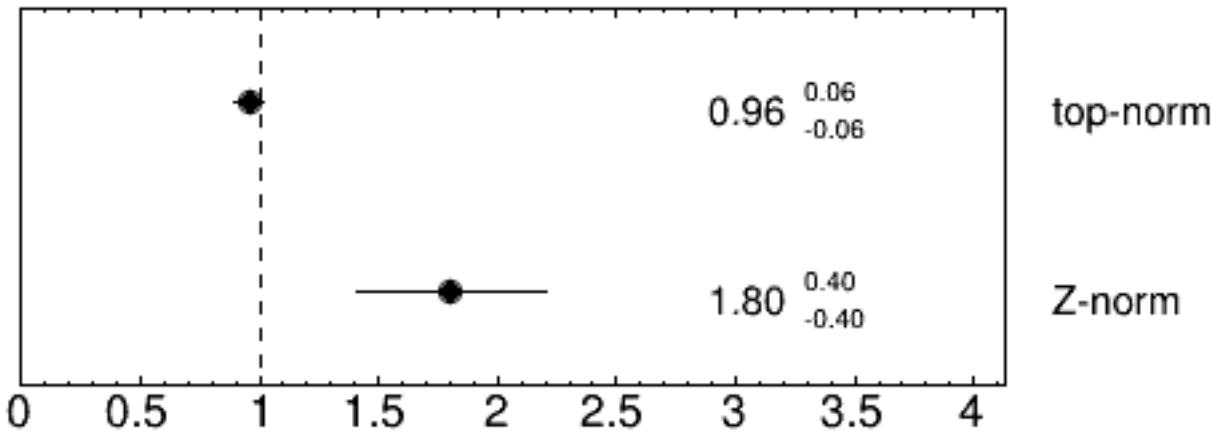


Figure 5.18: *The reduced correlation matrix of the nuisance parameters from the background only fit and the post-fit normalization parameters for this region.*

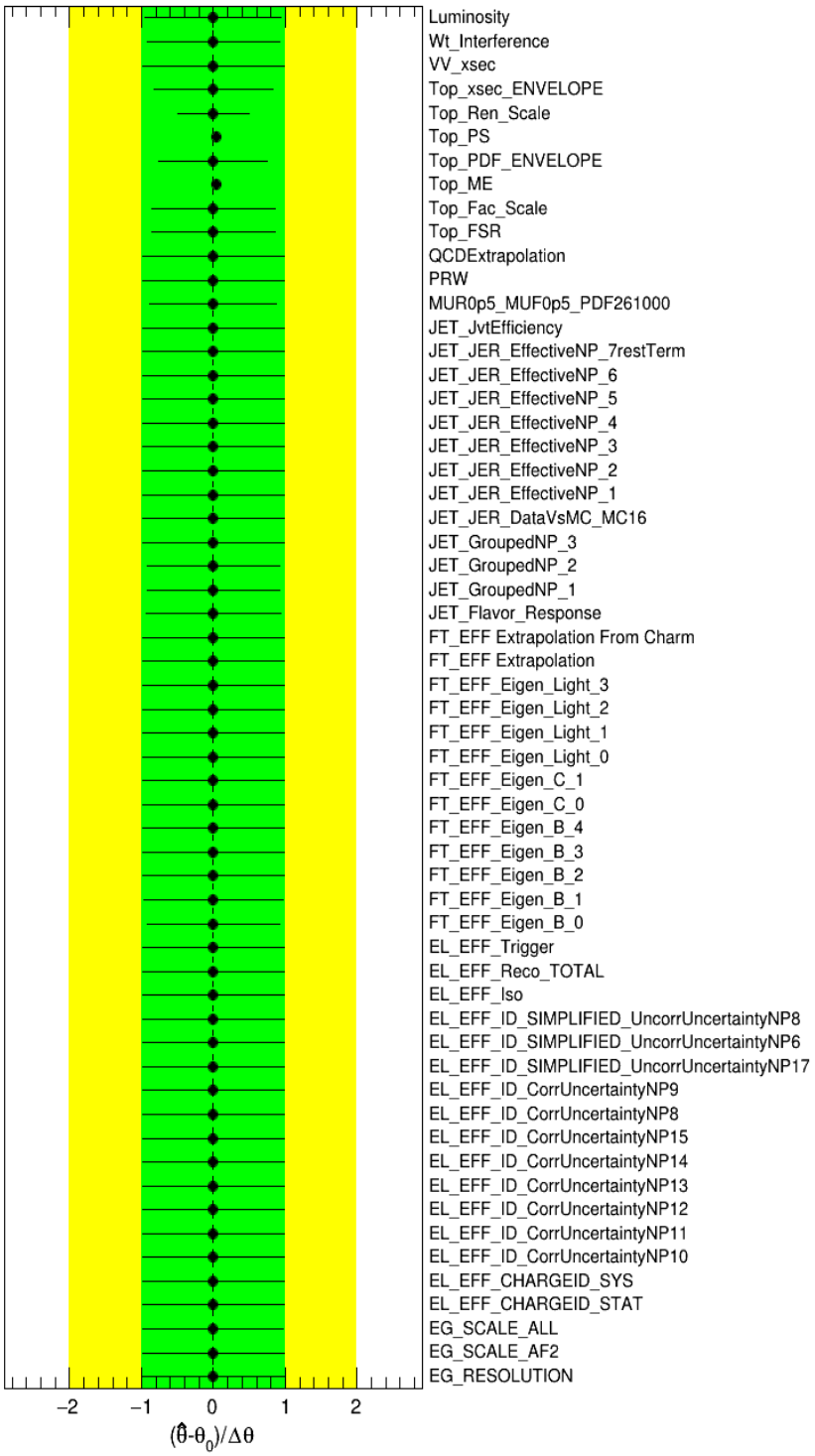


Figure 5.19: *Ranking plot of the nuisance parameters from the impact on the signal strength μ, from the variation of the uncertainty by sigma up and down.*

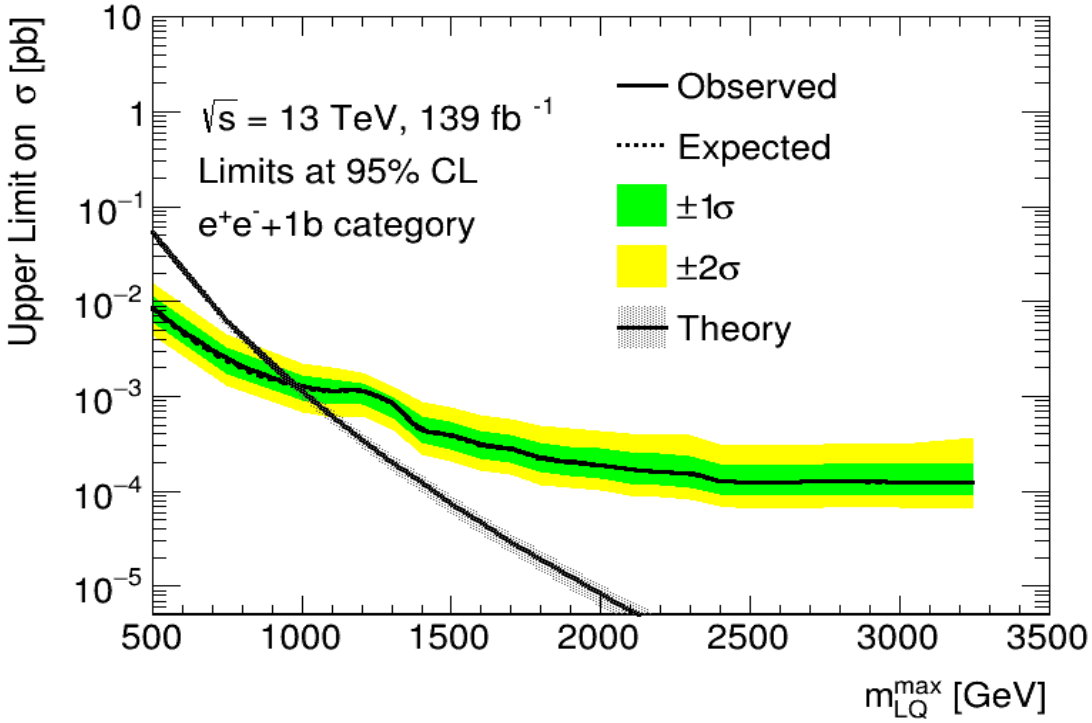


Figure 5.20: *Expected upper limit at 95 % confidence level (CL) on the LQ production cross section for different leptoquark masses. The grey line represent the LQ cross section and the hazed area, the uncertainty at leading order.*

5.8.5 Muon b-veto channel

A summary of the pre-fit and post-fit yields in the signal, control, and validation regions with the expected number of events for the different backgrounds are shown on Figure 5.21. The cut value for each LQ mass that gives the strongest limit and the expected upper limit is shown in Table 5.11. Figure 5.22 show the linear correlations of the nuisance parameters from the background only fit as well as the post-fit normalization of $t\bar{t}$ and Z+jets backgrounds. The overall top background normalization changes by 0.97 $\pm$0.06 while that of Z+jets changes by 1.11 $\pm$ 0.05. The nuisance parameters are correlated from the background-only fit. A strong anti-correlation as expected is seen in the Z+jets normalization and the theory uncertainty, with other correlations being moderate. The impact of the nuisance parameter on the signal strength is evaluated in a similar manner as performed for electron b-veto and electron b-tag regions. The corresponding ranking plots are shown in Figure 5.23. The expected upper limit on the production cross-section multiplied by the branching ratio for all LQ masses together with the model interpretation is shown in Figure 5.24 for this region.

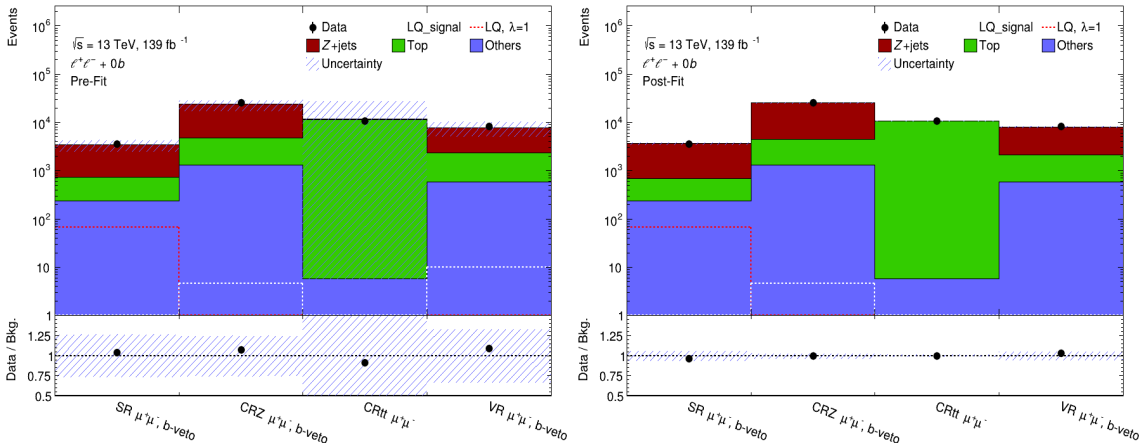
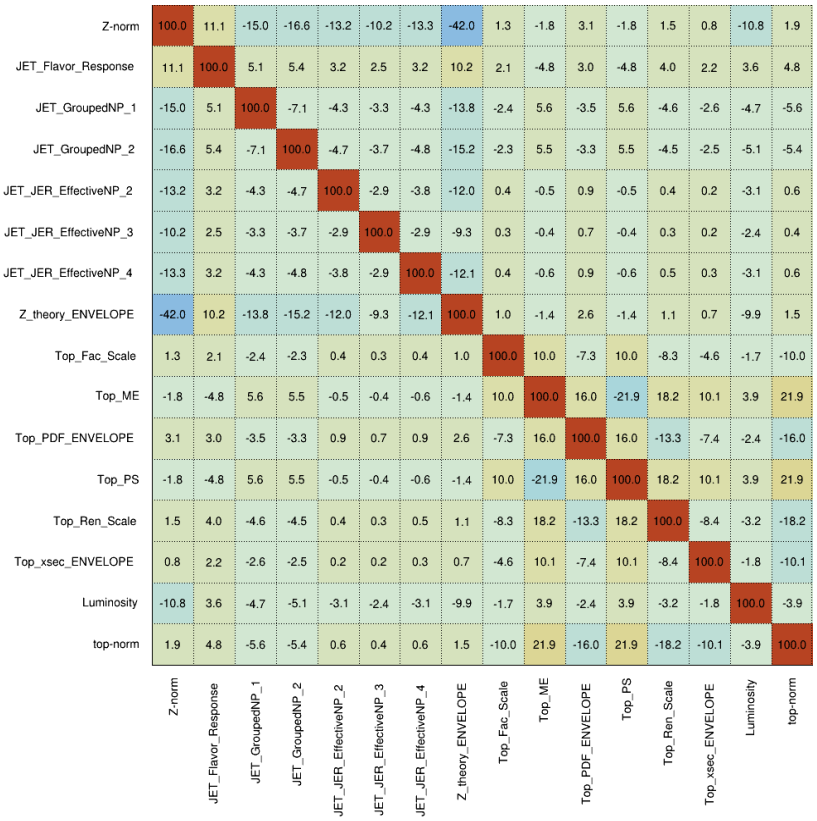


Figure 5.21: *Pre-fit and post-fit event yields in the signal, control and validation regions. The signal considered here is the 1200 GeV LQ mass hypothesis, corresponding to a cut value of 1100 GeV coupling to strange quarks. The Uncertainties are both systematic and statistical uncertainties.*

m_{LQ}[GeV]	m_{LQ}^{max} cut [GeV]	UL [pb]
500	400	2.30731e-02
750	700	5.84044e-03
1000	900	2.84020e-03
1100	900	2.42500e-03
1200	1100	1.94097e-03
1300	1100	1.65101e-03
1400	1400	1.16965e-03
1500	1400	7.51407e-04
1600	1500	5.26905e-04
1700	1500	4.34322e-04
1800	1600	3.70006e-04
1900	1700	3.23935e-04
2000	1700	2.92763e-04
2100	1900	2.58590e-04
2200	2000	2.32554e-04
2300	2000	2.07273e-04
2400	2100	1.93937e-04
2500	2300	1.79857e-04
2750	2300	1.43778e-04
3000	2600	1.21607e-04
3250	2900	9.41073e-05
3500	2900	8.02636e-05

Table 5.11: *A summary of the cut value of the LQ mass with the best upper limit on the signal strength for each LQ mass for b-veto, muon-channel.*



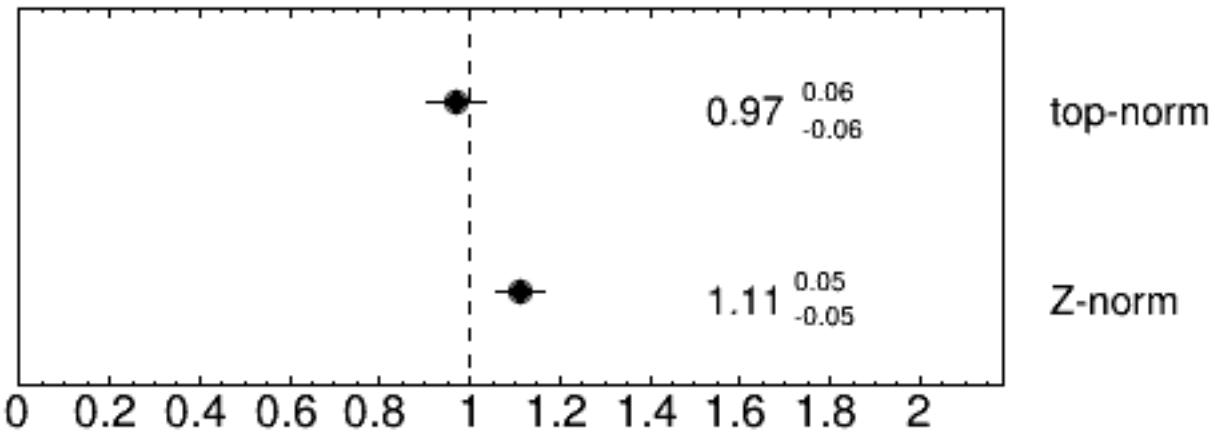


Figure 5.22: *The reduced correlation matrix of the nuisance parameters from the background only fit and the post-fit normalization parameters for b-veto, muon-channel.*

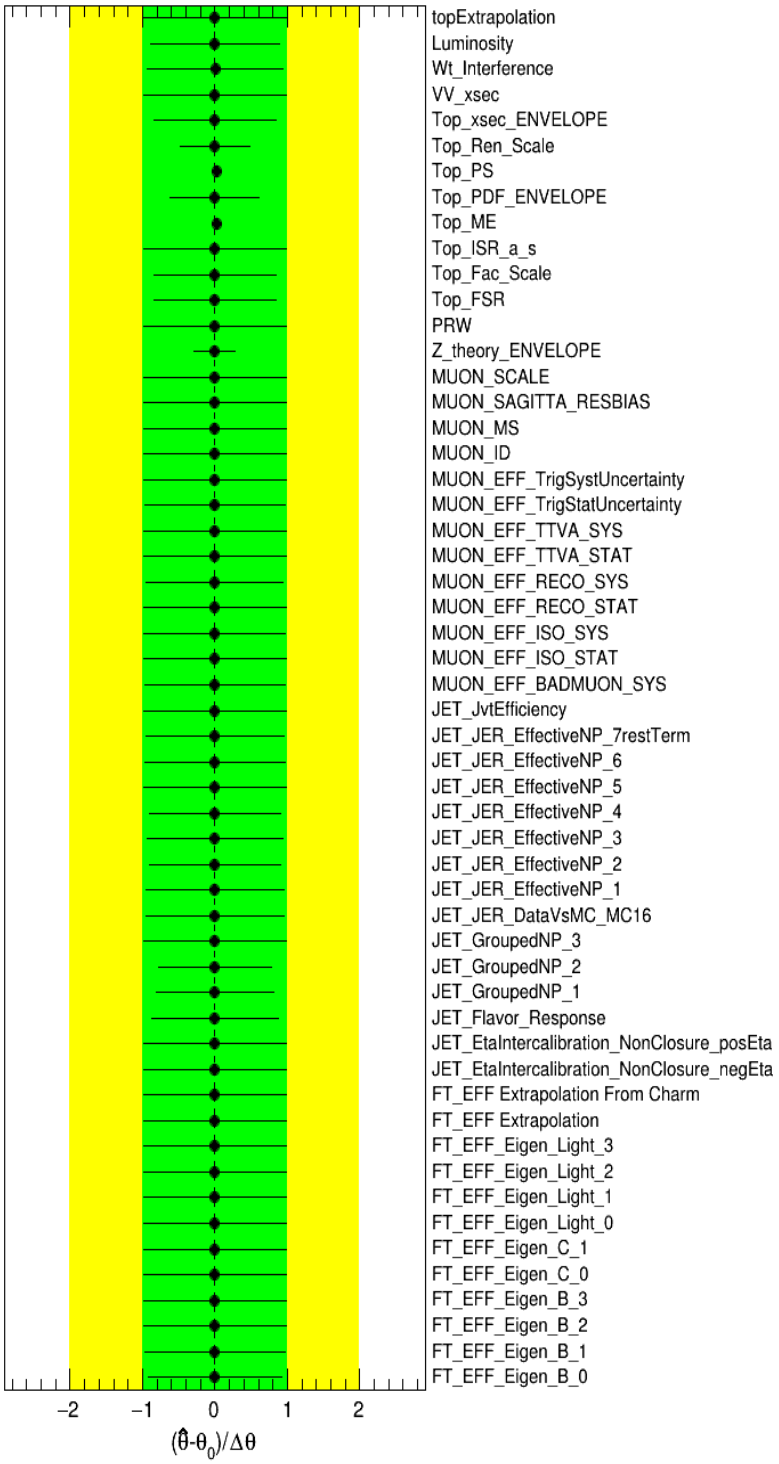


Figure 5.23: *Ranking plot of the nuisance parameters from the impact on the signal strength μ, from the variation of the uncertainty by sigma up and down for b-veto, muon-channel.*

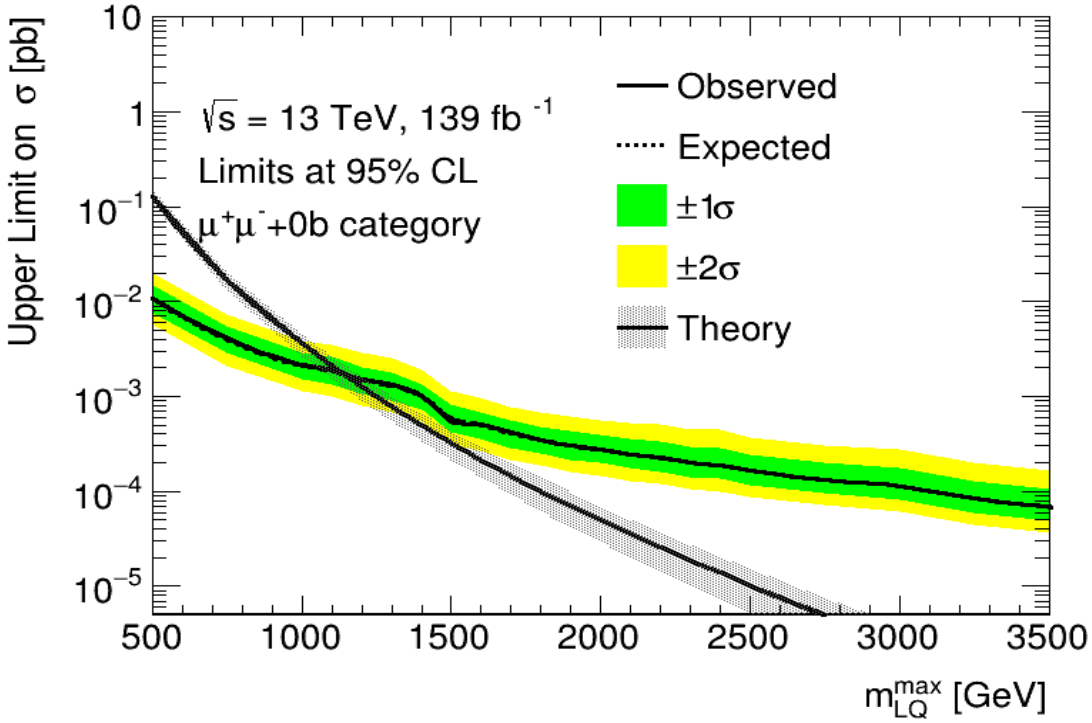


Figure 5.24: *Expected upper limit at 95 % confidence level (CL) on the LQ production cross section for different leptoquark masses. The grey line represent the LQ cross section and the hazed area, the uncertainty at leading order. This is for b-veto, muon-channel.*

5.8.6 Muon b-tag channel

The pre-fit and post-fit yields in the signal, control, and validation regions with the expected number of events for the different backgrounds are summarized in Figure 5.25. The cut value for each LQ mass that gives the strongest limit and the expected upper limit is shown in Table 5.12. The linear correlations of the nuisance parameters from the background only fit as well as the post-fit normalization of $t\bar{t}$ and Z+jets backgrounds is shown on Figure 5.26. The overall top background normalization changes by 0.97 $\pm$0.06 while that of Z+jets changes by 1.11 $\pm$ 0.05. The nuisance parameters are correlated from the background-only fit. A strong anti-correlation as expected is seen in the Z+jets normalization and the theory uncertainty, with other correlations being moderate. The impact of the nuisance parameter on the signal strength is evaluated in a similar manner as performed for electron b-veto and electron b-tag regions. The corresponding ranking plots are shown in Figure 5.27. The expected upper limit on the production cross-section multiplied by the branching ratio for all LQ masses together with the model interpretation is shown in Figure 5.28 for this region.

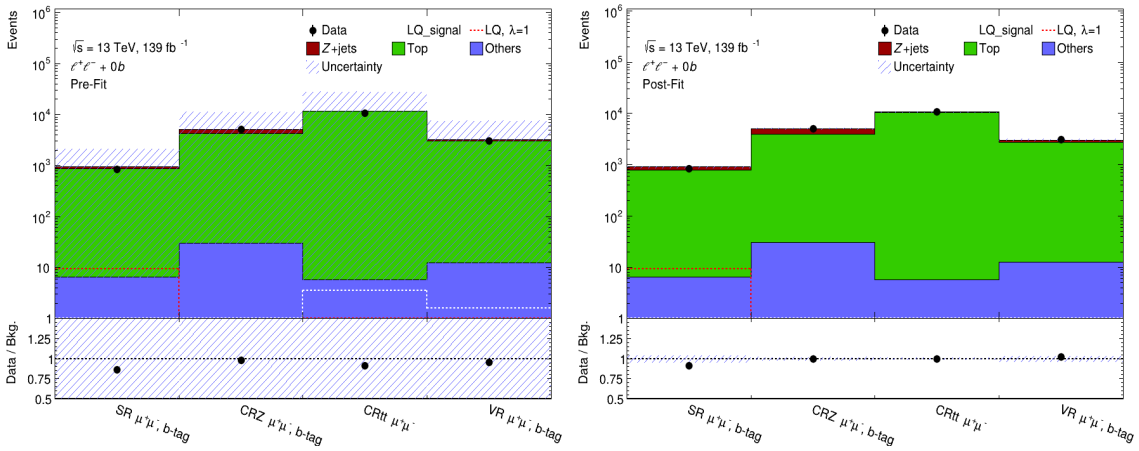
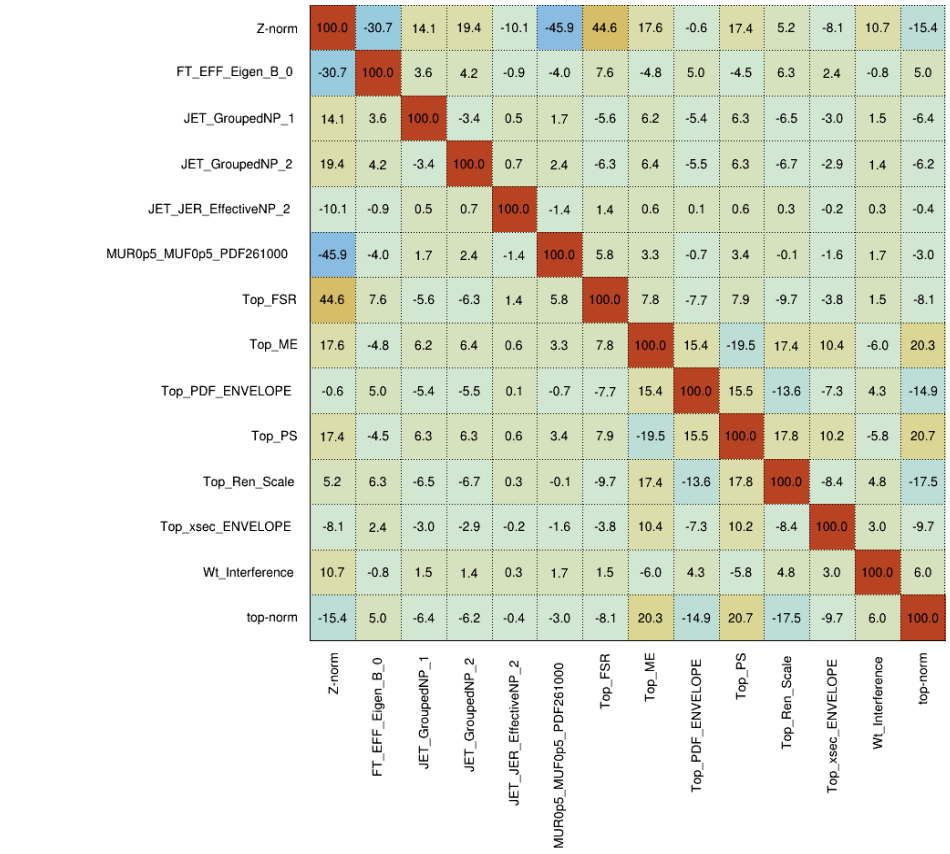


Figure 5.25: *Pre-fit and post-fit event yields in the signal, control and validation regions. The signal considered here is the 1200 GeV LQ mass hypothesis, corresponding to a cut value of 1100 GeV coupling to bottom quarks. The Uncertainties are both systematic and statistical uncertainties.*

m_{LQ}[GeV]	m_{LQ}^{max} cut [GeV]	UL [pb]
500	400	1.15721e-02
750	600	3.67239e-03
1000	900	1.05759e-03
1100	900	8.65415e-04
1200	1100	7.02809e-04
1300	1100	5.51497e-04
1400	1200	4.65028e-04
1500	1300	3.83508e-04
1600	1400	3.37890e-04
1700	1400	2.92378e-04
1800	1500	2.81393e-04
1900	1700	2.60283e-04
2000	1700	2.29415e-04
2100	1700	2.11779e-04
2200	1700	2.08473e-04
2300	1700	2.09118e-04
2400	1700	2.04200e-04
2500	1700	2.00544e-04
2750	2200	2.03431e-04
3000	2300	2.04704e-04
3250	2300	1.97515e-04
3500	2300	2.10280e-04

Table 5.12: *A summary of the cut value of the LQ mass with the best upper limit on the signal strength for each LQ mass for b-tag, muon-channel.*



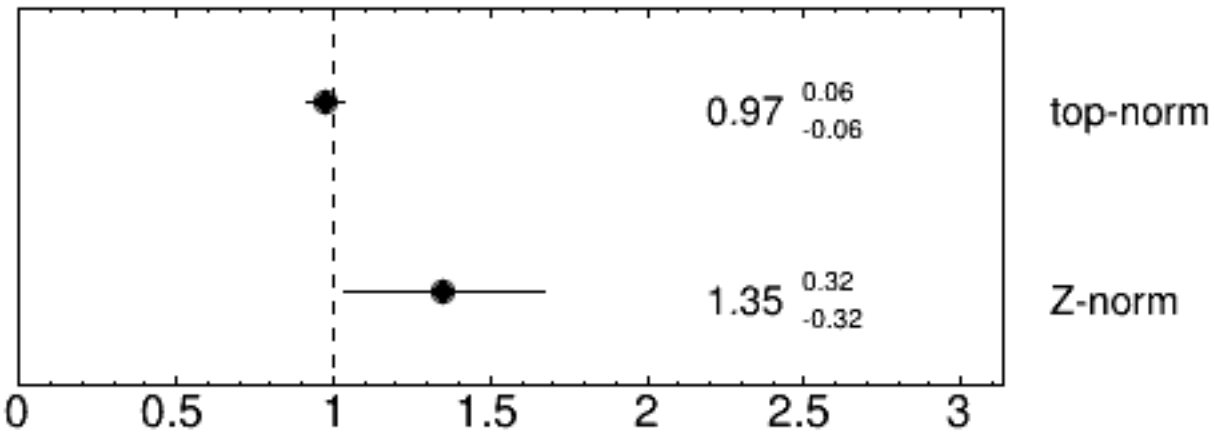


Figure 5.26: *The reduced correlation matrix of the nuisance parameters from the background only fit and the post-fit normalization parameters for b-tag, muon-channel.*

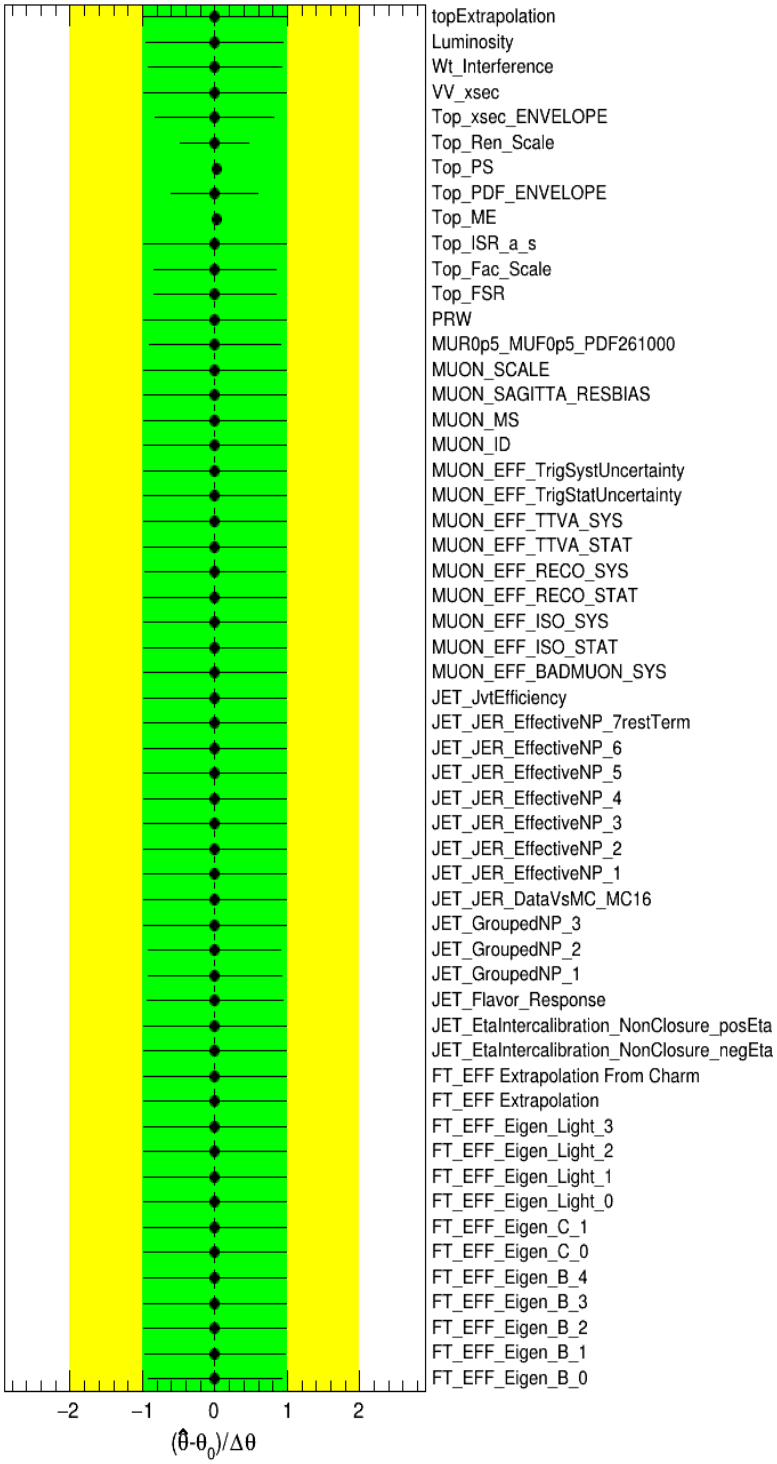


Figure 5.27: *Ranking plot of the nuisance parameters from the impact on the signal strength μ, from the variation of the uncertainty by sigma up and down for b-tag, muon-channel.*

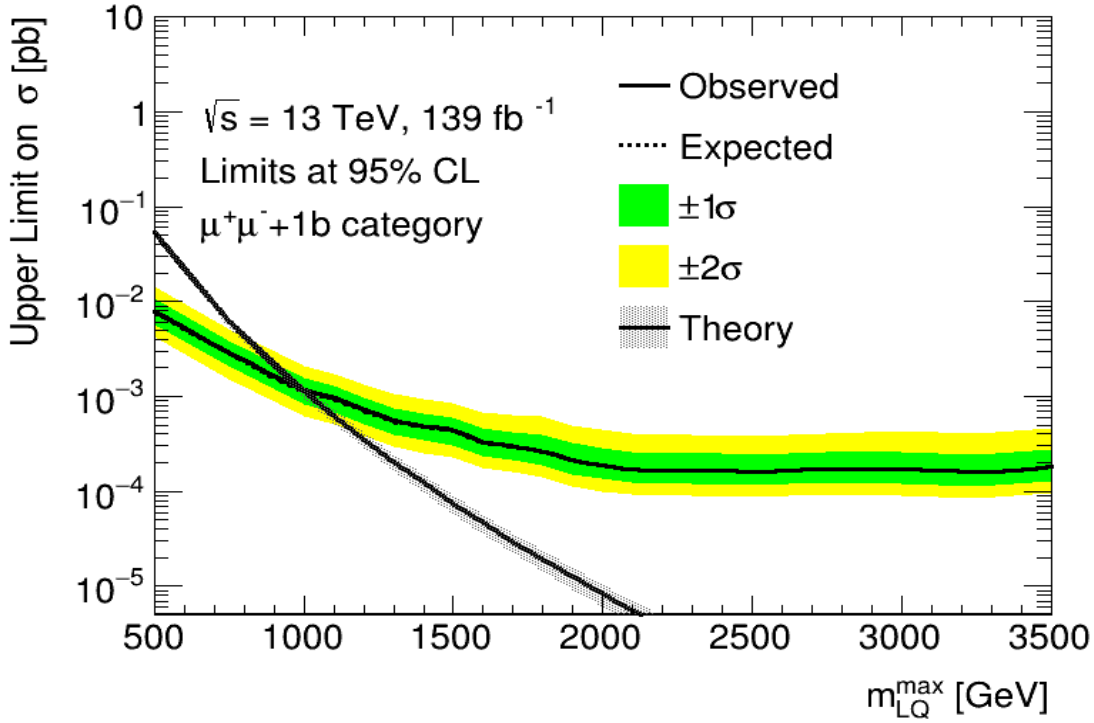


Figure 5.28: *Expected upper limit at 95 % confidence level (CL) on the LQ production cross section for different leptoquark masses. The grey line represent the LQ cross section and the hazed area, the uncertainty at leading order. This is for b-tag, muon-channel.*

5.9 Conclusion

A search for leptoquarks in single production decaying into an electron or muon in association with a light flavor quark or bottom quark was presented using proton-proton collisions of 139 fb^{-1} integrated luminosity recorded by the ATLAS detector. For each of the signal regions (electron b-veto, electron b-tag, muon b-veto, muon b-tag), the model-independent upper limits were set on the signal cross-section at 95 % confidence level. The mass range of the leptoquarks considered is 500 GeV to 3500 GeV. In the electron b-veto channel, the model exclude leptoquarks coupling to strange quarks at masses below 1.1 TeV while for leptoquarks coupling to bottom quarks and electrons, the model excludes the masses below 1.0 TeV. Similarly, for the muon channel, the exclusion is at masses below 1.1 TeV for the leptoquarks coupling to strange quark and 1.0 TeV for the leptoquarks coupling to the bottom quark. No new physics has been observed in this analysis.

6. Summary

This thesis presents two beyond the Standard Model searches: The first is the search for the right-handed gauge boson W_R decaying into a boosted right-handed heavy neutrino N_R and a lepton while the second search is the single leptoquark search with the ATLAS detector. These searches use the full Run 2 ATLAS data set. The first search is aimed at explaining why neutrino masses are very small but non-zero contrary to the Standard Model where the neutrino masses are zero. Only the electron final state is reported in this thesis which makes use of the large-radius jet that contains an electron as our N_R so as to significantly reduce the background contribution. A detailed study to improve the identification of electrons close to jets in the context of this search is also presented. The W_R reconstructed is consistent with background prediction. The partial Run 2 result exclude W_R mass above 4.8 TeV for N_R mass 0.4-0.5 TeV. This full Run 2 search result show a significance of 1.4 σ which is lower than the 2.4 σ obtained using the partial Run 2 data. We do not see any significant deviation to the prediction of the Standard Model. The second search is aimed at explaining the anomalies in the flavour sector and the recent muon g-2 result by searching for leptoquarks in single production decaying into electrons or muons in association with a strange or bottom quark in the final state. For each of the signal regions (electron b-veto, electron b-tag, muon b-veto, muon b-tag), the model-independent upper limits were set on the signal cross-section at 95 % confidence level. The mass range of the leptoquarks considered is 500 GeV to 3500 GeV. In the electron b-veto channel, the model exclude leptoquarks coupling to strange quarks at masses below 1.1 TeV while for leptoquarks coupling to bottom quarks and electrons, the model excludes the masses below 1.0 TeV. Similarly, for the muon channel, the exclusion is at masses below 1.1 TeV for the leptoquarks coupling to strange quark and 1.0 TeV for the leptoquarks coupling to the bottom quark. No signatures of new physics was observed in this analysis.

Bibliography

[1] Peter W. Higgs. "Broken Symmetries and the Masses of Gauge Bosons". In: *Phys. Rev. Lett.* 13 (1964). Ed. by J.C. Taylor, pp. 508–509. DOI: 10.1103/PhysRevLett.13.508.

[2] R. Keith Ellis, W. James Stirling, and B. R. Webber. *QCD and collider physics*. Vol. 8. Cambridge University Press, Feb. 2011. ISBN: 978-0-511-82328-2, 978-0-521-54589-1. URL: https://inspirehep.net/literature/328604.

[3] W. Greiner. "Quantum electrodynamics of strong fields". In: *Lect. Notes Phys.* 231 (1985). Ed. by W. D. Heiss, pp. 95–226. DOI: 10.1007/3-540-15653-4_3.

[4] Makoto Kobayashi and Toshihide Maskawa. "CP Violation in the Renormalizable Theory of Weak Interaction". In: *Prog. Theor. Phys.* 49 (1973), pp. 652–657. DOI: 10.1143/PTP.49.652.

[5] F. Englert and R. Brout. "Broken Symmetry and the Mass of Gauge Vector Mesons". In: *Phys. Rev. Lett.* 13 (1964). Ed. by J. C. Taylor, pp. 321–323. DOI: 10.1103/PhysRevLett.13.321.

[6] Peter W. Higgs. "Broken symmetries, massless particles and gauge fields". In: *Phys. Lett.* 12 (1964), pp. 132–133. DOI: 10.1016/0031-9163(64)91136-9.

[7] W. Cottingham and Derek Greenwood. "An introduction to the standard model of particle physics: Second edition". In: *An introduction to the standard model of particle physics / W. Noel Cottingham, Derek A. Greenwood. 2nd ed. Cambridge : Cambridge University Press, 2007. ISBN: 9780521852494 (cased)* (Jan. 2007). DOI: 10.1017/CBO9780511791406.

[8] Chen-Ning Yang and Robert L. Mills. "Conservation of Isotopic Spin and Isotopic Gauge Invariance". In: *Phys. Rev.* 96 (1954). Ed. by Jong-Ping Hsu and D. Fine, pp. 191–195. DOI: 10.1103/PhysRev.96.191.

[9] Hideki Yukawa. "On the Interaction of Elementary Particles I". In: *Proc. Phys. Math. Soc. Jap.* 17 (1935), pp. 48–57. DOI: 10.1143/PTPS.1.1.

[10] ATLAS Collaboration. "The ATLAS Experiment at the CERN Large Hadron Collider". In: *JINST* 3 (2008), S08003. DOI: 10.1088/1748-0221/3/08/S08003.

[11] N. Cabibbo and R. Gatto. "Consequences of unitary symmetry for weak and electromagnetic transitions". In: *Nuovo Cim.* 21 (1961), pp. 872–877. DOI: 10.1007/BF02785616.

[12] Nicola Cabibbo. "Unitary Symmetry and Leptonic Decays". In: *Phys. Rev. Lett.* 10 (1963), pp. 531–533. DOI: 10.1103/PhysRevLett.10.531.

[13] ATLAS Collaboration. "Measurement of angular correlations in Drell-Yan lepton pairs to probe Z/gamma* boson transverse momentum at sqrt(s)=7 TeV with the ATLAS detector". In: *Phys. Lett.* B720 (2013), pp. 32–51. DOI: 10.1016/j.physletb.2013.01.054. arXiv: 1211.6899 [hep-ex].

[14] ATLAS Collaboration. "Measurement of ZZ production in pp collisions at $\sqrt{s} = 7$ TeV and limits on anomalous ZZZ and $ZZ\gamma$ couplings with the ATLAS detector". In: *JHEP* 03 (2013), p. 128. DOI: 10.1007/JHEP03(2013)128. arXiv: 1211.6096 [hep-ex].

[15] ATLAS Collaboration. "Measurement of the production of a W boson in association with a charm quark in pp collisions at $\sqrt{s} = 7$ TeV with the ATLAS

detector". In: *JHEP* 05 (2014), p. 068. DOI: 10.1007/JHEP05(2014)068. arXiv: 1402.6263 [hep-ex].

[16] CMS Collaboration. "The CMS experiment at the CERN LHC". In: *Journal of Instru-mentation* 3 (2008), S08004–S08004. DOI: 10.1088/1748-0221/3/08/s08004. URL: https://doi.org/10.1088%2F1748-0221%2F3%2F08%2Fs08004.

[17] LHCb Collaboration. "The LHCb Detector at the LHC". In: *JINST* 3 (2008), S08005. DOI: 10.1088/1748-0221/3/08/S08005.

[18] ALICE Collaboration. "The ALICE experiment at the CERN LHC". In: *JINST* 3 (2008), S08002. DOI: 10.1088/1748-0221/3/08/S08002.

[19] Esma Mobs. "The CERN accelerator complex - 2019. Complexe des accelerateurs du CERN - 2019". In: (2019). General Photo. URL: https://cds.cern.ch/record/2684277.

[20] Stephen Myers. "The LEP collider, from design to approval and commissioning". In: (Oct. 1991). DOI: 10.5170/CERN-1991-008.

[21] ATLAS Collaboration. *Online luminosity public results Run 2*. URL: https://twiki.cern.ch/twiki/bin/view/AtlasPublic/LuminosityPublicResultsRun2.

[22] ATLAS Collaboration. "ATLAS Insertable B-Layer Technical Design Report Addendum". In: (May 2012). URL: https://inspirehep.net/literature/1609509.

[23] ATLAS Collaboration. "Production and Integration of the ATLAS Insertable B-Layer". In: *JINST* 13.05 (2018), T05008. DOI: 10.1088/1748-0221/13/05/T05008. arXiv: 1803.00844 [physics.ins-det].

[24] Matthias Schott and Monica Dunford. "Review of single vector boson production in pp collisions at $\sqrt{s} = 7$ TeV". In: *Eur. Phys. J. C* 74 (2014), p. 2916. DOI: 10.1140/epjc/s10052-014-2916-1. arXiv: 1405.1160 [hep-ex].

[25] ATLAS Collaboration. "The ATLAS Inner Detector commissioning and calibration". In: *Eur. Phys. J. C* 70 (2010), pp. 787–821. DOI: 10.1140/epjc/s10052-010-1366-7. arXiv: 1004.5293 [physics.ins-det].

[26] ATLAS Collaboration. "ATLAS inner detector: Technical design report. Vol. 2". In: (1997). URL: https://inspirehep.net/literature/455673.

[27] ATLAS Collaboration. "ATLAS pixel detector: Technical design report". In: (May 1998). URL: https://inspirehep.net/literature/487239.

[28] Karolos Potamianos. "The upgraded Pixel detector and the commissioning of the Inner Detector tracking of the ATLAS experiment for Run-2 at the Large Hadron Collider". In: (). arXiv: 1608.07850.

[29] F. Bauer et al. "Construction and Test of MDT Chambers for the ATLAS Muon Spectrometer". In: *Nucl. Instrum. Meth. A* (). Ed. by G. Batignani et al., pp. 17–20. DOI: 10.1016/S0168-9002(00)01156-6. arXiv: 1604.02000.

[30] Theodoros Argyropoulos et al. "Cathode strip chambers in ATLAS: Installation, commissioning and in situ performance". In: *IEEE Trans. Nucl. Sci.* 56 (2009), pp. 1568–1574. DOI: 10.1109/TNS.2009.2020861.

[31] ATLAS Collaboration. "Performance of the ATLAS muon triggers in Run 2". In: (Apr. 2020). arXiv: 2004.13447 [hep-ex].

[32] G. Aielli et al. "The RPC first level muon trigger in the barrel of the ATLAS experiment". In: *Nucl. Phys. B Proc. Suppl.* 158 (2006). Ed. by S.K. Park, S.P. Ratti, and R. Santonico, pp. 11–15. DOI: 10.1016/j.nuclphysbps.2006.07.031.

[33] S. Majewski et al. "A THIN MULTIWIRE CHAMBER OPERATING IN THE HIGH MULTIPLICATION MODE". In: *Nucl. Instrum. Meth.* 217 (1983), pp. 265–271. DOI: 10.1016/0167-5087(83)90146-1.

[34] Zoltan Nagy and Davison E. Soper. "What is a parton shower?" In: *Phys. Rev. D* 98.1 (2018), p. 014034. DOI: 10.1103/PhysRevD.98.014034. arXiv: 1705.08093 [hep-ph].

[35] Stefan Höche. "Introduction to parton-shower event generators". In: *Theoretical Advanced Study Institute in Elementary Particle Physics: Journeys Through the Precision Frontier: Amplitudes for Colliders*. 2015, pp. 235–295. DOI: 10.1142/9789814678766_0005. arXiv: 1411.4085 [hep-ph].

[36] John C. Collins. "Sudakov form-factors". In: *Adv. Ser. Direct. High Energy Phys.* 5 (1989), pp. 573–614. DOI: 10.1142/9789814503266_0006. arXiv: hep-ph/0312336.

[37] Dokshitzer Y. L. Khoze V. A. Trovan S. I. Azimov Ya. I. "Similarity of parton and hadron spectra in QCD jets". In: *Zeitschrift für Physik C Particles and Fields*. 1431-5858 27 (1985). DOI: 10.1007/BF01642482. URL: https://doi.org/10.1007/BF01642482.

[38] Deepak Kar. *Experimental Particle Physics*. 2053-2563. IOP Publishing, 2019. ISBN: 978-0-7503-2112-9. DOI: 10.1088/2053-2563/ab1be6. URL: http://dx.doi.org/10.1088/2053-2563/ab1be6.

[39] ATLAS Collaboration. "Performance of the ATLAS Trigger System in 2015". In: *Eur. Phys. J. C* 77.5 (2017), p. 317. DOI: 10.1140/epjc/s10052-017-4852-3. arXiv: 1611.09661 [hep-ex].

[40] Catrin Bernius. *HL-LHC prospects from ATLAS and CMS*. Tech. rep. ATL-PHYS-PROC-2019-023. Geneva: CERN, 2019. URL: https://cds.cern.ch/record/2666331.

[41] ATLAS Collaboration. "The performance of the jet trigger for the ATLAS detector during 2011 data taking". In: *Eur. Phys. J. C* 76.10 (2016), p. 526. DOI: 10.1140/epjc/s10052-016-4325-0. arXiv: 1606.07759 [hep-ex].

[42] ATLAS Collaboration. "Electron reconstruction and identification in the ATLAS experiment using the 2015 and 2016 LHC proton-proton collision data at $\sqrt{s}$ = 13 TeV". In: *Eur. Phys. J. C* 79.8 (2019), p. 639. DOI: 10.1140/epjc/s10052-019-7140-6. arXiv: 1902.04655 [physics.ins-det].

[43] W. Lampl et al. "Calorimeter clustering algorithms: Description and performance". In: (May 2008).

[44] ATLAS Collaboration. "Electron reconstruction and identification in the ATLAS experiment using the 2015 and 2016 LHC proton-proton collision data at $\sqrt{s}$ = 13 TeV". In: *Eur. Phys. J. C* 79.8 (2019), p. 639. DOI: 10.1140/epjc/s10052-019-7140-6. arXiv: 1902.04655 [physics.ins-det].

[45] ATLAS Collaboration. "dE/dx measurement in the ATLAS Pixel Detector and its use for particle identification". In: (Mar. 2011). URL: https://inspirehep.net/literature/1204066.

[46] ATLAS Collaboration. "Electron efficiency measurements with the ATLAS detector using the 2012 LHC proton-proton collision data". In: (June 2014). URL: https://inspirehep.net/literature/1299450.

[47] Thijs G. Cornelissen et al. "The global χ^2 track fitter in ATLAS". In: *J. Phys. Conf. Ser.* 119 (2008), p. 032013. DOI: 10.1088/1742-6596/119/3/032013.

[48] ATLAS Collaboration. "Improved electron reconstruction in ATLAS using the Gaussian Sum Filter-based model for bremsstrahlung". In: (May 2012). URL: https://inspirehep.net/literature/1204271.

[49] ATLAS Collaboration. "Electron efficiency measurements with the ATLAS detector using 2012 LHC proton–proton collision data". In: *Eur. Phys. J. C* 77.3 (2017), p. 195. DOI: 10.1140/epjc/s10052-017-4756-2. arXiv: 1612.01456 [hep-ex].

[50] ATLAS Collaboration. "Topological cell clustering in the ATLAS calorimeters and its performance in LHC Run 1". In: *Eur. Phys. J. C* 77 (2017), p. 490. DOI: 10.1140/epjc/s10052-017-5004-5. arXiv: 1603.02934 [hep-ex].

[51] ATLAS Collaboration. "ATLAS Jet Reconstruction, Calibration, and Tagging of Lorentz-boosted Objects". In: *EPJ Web Conf.* 182 (2018). Ed. by Y. Aharonov, L. Bravina, and S. Kabana, p. 02113. DOI: 10.1051/epjconf/201818202113.

[52] ATLAS Collaboration. "Jet reconstruction and performance using particle flow with the ATLAS Detector". In: *Eur. Phys. J. C* 77.7 (2017), p. 466. DOI: 10.1140/epjc/s10052-017-5031-2. arXiv: 1703.10485 [hep-ex].

[53] Matteo Cacciari, Gavin P. Salam, and Gregory Soyez. "The anti-k_t jet clustering algorithm". In: *JHEP* 04 (2008), p. 063. DOI: 10.1088/1126-6708/2008/04/063. arXiv: 0802.1189 [hep-ph].

[54] Steven Weinberg. "Baryon- and Lepton-Nonconserving Processes". In: *Phys. Rev. Lett.* 43 (21 1979), pp. 1566–1570. DOI: 10.1103/PhysRevLett.43.1566. URL: https://link.aps.org/doi/10.1103/PhysRevLett.43.1566.

[55] Peter Minkowski. "$\mu \to e\gamma$ at a Rate of One Out of 10^9 Muon Decays?" In: *Phys. Lett. B* 67 (1977), pp. 421–428. DOI: 10.1016/0370-2693(77)90435-X.

[56] Tsutomu Yanagida. "Horizontal gauge symmetry and masses of neutrinos". In: *Conf. Proc. C* 7902131 (1979). Ed. by Osamu Sawada and Akio Sugamoto, pp. 95–99.

[57] Murray Gell-Mann, Pierre Ramond, and Richard Slansky. "Complex Spinors and Unified Theories". In: (2013). arXiv: 1306.4669 [hep-th].

[58] M. Magg and Ch. Wetterich. "Neutrino mass problem and gauge hierarchy". In: *Physics Letters B* 94.1 (1980), pp. 61 –64. ISSN: 0370-2693. DOI: https://doi.org/10.1016/0370-2693(80)90825-4. URL: http://www.sciencedirect.com/science/article/pii/0370269380908254.

[59] T. P. Cheng and Ling-Fong Li. "Neutrino masses, mixings, and oscillations in SU(2)U(1) models of electroweak interactions". In: *Phys. Rev. D* 22 (11 1980), pp. 2860–2868. DOI: 10.1103/PhysRevD.22.2860. URL: https://link.aps.org/doi/10.1103/PhysRevD.22.2860.

[60] Rabindra N. Mohapatra, familyi=c., given=Goran, giveni=G., „ and. "Neutrino masses and mixings in gauge models with spontaneous parity violation". In: *Phys. Rev. D* 23 (1 1981), pp. 165–180. DOI: 10.1103/PhysRevD.23.165. URL: https://link.aps.org/doi/10.1103/PhysRevD.23.165.

[61] Robert Foot et al. "Seesaw Neutrino Masses Induced by a Triplet of Leptons". In: *Z. Phys. C* 44 (1989), p. 441. DOI: 10.1007/BF01415558.

[62] Jogesh C. Pati and Abdus Salam. "Lepton number as the fourth "color"". In: *Phys. Rev. D* 10 (1 1974), pp. 275–289. DOI: 10.1103/PhysRevD.10.275. URL: https://link.aps.org/doi/10.1103/PhysRevD.10.275.

[63] R. N. Mohapatra and J. C. Pati. “"Natural" left-right symmetry”. In: *Phys. Rev. D* 11 (9 1975), pp. 2558–2561. DOI: 10.1103/PhysRevD.11.2558. URL: https://link.aps.org/doi/10.1103/PhysRevD.11.2558.

[64] G. Senjanovic and R. N. Mohapatra. “Exact left-right symmetry and spontaneous violation of parity”. In: *Phys. Rev. D* 12 (5 1975), pp. 1502–1505. DOI: 10.1103/PhysRevD.12.1502. URL: https://link.aps.org/doi/10.1103/PhysRevD.12.1502.

[65] ATLAS Collaboration. “Search for heavy Majorana neutrinos with the ATLAS detector in pp collisions at $\sqrt{s} = 8$ TeV”. In: *Journal of High Energy Physics* 2015.7 (2015). ISSN: 1029-8479. DOI: 10.1007/jhep07(2015)162. URL: http://dx.doi.org/10.1007/JHEP07(2015)162.

[66] ATLAS Collaboration. “Search for heavy Majorana or Dirac neutrinos and right-handed W gauge bosons in final states with two charged leptons and two jets at $\sqrt{s} = 8$ TeV with the ATLAS detector”. In: *Journal of High Energy Physics* 2019.1 (2019). ISSN: 1029-8479. DOI: 10.1007/jhep01(2019)016. URL: http://dx.doi.org/10.1007/JHEP01(2019)016.

[67] ATLAS Collaboration. “Search for a right-handed gauge boson decaying into a high-momentum heavy neutrino and a charged lepton in pp collisions with the ATLAS detector at $\sqrt{s} = 13$ TeV”. In: *Phys. Lett. B* 798 (2019), p. 134942. DOI: 10.1016/j.physletb.2019.134942. arXiv: 1904.12679 [hep-ex].

[68] CMS Collaboration. “Search for heavy neutrinos and W bosons with right-handed couplings in proton–proton collisions at $\sqrt{s} = 8$ TeV”. In: *The European Physical Journal C* 74.11 (2014). ISSN: 1434-6052. DOI: 10.1140/epjc/s10052-014-3149-z. URL: http://dx.doi.org/10.1140/epjc/s10052-014-3149-z.

[69] CMS Collaboration. “Search for heavy neutrinos or third-generation leptoquarks in final states with two hadronically decaying leptons and two jets in proton-proton collisions at $\sqrt{s} = 13$ TeV”. In: *Journal of High Energy Physics* 2017.3 (2017). ISSN: 1029-8479. DOI: 10.1007/jhep03(2017)077. URL: http://dx.doi.org/10.1007/JHEP03(2017)077.

[70] CMS Collaboration. “Search for a heavy right-handed W boson and a heavy neutrino in events with two same-flavor leptons and two jets at $\sqrt{s} = 13$ TeV”. In: *Journal of High Energy Physics* 2018.5 (2018). ISSN: 1029-8479. DOI: 10.1007/jhep05(2018)148. URL: http://dx.doi.org/10.1007/JHEP05(2018)148.

[71] CMS Collaboration. “Search for heavy Majorana neutrinos in same-sign dilepton channels in proton-proton collisions at $\sqrt{s} = 13$ TeV”. In: *Journal of High Energy Physics* 2019.1 (2019). ISSN: 1029-8479. DOI: 10.1007/jhep01(2019)122. URL: http://dx.doi.org/10.1007/JHEP01(2019)122.

[72] ATLAS Collaboration. “Search for new resonances in mass distributions of jet pairs using 139 fb^{-1} of pp collisions at $\sqrt{s} = 13$ TeV with the ATLAS detector”. In: *JHEP* 03 (2020), p. 145. DOI: 10.1007/JHEP03(2020)145. arXiv: 1910.08447 [hep-ex].

[73] ATLAS Collaboration. “Search for heavy Majorana or Dirac neutrinos and right-handed W gauge bosons in final states with two charged leptons and two jets at $\sqrt{s} = 13$ TeV with the ATLAS detector”. In: *JHEP* 01 (2019), p. 016. DOI: 10.1007/JHEP01(2019)016. arXiv: 1809.11105 [hep-ex].

[74] P. Duka, J. Gluza, and M. Zralek. "Quantization and renormalization of the manifest left-right symmetric model of electroweak interactions". In: *Annals Phys.* 280 (2000), pp. 336–408. DOI: 10.1006/aphy.1999.5988. arXiv: hep-ph/9910279.

[75] Wai-Yee Keung and Goran Senjanovic. "Majorana Neutrinos and the Production of the Right-Handed Charged Gauge Boson". In: *Phys. Rev. Lett.* 50 (19 1983), pp. 1427–1430. DOI: 10.1103/PhysRevLett.50.1427. URL: https://link.aps.org/doi/10.1103/PhysRevLett.50.1427.

[76] Manimala Mitra et al. "Neutrino jets from high-mass WR gauge bosons in TeV-scale left-right symmetric models". In: *Physical Review D* 94.9 (2016). ISSN: 2470-0029. DOI: 10.1103/physrevd.94.095016. URL: http://dx.doi.org/10.1103/PhysRevD.94.095016.

[77] A. G. Dias et al. "Simple realization of the inverse seesaw mechanism". In: *Physical Review D* 86.3 (2012). ISSN: 1550-2368. DOI: 10.1103/physrevd.86.035007. URL: http://dx.doi.org/10.1103/PhysRevD.86.035007.

[78] R. Barbier et al. "R-Parity-violating supersymmetry". In: *Physics Reports* 420.1-6 (2005), 1–195. ISSN: 0370-1573. DOI: 10.1016/j.physrep.2005.08.006. URL: http://dx.doi.org/10.1016/j.physrep.2005.08.006.

[79] ATLAS Collaboration. "Search for new phenomena in a lepton plus high jet multiplicity final state with the ATLAS experiment using $\sqrt{s} = 13$ TeV proton-proton collision data". In: *Journal of High Energy Physics* 2017.9 (2017). ISSN: 1029-8479. DOI: 10.1007/jhep09(2017)088. URL: http://dx.doi.org/10.1007/JHEP09(2017)088.

[80] ATLAS Collaboration. "Search for a right-handed gauge boson decaying into a high-momentum heavy neutrino and a charged lepton in pp collisions with the ATLAS detector at $\sqrt{s} = 13$ TeV". In: *Phys. Lett. B* 798 (2019), p. 134942. DOI: 10.1016/j.physletb.2019.134942. arXiv: 1904.12679 [hep-ex].

[81] J. Alwall et al. "The automated computation of tree-level and next-to-leading order differential cross sections, and their matching to parton shower simulations". In: *JHEP* 07 (2014), p. 079. DOI: 10.1007/JHEP07(2014)079. arXiv: 1405.0301 [hep-ph].

[82] Torbjörn Sjöstrand et al. "An introduction to PYTHIA 8.2". In: *Comput. Phys. Commun.* 191 (2015), pp. 159–177. DOI: 10.1016/j.cpc.2015.01.024. arXiv: 1410.3012 [hep-ph].

[83] Richard D. Ball et al. "Parton distributions for the LHC Run II". In: *JHEP* 04 (2015), p. 040. DOI: 10.1007/JHEP04(2015)040. arXiv: 1410.8849 [hep-ph].

[84] ATLAS Collaboration. "ATLAS Pythia 8 tunes to 7 TeV data". In: (Nov. 2014).

[85] Michal Czakon and Alexander Mitov. "Top++: A Program for the Calculation of the Top-Pair Cross-Section at Hadron Colliders". In: *Comput. Phys. Commun.* 185 (2014), p. 2930. DOI: 10.1016/j.cpc.2014.06.021. arXiv: 1112.5675 [hep-ph].

[86] ATLAS Collaboration. "Studies on top-quark Monte Carlo modelling for Top2016". In: (Oct. 2016).

[87] Nikolaos Kidonakis. "Next-to-next-to-leading-order collinear and soft gluon corrections for t-channel single top quark production". In: *Phys. Rev. D* 83 (2011), p. 091503. DOI: 10.1103/PhysRevD.83.091503. arXiv: 1103.2792 [hep-ph].

[88] Nikolaos Kidonakis. "Two-loop soft anomalous dimensions for single top quark associated production with a W- or H-". In: *Phys. Rev. D* 82 (2010), p. 054018. DOI: 10.1103/PhysRevD.82.054018. arXiv: 1005.4451 [hep-ph].

[89] Nikolaos Kidonakis. "NNLL resummation for s-channel single top quark production". In: *Phys. Rev. D* 81 (2010), p. 054028. DOI: 10.1103/PhysRevD.81.054028. arXiv: 1001.5034 [hep-ph].

[90] Charalampos Anastasiou et al. "High precision QCD at hadron colliders: Electroweak gauge boson rapidity distributions at NNLO". In: *Phys. Rev. D* 69 (2004), p. 094008. DOI: 10.1103/PhysRevD.69.094008. arXiv: hep-ph/0312266.

[91] Paolo Nason. "A New method for combining NLO QCD with shower Monte Carlo algorithms". In: *JHEP* 11 (2004), p. 040. DOI: 10.1088/1126-6708/2004/11/040. arXiv: hep-ph/0409146.

[92] Stefano Frixione, Paolo Nason, and Giovanni Ridolfi. "A Positive-weight next-to-leading-order Monte Carlo for heavy flavour hadroproduction". In: *JHEP* 09 (2007), p. 126. DOI: 10.1088/1126-6708/2007/09/126. arXiv: 0707.3088 [hep-ph].

[93] Stefano Frixione, Paolo Nason, and Carlo Oleari. "Matching NLO QCD computations with Parton Shower simulations: the POWHEG method". In: *JHEP* 11 (2007), p. 070. DOI: 10.1088/1126-6708/2007/11/070. arXiv: 0709.2092 [hep-ph].

[94] Simone Alioli et al. "A general framework for implementing NLO calculations in shower Monte Carlo programs: the POWHEG BOX". In: *JHEP* 06 (2010), p. 043. DOI: 10.1007/JHEP06(2010)043. arXiv: 1002.2581 [hep-ph].

[95] T. Gleisberg et al. "Event generation with SHERPA 1.1". In: *JHEP* 02 (2009), p. 007. DOI: 10.1088/1126-6708/2009/02/007. arXiv: 0811.4622 [hep-ph].

[96] Richard D. Ball et al. "Parton distributions with LHC data". In: *Nucl. Phys. B* 867 (2013), pp. 244–289. DOI: 10.1016/j.nuclphysb.2012.10.003. arXiv: 1207.1303 [hep-ph].

[97] ATLAS Collaboration. "The ATLAS Simulation Infrastructure". In: *Eur. Phys. J. C* 70 (2010), pp. 823–874. DOI: 10.1140/epjc/s10052-010-1429-9. arXiv: 1005.4568 [physics.ins-det].

[98] GEANT4 Collaboration. "GEANT4–a simulation toolkit". In: *Nucl. Instrum. Meth. A* 506 (2003), pp. 250–303. DOI: 10.1016/S0168-9002(03)01368-8.

[99] ATLAS Collaboration. "Further ATLAS tunes of PYTHIA6 and Pythia 8". In: (Nov. 2011).

[100] G. Watt and R.S. Thorne. "Study of Monte Carlo approach to experimental uncertainty propagation with MSTW 2008 PDFs". In: *JHEP* 08 (2012), p. 052. DOI: 10.1007/JHEP08(2012)052. arXiv: 1205.4024 [hep-ph].

[101] ATLAS Collaboration. "Electron efficiency measurements with the ATLAS detector using the 2015 LHC proton-proton collision data". In: (June 2016). Ed. by Etienne Augé, Jacques Dumarchez, and Jean Tran Thanh Van.

[102] ATLAS Collaboration. "Electron and photon performance measurements with the ATLAS detector using the 2015–2017 LHC proton-proton collision data". In: *JINST* 14.12 (2019), P12006. DOI: 10.1088/1748-0221/14/12/P12006. arXiv: 1908.00005 [hep-ex].

[103] ATLAS Collaboration. "Jet energy scale measurements and their systematic uncertainties in proton-proton collisions at $\sqrt{s} = 13$ TeV with the ATLAS detector". In: *Phys. Rev. D* 96.7 (2017), p. 072002. DOI: 10.1103/PhysRevD.96.072002. arXiv: 1703.09665 [hep-ex].

[104] David Krohn, Jesse Thaler, and Lian-Tao Wang. "Jet Trimming". In: *JHEP* 02 (2010), p. 084. DOI: 10.1007/JHEP02(2010)084. arXiv: 0912.1342 [hep-ph].

[105] S. Catani et al. "Longitudinally invariant K_t clustering algorithms for hadron hadron collisions". In: *Nucl. Phys. B* 406 (1993), pp. 187–224. DOI: 10.1016/0550-3213(93)90166-M.

[106] ATLAS Collaboration. "Jet mass reconstruction with the ATLAS Detector in early Run 2 data". In: (July 2016).

[107] ATLAS Collaboration. "Search for heavy Majorana or Dirac neutrinos and right-handed W gauge bosons in final states with two charged leptons and two jets at $\sqrt{s} = 13$ TeV with the ATLAS detector". In: *JHEP* 01 (2019), p. 016. DOI: 10.1007/JHEP01(2019)016. arXiv: 1809.11105 [hep-ex].

[108] ATLAS Collaboration. "Search for new phenomena in a lepton plus high jet multiplicity final state with the ATLAS experiment using sqrt(s) = 13 TeV proton–proton collision data". In: (Mar. 2017). Ed. by Etienne Auge, Jacques Dumarchez, and Jean Tran Thanh Van.

[109] ATLAS Collaboration. "Electron reconstruction and identification efficiency measurements with the ATLAS detector using the 2011 LHC proton-proton collision data". In: *Eur. Phys. J.* C74.7 (2014), p. 2941. DOI: 10.1140/epjc/s10052-014-2941-0. arXiv: 1404.2240 [hep-ex].

[110] ATLAS Collaboration. "Electron performance measurements with the ATLAS detector using the 2010 LHC proton-proton collision data". In: *Eur. Phys. J. C* 72 (2012), p. 1909. DOI: 10.1140/epjc/s10052-012-1909-1. arXiv: 1110.3174 [hep-ex].

[111] ATLAS Collaboration. "Electron efficiency measurements with the ATLAS detector using 2012 LHC proton–proton collision data". In: *Eur. Phys. J. C* 77.3 (2017), p. 195. DOI: 10.1140/epjc/s10052-017-4756-2. arXiv: 1612.01456 [hep-ex].

[112] ATLAS Collaboration. "Luminosity determination in pp collisions at $\sqrt{s} = 13$ TeV using the ATLAS detector at the LHC". In: (June 2019).

[113] ATLAS Collaboration. "Luminosity determination in pp collisions at $\sqrt{s} = 8$ TeV using the ATLAS detector at the LHC". In: *Eur. Phys. J. C* 76.12 (2016), p. 653. DOI: 10.1140/epjc/s10052-016-4466-1. arXiv: 1608.03953 [hep-ex].

[114] G. Avoni et al. "The new LUCID-2 detector for luminosity measurement and monitoring in ATLAS". In: *Journal of Instrumentation* 13.07 (2018), P07017–P07017. DOI: 10.1088/1748-0221/13/07/p07017. URL: https://doi.org/10.1088/1748-0221/13/07/p07017.

[115] ATLAS Collaboration. "In situ calibration of large-radius jet energy and mass in 13 TeV proton–proton collisions with the ATLAS detector". In: *Eur. Phys. J. C* 79.2 (2019), p. 135. DOI: 10.1140/epjc/s10052-019-6632-8. arXiv: 1807.09477 [hep-ex].

[116] ATLAS Collaboration. "Search for new phenomena in dijet events using 37 fb^{-1} of pp collision data collected at $\sqrt{s}$ =13 TeV with the ATLAS detector". In:

Phys. Rev. D 96.5 (2017), p. 052004. DOI: 10.1103/PhysRevD.96.052004. arXiv: 1703.09127 [hep-ex].

[117] ATLAS Collaboration. "Search for strong gravity in multijet final states produced in pp collisions at $\sqrt{s} = 13$ TeV using the ATLAS detector at the LHC". In: *JHEP* 03 (2016), p. 026. DOI: 10.1007/JHEP03(2016)026. arXiv: 1512.02586 [hep-ex].

[118] S. Schael et al. "Precision electroweak measurements on the Z resonance". In: *Phys. Rept.* 427 (2006), pp. 257–454. DOI: 10.1016/j.physrep.2005.12.006. arXiv: hep-ex/0509008.

[119] ATLAS Collaboration. "Test of the universality of τ and μ lepton couplings in W-boson decays with the ATLAS detector". In: *Nature Phys.* 17.7 (2021), pp. 813–818. DOI: 10.1038/s41567-021-01236-w.

[120] LHCb Collaboration. "Differential branching fractions and isospin asymmetries of $B \to K^{(*)}\mu^+\mu^-$ decays". In: *JHEP* 06 (2014), p. 133. DOI: 10.1007/JHEP06(2014)133. arXiv: 1403.8044 [hep-ex].

[121] LHCb Collaboration. "Angular analysis and differential branching fraction of the decay $B_s^0 \to \phi\mu^+\mu^-$". In: *JHEP* 09 (2015), p. 179. DOI: 10.1007/JHEP09(2015)179. arXiv: 1506.08777 [hep-ex].

[122] Belle Collaboration. "Lepton-Flavor-Dependent Angular Analysis of $B \to K^*\ell^+\ell^-$". In: *Phys. Rev. Lett.* 118.11 (2017), p. 111801. DOI: 10.1103/PhysRevLett.118.111801. arXiv: 1612.05014 [hep-ex].

[123] Belle Collaboration. "Angular analysis of $B^0 \to K^*(892)^0\ell^+\ell^-$". In: *LHC Ski 2016: A First Discussion of 13 TeV Results*. Apr. 2016. arXiv: 1604.04042 [hep-ex].

[124] ATLAS Collaboration. "Angular analysis of $B_d^0 \to K^*\mu^+\mu^-$ decays in pp collisions at $\sqrt{s} = 8$ TeV with the ATLAS detector". In: (Apr. 2017). Ed. by Etienne Auge, Jacques Dumarchez, and Jean Tran Thanh Van.

[125] CMS Collaboration. "Measurement of the P_1 and P_5' angular parameters of the decay $B^0 \to K^{*0}\mu^+\mu^-$ in proton-proton collisions at $\sqrt{s} = 8$ TeV". In: (2017).

[126] LHCb Collaboration. "Test of lepton universality in beauty-quark decays". In: (Mar. 2021). arXiv: 2103.11769 [hep-ex].

[127] Muon g 2 Collaboration. "Measurement of the Positive Muon Anomalous Magnetic Moment to 0.46 ppm". In: *Phys. Rev. Lett.* 126.14 (2021), p. 141801. DOI: 10.1103/PhysRevLett.126.141801. arXiv: 2104.03281 [hep-ex].

[128] Howard Georgi and S. L. Glashow. "Unity of All Elementary-Particle Forces". In: *Phys. Rev. Lett.* 32 (8 1974), pp. 438–441. DOI: 10.1103/PhysRevLett.32.438. URL: https://link.aps.org/doi/10.1103/PhysRevLett.32.438.

[129] Jogesh C. Pati and Abdus Salam. "Unified Lepton-Hadron Symmetry and a Gauge Theory of the Basic Interactions". In: *Phys. Rev. D* 8 (1973), pp. 1240–1251. DOI: 10.1103/PhysRevD.8.1240.

[130] Andreas Crivellin. "Explaining the flavor anomalies with the Pati-Salam leptoquarks". In: *PoS* ALPS2018 (2018), p. 007. DOI: 10.22323/1.330.0007.

[131] Dario Müller. "Leptoquarks in Flavour Physics". In: *EPJ Web Conf.* 179 (2018). Ed. by Giancarlo D'Ambrosio et al., p. 01015. DOI: 10.1051/epjconf/201817901015. arXiv: 1801.03380 [hep-ph].

[132] Andreas Crivellin and Francesco Saturnino. "Explaining the Flavor Anomalies with a Vector Leptoquark (Moriond 2019 update)". In: *PoS* DIS2019 (2019), p. 163. DOI: 10.22323/1.352.0163. arXiv: 1906.01222 [hep-ph].

[133] Innes Bigaran, John Gargalionis, and Raymond R. Volkas. "A near-minimal leptoquark model for reconciling flavour anomalies and generating radiative neutrino masses". In: *JHEP* 10 (2019), p. 106. DOI: 10.1007/JHEP10(2019)106. arXiv: 1906.01870 [hep-ph].

[134] Oleg Popov and Graham A White. "One Leptoquark to unify them? Neutrino masses and unification in the light of $(g-2)_\mu$, $R_{D^{(*)}}$ and R_K anomalies". In: *Nucl. Phys. B* 923 (2017), pp. 324–338. DOI: 10.1016/j.nuclphysb.2017.08.007. arXiv: 1611.04566 [hep-ph].

[135] Ilja Doršner and Admir Greljo. "Leptoquark toolbox for precision collider studies". In: *JHEP* 05 (2018), p. 126. DOI: 10.1007/JHEP05(2018)126. arXiv: 1801.07641 [hep-ph].

[136] CMS Collaboration. "Search for single production of scalar leptoquarks in proton-proton collisions at $\sqrt{s} = 8$ *TeV*". In: *Phys. Rev. D* 93.3 (2016). [Erratum: Phys.Rev.D 95, 039906 (2017)], p. 032005. DOI: 10.1103/PhysRevD.93.032005. arXiv: 1509.03750 [hep-ex].

[137] ATLAS Collaboration. "Vertex Reconstruction Performance of the ATLAS Detector at $\sqrt{s} = 13$ *TeV*". In: (2015).

[138] ATLAS Collaboration. "Selection of jets produced in 13TeV proton-proton collisions with the ATLAS detector". In: (July 2015).

[139] I. Doršner et al. "Physics of leptoquarks in precision experiments and at particle colliders". In: *Phys. Rept.* 641 (2016), pp. 1–68. DOI: 10.1016/j.physrep.2016.06.001. arXiv: 1603.04993 [hep-ph].

[140] Torbjorn Sjostrand, Stephen Mrenna, and Peter Z. Skands. "A Brief Introduction to PYTHIA 8.1". In: *Comput. Phys. Commun.* 178 (2008), pp. 852–867. DOI: 10.1016/j.cpc.2008.01.036. arXiv: 0710.3820 [hep-ph].

[141] Kirill Melnikov and Frank Petriello. "Electroweak gauge boson production at hadron colliders through O(alpha(s)**2)". In: *Phys. Rev. D* 74 (2006), p. 114017. DOI: 10.1103/PhysRevD.74.114017. arXiv: hep-ph/0609070.

[142] Ryan Gavin et al. "FEWZ 2.0: A code for hadronic Z production at next-to-next-to-leading order". In: *Comput. Phys. Commun.* 182 (2011), pp. 2388–2403. DOI: 10.1016/j.cpc.2011.06.008. arXiv: 1011.3540 [hep-ph].

[143] A.D. Martin et al. "Parton distributions for the LHC". In: *Eur. Phys. J. C* 63 (2009), pp. 189–285. DOI: 10.1140/epjc/s10052-009-1072-5. arXiv: 0901.0002 [hep-ph].

[144] A.D. Martin et al. "Uncertainties on alpha(S) in global PDF analyses and implications for predicted hadronic cross sections". In: *Eur. Phys. J. C* 64 (2009), pp. 653–680. DOI: 10.1140/epjc/s10052-009-1164-2. arXiv: 0905.3531 [hep-ph].

[145] A.D. Martin et al. "Heavy-quark mass dependence in global PDF analyses and 3- and 4-flavour parton distributions". In: *Eur. Phys. J. C* 70 (2010), pp. 51–72. DOI: 10.1140/epjc/s10052-010-1462-8. arXiv: 1007.2624 [hep-ph].

[146] Emanuele Re. "Single-top Wt-channel production matched with parton showers using the POWHEG method". In: *Eur. Phys. J. C* 71 (2011), p. 1547. DOI: 10.1140/epjc/s10052-011-1547-z. arXiv: 1009.2450 [hep-ph].

[147] Stefano Frixione et al. "Single-top hadroproduction in association with a W boson". In: *JHEP* 07 (2008), p. 029. DOI: 10.1088/1126-6708/2008/07/029. arXiv: 0805.3067 [hep-ph].

[148] Simone Alioli et al. "NLO single-top production matched with shower in POWHEG: s- and t-channel contributions". In: *JHEP* 09 (2009). [Erratum: JHEP 02, 011 (2010)], p. 111. DOI: 10.1088/1126-6708/2009/09/111. arXiv: 0907.4076 [hep-ph].

[149] Tanju Gleisberg and Stefan Hoeche. "Comix, a new matrix element generator". In: *JHEP* 12 (2008), p. 039. DOI: 10.1088/1126-6708/2008/12/039. arXiv: 0808.3674 [hep-ph].

[150] F. Cascioli, P. Maierhöfer, and S. Pozzorini. "Scattering Amplitudes with Open Loops". In: *Phys. Rev. Lett.* 108 (11 2012), p. 111601. DOI: 10.1103/PhysRevLett.108.111601. URL: https://link.aps.org/doi/10.1103/PhysRevLett.108.111601.

[151] Stefan Hoeche et al. "QCD matrix elements + parton showers: The NLO case". In: *JHEP* 04 (2013), p. 027. DOI: 10.1007/JHEP04(2013)027. arXiv: 1207.5030 [hep-ph].

[152] Stefano Frixione and Bryan R. Webber. "Matching NLO QCD computations and parton shower simulations". In: *JHEP* 06 (2002), p. 029. DOI: 10.1088/1126-6708/2002/06/029. arXiv: hep-ph/0204244.

[153] ATLAS Collaboration. "Electron and photon energy calibration with the ATLAS detector using LHC Run 1 data". In: *Eur. Phys. J. C* 74.10 (2014), p. 3071. DOI: 10.1140/epjc/s10052-014-3071-4. arXiv: 1407.5063 [hep-ex].

[154] ATLAS Collaboration. "Muon reconstruction performance of the ATLAS detector in proton–proton collision data at $\sqrt{s}$ =13 TeV". In: *Eur. Phys. J. C* 76.5 (2016), p. 292. DOI: 10.1140/epjc/s10052-016-4120-y. arXiv: 1603.05598 [hep-ex].

[155] ATLAS Collaboration. "Performance of pile-up mitigation techniques for jets in pp collisions at $\sqrt{s} = 8$ TeV using the ATLAS detector". In: *Eur. Phys. J. C* 76.11 (2016), p. 581. DOI: 10.1140/epjc/s10052-016-4395-z. arXiv: 1510.03823 [hep-ex].

[156] ATLAS Collaboration. "Optimisation and performance studies of the ATLAS b-tagging algorithms for the 2017-18 LHC run". In: (July 2017).

[157] ATLAS Collaboration. "Performance of b-Jet Identification in the ATLAS Experiment". In: *JINST* 11.04 (2016), P04008. DOI: 10.1088/1748-0221/11/04/P04008. arXiv: 1512.01094 [hep-ex].

[158] ATLAS Collaboration. "Muon reconstruction performance of the ATLAS detector in proton–proton collision data at $\sqrt{s}$ =13 TeV". In: *Eur. Phys. J. C* 76.5 (2016), p. 292. DOI: 10.1140/epjc/s10052-016-4120-y. arXiv: 1603.05598 [hep-ex].

[159] ATLAS Collaboration. "Identification of boosted, hadronically decaying W bosons and comparisons with ATLAS data taken at $\sqrt{s} = 8$ TeV". In: *Eur. Phys. J. C* 76.3 (2016), p. 154. DOI: 10.1140/epjc/s10052-016-3978-z. arXiv: 1510.05821 [hep-ex].

[160] ATLAS Collaboration. "Performance of b-Jet Identification in the ATLAS Experiment". In: *JINST* 11.04 (2016), P04008. DOI: 10.1088/1748-0221/11/04/P04008. arXiv: 1512.01094 [hep-ex].

[161] ATLAS Collaboration. "Measurements of b-jet tagging efficiency with the ATLAS detector using $t\bar{t}$ events at $\sqrt{s} = 13$ TeV". In: *JHEP* 08 (2018), p. 089. DOI: 10.1007/JHEP08(2018)089. arXiv: 1805.01845 [hep-ex].

[162] Enrico Bothmann, Marek Schönherr, and Steffen Schumann. "Reweighting QCD matrix-element and parton-shower calculations". In: *Eur. Phys. J. C* 76.11 (2016), p. 590. DOI: 10.1140/epjc/s10052-016-4430-0. arXiv: 1606.08753 [hep-ph].

[163] Sayipjamal Dulat et al. "New parton distribution functions from a global analysis of quantum chromodynamics". In: *Phys. Rev. D* 93.3 (2016), p. 033006. DOI: 10.1103/PhysRevD.93.033006. arXiv: 1506.07443 [hep-ph].

[164] L. A. Harland-Lang et al. "Parton distributions in the LHC era: MMHT 2014 PDFs". In: *Eur. Phys. J. C* 75.5 (2015), p. 204. DOI: 10.1140/epjc/s10052-015-3397-6. arXiv: 1412.3989 [hep-ph].

[165] ATLAS Collaboration. "Simulation of top quark production for the ATLAS experiment at sqrt(s) = 13 TeV". In: (Jan. 2016).

[166] Jon Butterworth et al. "PDF4LHC recommendations for LHC Run II". In: *J. Phys. G* 43 (2016), p. 023001. DOI: 10.1088/0954-3899/43/2/023001. arXiv: 1510.03865 [hep-ph].

[167] S. S. Wilks. "The Large-Sample Distribution of the Likelihood Ratio for Testing Composite Hypotheses". In: *Annals Math. Statist.* 9.1 (1938), pp. 60–62. DOI: 10.1214/aoms/1177732360.